

# Numerical analysis of multiaxial test setup for composite cryogenic hydrogen tank development

Master Thesis

AE5711: Thesis Aerospace Structures and Materials  
Mateusz Lentner

Delft University of Technology

# Numerical analysis of multiaxial test setup for composite cryogenic hydrogen tank development

Master Thesis

by

Mateusz Lentner

Student Name	Student Number
Mateusz Lentner	4673824

Promotor: C. Dransfeld.  
Company Supervisor: J. Koord  
University Supervisor: B. Atli-Veltin  
Faculty: Faculty of Aerospace Engineering, Delft

Cover: NASA Tests Game Changing Composite Cryogenic Fuel Tank  
*[https : //www.nasa.gov/content/nasa - tests - game -  
changing - composite - cryogenic - fuel - tank\\_marshall\\_ews](https://www.nasa.gov/content/nasa-tests-game-changing-composite-cryogenic-fuel-tank_marshall_ews)*

# Preface

The present thesis report was written as part of my fulfilment of the Master's degree in the Aerospace Structures in Materials track at the Delft University of Technology. The topic of the thesis and the project's initial scope were defined by the Deutsches Zentrum für Luft und Raumfahrt e.V. / German Aerospace Center (DLR). The DLR supported and supervised the work during the entire duration of the process. However, this report wouldn't be possible without the help of certain people.

First and foremost, I would like to thank my company supervisor, Josef Koord. His guidance was essential in achieving the presented results. I'm incredibly grateful for the time that he gave me during our work sessions and meetings. Without his help, the presented report wouldn't have been possible.

Furthermore, my university supervisor, Bilim Atli-Veltin, was crucial in meeting the necessary deadlines and helped me tremendously in structuring my work. Her guidance also helped me grow as a student and an engineer. I'm thankful for all the kind words of encouragement and advice.

Last but definitely not least, I want to thank my friends and family, who were there with me throughout the entire journey. I was surrounded by people who deeply cared for me. This especially goes to my partner, Francesca van Marion, without whom the thesis journey wouldn't have been the same. You were always there for me, and this pushed me to reach the final line. Thank you for that.

*Mateusz Lentner  
Delft, February 2024*

# Summary

Hydrogen is one of aviation's most promising fuel alternatives for the coming years. However, to store it, a large and light vessel is needed. One of the promising candidates for this purpose is the carbon fibre fuel tank, as it saves significant weight against alternatives like metals. But despite its advantages, the composite tank has many disadvantages and limitations. One of which is the permeation and leakage of hydrogen molecules through its wall structure. Permeation happens as the polymeric matrix of the composite walls allows for the penetration of the very small hydrogen atoms. On the other hand, leakage is caused by crack propagation in the material due to repeated thermo-mechanical cycling. Regardless of the cause, both phenomena must be understood appropriately to design the hydrogen tank. They can cause fuel boil-offs or create dangerous situations for the passengers inside the aircraft. Despite the use of many simulations or analytical methods, the experimental approach is the only proven way to quantify these phenomena.

Many experimental methods have been developed to measure permeation and leakage through the composite laminate. They differ in both complexity and representativeness of the actual operational tank conditions. Simple methods focus mainly on the material aspect, where the thermo-mechanical loading is wholly disregarded. By taking into account thermal and mechanical conditions present in the tank walls, the representativeness of the given approach is improved. Simultaneously, however, the complexity and cost of experimental methods are increasing, ultimately reaching the highest point for full-scale prototype testing. Of all the different methods used in the research concerning permeation and leakage, one in particular lacks deep understanding and is almost wholly lacking in European research. This method is characterised by using more advanced specimen shapes like cross-shaped, tubular or circular laminate. Furthermore, it aims to achieve more representative thermo-mechanical conditions by applying mechanical loading similar to the one present in the tank walls and, at the same time, reaching cryogenic temperatures during testing. Based on these aspects, the approach is relevant for developing the composite hydrogen tank as it provides realistic conditions by a fraction of the cost of full-scale testing. However, it is unclear how the particular testing approach should be designed to achieve representative conditions and desirable results.

This brings the necessity to answer the following posed research question: How can the element-level testing of CFRP accurately represent the behaviour of a full-scale hydrogen tank on the topic of permeation and leakage? A better understanding of the element level can help choose suitable parameters for testing and accelerate the development of the composite hydrogen tank. As the permeation and leakage testing using more advanced shapes is comprehensive to aid this work, it was decided to focus only on one particular aspect: the bulge bi-axial testing. This decision was also supported by the thesis provider, the Deutsches Zentrum für Luft und Raumfahrt (DLR).

A numerical analysis approach was chosen using Abaqus software to answer this question. This way, all the parameters influencing the testing based on the available literature can be analysed and quantified. Following such an approach, the effect of variables on the stress state of the specimen can be evaluated by implementing a parametric study. From that, the equal bi-axial zone of the given specimen can also be estimated, which should dictate the measurement area for the permeation and leakage testing. Furthermore, other aspects, like damage initiation caused by the loading, are under investigation using LARC05 damage criteria. Finally, the thermal simulations for the entire testing rig are also provided to determine the specimen cooling conditions, test different methods to improve the cooling rate and find possible limitations.

Based on those analyses, the dependency of each defined parameter can be provided, and the potential damage from the required loading conditions can be estimated. Thus, a recommendation for the shape and characteristics of the specimen used in the bulge bi-axial testing can be given. By considering the thermal aspect and the clamping conditions, the initial design of the entire testing rig can also be proposed. This way, a better and more representative testing rig for the permeation and leakage measurement can be developed, provided that the model used in this research is first validated.

# Contents

<b>Preface</b>	<b>i</b>
<b>Summary</b>	<b>ii</b>
<b>Nomenclature</b>	<b>ix</b>
<b>1 Introduction</b>	<b>1</b>
1.1 Composite LH2 tanks: State of the art, History of the CFRP tank development . . . . .	1
1.2 Challenges . . . . .	3
1.3 Permeation and Leakage concerns . . . . .	3
1.4 Experimental testing methods . . . . .	4
1.4.1 Coupon level testing . . . . .	4
1.4.2 Element level testing . . . . .	5
1.4.3 Sub-scale testing . . . . .	5
1.4.4 Full-scale testing . . . . .	6
1.4.5 Methods of measurement . . . . .	6
1.5 Research Gap . . . . .	8
1.5.1 Research question . . . . .	8
<b>2 Methodology</b>	<b>9</b>
2.1 Experimental research and methodology . . . . .	10
2.1.1 Cross-setup testing . . . . .	10
2.1.2 Small-cylinder testing . . . . .	11
2.1.3 Bulge setup testing . . . . .	13
2.1.4 Parameters of interest . . . . .	14
2.1.5 Design approach . . . . .	19
2.1.6 Operational approach . . . . .	22
2.2 Numerical research and methodology . . . . .	23
2.2.1 Simplification and assumptions . . . . .	23
2.2.2 Parameters and Variables . . . . .	24
2.2.3 Numerical Model Setup . . . . .	25
2.2.4 Model verification . . . . .	28
2.2.5 Configuration for the parametric study . . . . .	30
2.2.6 Equal bi-axial zone . . . . .	31
2.2.7 Damage Analysis setup and implementation . . . . .	32
2.2.8 Practical testing consideration . . . . .	34
<b>3 Results</b>	<b>38</b>
3.1 Parametric study results . . . . .	39
3.1.1 Effect of the Diameter . . . . .	40
3.1.2 Effect of the Curvature . . . . .	44
3.1.3 Effect of the Thickness . . . . .	48
3.1.4 Effect of the Pressure . . . . .	52
3.1.5 Effect of the Layup . . . . .	56
3.2 Damage Analysis results . . . . .	60
3.2.1 Damage results for the different reinforcement thickness . . . . .	62
3.2.2 Damage results for the different reinforcement material . . . . .	64
3.2.3 Damage results for the different reinforcement width . . . . .	67
3.2.4 Damage results for the single-sided and double-sided reinforcement . . . . .	69
3.3 Thermal modelling results . . . . .	71
3.3.1 Other cooling methods . . . . .	75

---

<b>4</b>	<b>Discussions</b>	<b>79</b>
4.1	Effect of different parameters	80
4.1.1	Influence of the diameter	80
4.1.2	Influence of the curvature	80
4.1.3	Influence of the thickness	81
4.1.4	Influence of the pressure	81
4.1.5	Influence of the layup	82
4.2	Damage and element testing	82
4.2.1	Influence of the reinforcement	83
4.3	Thermal aspect	84
4.3.1	Liquid nitrogen submersion method	84
4.3.2	Other cooling methods	85
4.4	Research question reflections	86
<b>5</b>	<b>Conclusions</b>	<b>88</b>
<b>6</b>	<b>Recommendations</b>	<b>90</b>
	<b>References</b>	<b>91</b>
<b>7</b>	<b>Model verification</b>	<b>97</b>
7.1	Mesh convergence	97
7.1.1	Results for the X-path	97
7.1.2	Results for the Z-path	98
7.1.3	Results for the Small circular path	99
7.1.4	Results for the Large circular path	100
7.1.5	Meshing strategy	101
7.1.6	Verification	104

# List of Figures

1.1	Composite liquid hydrogen tanks developed till 2004 Figure 1.1a and testing of a large scale tank, part of the CCTD program Figure 1.1b . . . . .	2
1.2	Diffusion-driven process of molecules transport in Figure 1.2a and free passage of molecules through the crack network in Figure 1.2b . . . . .	4
1.3	Testing triangle: Overview of different permeation testing methods in the literature and grouped into different categories. . . . .	6
1.4	Graphical representation of the different methods used for the permeation and leakage measurement . . . . .	7
2.1	Cross-specimen permeation testing instrumentation present at JAXA [46] . . . . .	11
2.2	Examples of the multi-axial permeation rigs developed by NASA . . . . .	11
2.3	Permeation setups used for the tubular specimen testing Figure 2.3a by [104] and Figure 2.3b by [63] . . . . .	12
2.4	Graphical representation of the Monometric method Figure 1.4a and Volumetric method Figure 1.4c . . . . .	13
2.5	Out-of-plane bi-axial testing rig for the permeation and leakage measurement developed by Raffaelli [81] . . . . .	14
2.6	Chosen symmetric layouts for the research . . . . .	16
2.7	Specimen geometries from the literature for the bulge bi-axial testing . . . . .	20
2.8	Chosen approach for the numerical analysis regarding clamping and specimen geometry . . . . .	20
2.9	Tank dimensions for the SLS upper stage and the test article from the CCTD project . . . . .	21
2.10	Initial design approach for the bulge bi-axial testing setup used to build a numerical simulation . . . . .	22
2.11	Assumed steps that specimen would experience before and during permeation and leakage testing with the bulge bi-axial testing approach . . . . .	23
2.12	Representative of the parameters definition . . . . .	24
2.13	Coordinate system used for the numerical analysis . . . . .	24
2.14	Clamping zone at which the clamping force is applied to . . . . .	25
2.15	Overview of all the parameters involved in the numerical analysis research . . . . .	25
2.16	Chosen boundary conditions for the clamping of the laminate . . . . .	26
2.17	Steps with different loading conditions and the temperature of the laminate used during the numerical analysis . . . . .	27
2.18	The chosen parametric study matrix with all the variables used . . . . .	31
2.19	LARC05 damage criteria . . . . .	32
2.20	Possible specimen reinforcement, with the definition of width and thickness parameter . . . . .	34
2.21	Assumed temperature over time of the Helium applied to the system . . . . .	35
2.22	Dewar used by the DLR to perform the submersion testing . . . . .	36
2.23	Approach for the modelling and boundary conditions introduction for the thermal analysis . . . . .	36
2.24	Three possible designs for the cooling method of the out-of-plane bi-axial setup for the permeation and leakage testing. . . . .	37
3.1	Variables analysed for the diameter effect study . . . . .	40
3.2	Vertical displacement of the specimen for the different values of the diameter. . . . .	40
3.3	The average and standard deviation of critical parameters . . . . .	41
3.4	The average and standard deviation of critical parameters . . . . .	42
3.5	The average and standard deviation of critical parameters . . . . .	43
3.6	Variables analysed for the curvature effect study . . . . .	44
3.7	Vertical displacement of the specimen for the different values of the curvature. . . . .	44
3.8	The average and standard deviation of critical parameters . . . . .	45

3.9	The average and standard deviation of critical parameters	46
3.10	Results of the equal bi-axial zone analysis, concerning specimen curvature for the top of the specimen	47
3.11	Results of the equal bi-axial zone analysis concerning specimen curvature for the bottom of the specimen	47
3.12	Variables analysed for the thickness effect study.	48
3.13	Vertical displacement of the specimen with different thicknesses	48
3.14	The average and standard deviation of critical parameters	49
3.15	The average and standard deviation of critical parameters	50
3.16	Equal bi-axial zone distribution at the top of the specimen	51
3.17	Equal bi-axial zone distribution at the bottom of the specimen	51
3.18	Variables analysed for the pressure effect study	52
3.19	Vertical displacement of the specimen for the different values of the pressure	52
3.20	The average and standard deviation of critical parameters	53
3.21	The average and standard deviation of critical parameters	54
3.22	Equal bi-axial zone distribution at the top of the specimen	54
3.23	Equal bi-axial zone distribution at the bottom of the specimen	55
3.24	Variables analysed for the layup effect study	56
3.25	Vertical displacement of the specimen for the different layup options	56
3.26	The average and standard deviation of critical parameters	57
3.27	The average and standard deviation of critical parameters	58
3.28	The average and standard deviation of critical parameters	59
3.29	Equal bi-axial zone distribution at the top of the specimen	60
3.30	Equal bi-axial zone distribution at the bottom of the specimen	60
3.31	Legend for the damage analysis graphs	61
3.32	Stress and strain values for the specimen with the indication of the first damage appearance	61
3.33	Stress and strain values for the specimen with the 1 mm thick reinforcement with the indication of the first damage appearance	62
3.34	Stress and strain values for the specimen with the 2 mm thick reinforcement with the indication of the first damage appearance	62
3.35	Stress and strain values for the specimen with the 4 mm thick reinforcement with the indication of the first damage appearance	63
3.36	Stress and strain values for the specimen with the steel reinforcement with the indication of the first damage appearance	65
3.37	Stress and strain values for the specimen with the aluminium reinforcement with the indication of the first damage appearance	65
3.38	Stress and strain values for the specimen with the CFRP reinforcement with the indication of the first damage appearance	65
3.39	Stress and strain values for the specimen with the CFRP reinforcement at the 45-degree angle with the indication of the first damage appearance	67
3.40	Stress and strain values for the specimen with the reinforcement width of 60 [mm] with the indication of the first damage appearance	67
3.41	Stress and strain values for the specimen with the reinforcement width of 80 [mm] with the indication of the first damage appearance	68
3.42	Stress and strain values for the specimen with the reinforcement width of 100 [mm] with the indication of the first damage appearance	68
3.43	Stress and strain values for the specimen with single and double reinforcement with the indication of the first damage appearance	70
3.44	Models of the testing rig used for the heat capacity calculations and thermal analysis	71
3.45	The average and standard deviation of critical parameters	72
3.46	The average and standard deviation of critical parameters	73
3.47	The average and standard deviation of critical parameters	73
3.48	Temperature change for the specimen's centre with a and without pre-cooling step	74
3.49	Temperature and heat flux change for the specimen's centre and the bottom enclosure of the permeation setup during the application of warmer helium gas to the system.	75
3.50	Effect of the warmer helium gas on the temperature distribution of the testing setup	75

---

3.51	Effect of the Cold gas cooling method on the temperature distribution of the testing setup	76
3.52	Effect of the cold gas cooling on the temperature and heat flux of the specimen . . . . .	76
3.53	Effect of the cold gas cooling on the heat flux distribution of the specimen . . . . .	76
3.54	Effect of the Cryostat cooling method on the temperature distribution of the testing setup	77
3.55	Effect of the cryostat cooling method on the temperature and heat flux of the specimen at the point of the maximum heat flux registered in the specimen's centre . . . . .	77
3.56	Effect of the cryostat cooling method on the heat flux distribution of the specimen . . . . .	77
3.57	Effect of the cooling fins on the temperature distribution of the testing setup . . . . .	78
3.58	Effect of the cooling fins on the temperature and heat flux of the specimen at the point of the maximum heat flux registered in the specimen's centre . . . . .	78
3.59	Effect of the cooling fins on the heat flux distribution of the specimen . . . . .	78
7.1	X-path used for the results presentation. . . . .	97
7.2	The average and standard deviation of critical parameters . . . . .	98
7.3	Z-path used for the results presentation . . . . .	98
7.4	The average and standard deviation of critical parameters . . . . .	99
7.5	Small circle path used for the results presentation . . . . .	99
7.6	The average and standard deviation of critical parameters . . . . .	100
7.7	Large circle path used for the results presentation . . . . .	100
7.8	The average and standard deviation of critical parameters . . . . .	101
7.9	Vertical displacement along the x-path for different mesh strategies . . . . .	102
7.10	The average and standard deviation of critical parameters . . . . .	102
7.11	The average and standard deviation of critical parameters . . . . .	103
7.12	The average and standard deviation of critical parameters . . . . .	104

# List of Tables

2.1	Material characteristics at room and cryogenic temperature for the IM7/8552 material system [91]	15
2.2	Effect of the different boundary conditions on the specimen	26
2.3	Chosen mesh sizes for the mesh convergence study	29
2.4	Set of meshes used in the meshing strategy study	30
2.5	Material strength properties derived from the work of Sheerer et al. [91]	33
2.6	Reinforcement parameters and variables used in the analysis	34
2.7	Thermal properties of the materials used for the cooling analysis	35
3.1	Chosen paths across the specimen for the results presentation	39
3.2	Specimen status just before or at the first damage appearance for each of the initial damage criterion	61
3.3	Specimen status just before or at the first damage appearance for each of the initial damage criterion and for all tested reinforcement's thicknesses	64
3.4	Specimen status just before or at the first damage appearance for each of the initial damage criterion and for all tested reinforcement's materials	66
3.5	Specimen status just before or at the first damage appearance for each of the initial damage criterion for the composite reinforcement with the 45-degree position angle	67
3.6	Specimen status just before or at the first damage appearance for each of the initial damage criterion and for all tested reinforcement's widths	69
3.7	Specimen status just before or at the first damage appearance for each of the initial damage criteria for both single and double reinforcement	70
3.8	Inputs for the estimation of the liquid nitrogen volume necessary for the cooling of the setup	71
3.9	Specimen status at different points during the cooling procedure for the method with the pre-cooling step and the method with the pure liquid nitrogen submersion cooling.	74
7.1	Chosen paths across the specimen for the results presentation	97
7.2	Computing time of each meshing methods.	101
7.3	Specific values of the stress and strain, from the results regarding the determination of the dependency of the square partitioning line	104
7.4	Results of the performed verification	105

# Nomenclature

## Abbreviations

Abbreviation	Definition
CFRP	Carbon Fibre Reinforced Polymer
NASA	National Aeronautics and Space Administration
SSTO	Single Stage to Orbit
RLV	Reusable Launch Vehicle
CCTD	Composite Cryotank Technology Development
SLS	Space Launch System
MSFC	Marshall Space Flight Centre
CHATT	Cryogenic Hypersonic Advanced Tank Technologies
DLR	Deutsches Zentrum für Luft und Raumfahrt
PHOEBUS	Prototype of a Highly Optimised Black Upper Stage
JAXA	Japanese Space Agency
DC-X	Delta Clipper experimental
SLI	Space Launch Initiative

## Symbols

Symbol	Definition	Unit
$l$	Thickness	[mm]
$n$	Pressure exponent (sorption)	[-]
$p_f$	Pressure at feed	[bar]
$w$	Vertical deflection	[mm]
$r$	Radius	[mm]
$p$	Pressure	[bar]
$t$	Wall thickness	[mm]
$a$	Plate radius	[mm]
$q$	Distributed load	[N/mm]
$h$	Thickness of the plate	[mm]
$A$	Area	[m <sup>2</sup> ]
$D$	Diffusivity	[m <sup>2</sup> s <sup>-1</sup> ]
$E_p$	Activation energy of P	[J/mol]
$E$	Elastic modulus	[Pa]
$F$	Force	[N]
$J_{ss}$	Steady state flux of molecules	[bar / l s]
$P$	Permeability	[mol/ m s Pa]
$P_0$	pre-exponential factor of P	[-]
$R$	Universal Gas Constant	[J/mol]
$S$	Solubility	[mol/l]
$T$	Temperature	[K]
$X_T$	Longitudinal tensile strength	[Pa]
$X_C$	Longitudinal compressive strength	[Pa]
$Y_T$	Transverse tensile strength	[Pa]
$Y_C$	Transverse compressive strength	[Pa]

Symbol	Definition	Unit
$S_L$	Plane shear strength	[Pa]
$S_T$	Transverse shear strength	[Pa]
$\sigma$	Stress	[Pa]
$\sigma_h$	Hoop stress	[Pa]
$\sigma_a$	Axial stress	[Pa]
$\alpha_0$	Fracture plane angle for compression	[°]
$\eta_L$	Longitudinal shear friction coefficient	[-]
$\eta_T$	Transverse shear friction coefficient	[-]

# 1

## Introduction

Current environmental challenges require tremendous efforts in all industries to change the climate and stop global warming effectively. Batteries and the transition to electric energy are promising if sustainable energy sources are used. Unfortunately, with the current battery technology, electric planes, especially on long-distance routes, are unfeasible [94]. That's why industry players like Airbus, to tackle the environmental challenges, turned to liquid hydrogen as an alternative fuel for their planes [40]. Hydrogen, with its good performance per kilogram, is an excellent candidate to allow the aviation industry to meet the net zero carbon emissions goals by 2050 [6, 70]. This is especially true if hydrogen is used in its much denser form as a liquid. Unfortunately, even in the liquid form, hydrogen takes up a lot of volume, and its volumetric index is poor. That's why the liquid hydrogen storage tank must be very light and robust to support the operational requirements of aeroplane operators [1] to reach a satisfactory gravimetric index of around 15 %. Hence, companies like Airbus are intensively looking into the feasibility of composite hydrogen tanks for aviation with the ZEROe project, for example, [2]. Carbon Fibre Reinforced Polymer (CFRP) is the most promising candidate for this task. CFRP is a suitable material choice for a large liquid hydrogen tank due to its superior performance, especially its high strength-to-weight ratio and low thermal conductivity compared to other engineering materials like aluminium or steel.

Liquid hydrogen as a fuel source has been used for many years in the aerospace industry. Many launchers and rockets already used liquid hydrogen as a fuel source in the 1960s. Saturn V, the rocket that took people to the Moon, was powered by liquid hydrogen and oxygen, at least at the upper stages [75]. Nowadays, Ariane 5 and 6, Space Launch System (SLS), and many other rocket launchers currently in use are still utilising liquid hydrogen as a fuel [21], [4] [7].

That's why the development of composite hydrogen storage started in the space industry many years ago, mainly because any weight savings of the launcher are even more crucial than for the aircraft [22]. The research into lightweight tanks primarily focused on the upper stages of the launchers of Single Stage to Orbit (SSTO) vehicles, as the weight improvement there matters the most [85].

### 1.1. Composite LH2 tanks: State of the art, History of the CFRP tank development

According to National Aeronautics and Space Administration (NASA) research, hydrogen tanks made out of CFRP can see even a 30 % reduction in mass compared to the state-of-the-art aluminium tank and a 25 % decrease in cost [100]. Such an improvement created a significant incentive to develop the CFRP fuel tank and advance rocket launch technologies. Hence, in the last 30 years, substantial development took place to bring the technology of the CFRP tank to the production level. Countries across Europe and Asia advanced research in this field, but the first developments started in the 90s in the United States [109].

The first project aimed to develop a CFRP liquid hydrogen tank and make the single-stage to-orbit vehicle possible was the reusable launch vehicle program (RLV). In 1991, McDonnell Douglas designed and manufactured a Delta Clipper - Experimental (DC-X) vehicle [27]. The development process included designing and manufacturing one of the first fully composite liquid hydrogen tanks and composite

feedlines [26]. The program was cancelled in 1996 after a crash landing [8].

In 1994, NASA proposed a project to develop a new generation of the launch system. Technical progress of the CFRP tank was seen as the program's primary goal to make future SSTO vehicles possible [34]. The design by Lockheed Martin, the X-33, was chosen as the best compelling proposition from all competing manufacturers in 1996. This design included a multi-lobe composite liquid hydrogen tank with sandwich walls that also acted as insulation as the walls were evacuated and kept under a vacuum. The tank was regarded as one of the crucial sub-systems and was heavily tested under different conditions [64]. Unfortunately, during one of the ground tests in 1999 with liquid hydrogen, the tank experienced a catastrophic failure. After a thorough investigation, it was determined that the failure was caused by the liquid hydrogen leak in the inner sheet of the tank, which created the effect of cryo-pumping, which in turn caused delamination and failure of the structure [73]. Ultimately, due to the tank failure and other factors mentioned by Ransom et al. [82] the program was cancelled in 2001 [64].

The lessons learned from the X-33 project, like the usage of graphite composites and debonding issues [64] [82], were implemented in the Space Launch Initiative (SLI) project [86], where the development of the hydrogen tank was scaled down, and more traditional structures for the tank were investigated [28]. As a result, in 2004, Northrop Grumman built a sub-scale version of the CFRP tank [57]. The tank was consequently tested, but the test outcome is unknown to the author. Ultimately, the project concluded in 2006 [17]. The continued development of all composite hydrogen tanks up to this point can be seen in the Figure 1.1a.

From the SLI project, the next big step into the production-ready CFRP composite tank was done during the Composite Cryotank Technology Development (CCTD) Project, part of the Game-changing program, where the main task was to push the technology readiness of the composite tank components to accelerate the next generation of launcher structures [32]. The project started in 2011 and concluded in 2015. During the project run, a CFRP hydrogen tank was built and tested by Boeing company [67], as seen in Figure 1.1b.

However, many other proposals were also investigated, and the state-of-the-art aluminium tank was also designed as part of the program for the most tangible comparison [57]. The project used all the knowledge gathered from previous projects run by NASA, and the result was the working 2.4 m and 5.5 m diameter hydrogen tank [33].

From the CCTD project, the only other mention of the CFRP tank in the United States was the development of the Exploratory Upper Stage for the Space Launch System (SLS) vehicle, where the CFRP hydrogen tank will be used to decrease the mass of the upper stage and increase the overall performance of the vehicle. The latest known development is Boeing's successful ground test of the sub-scale tank performed at the Marshall Space Flight Centre (MSFC) [71].

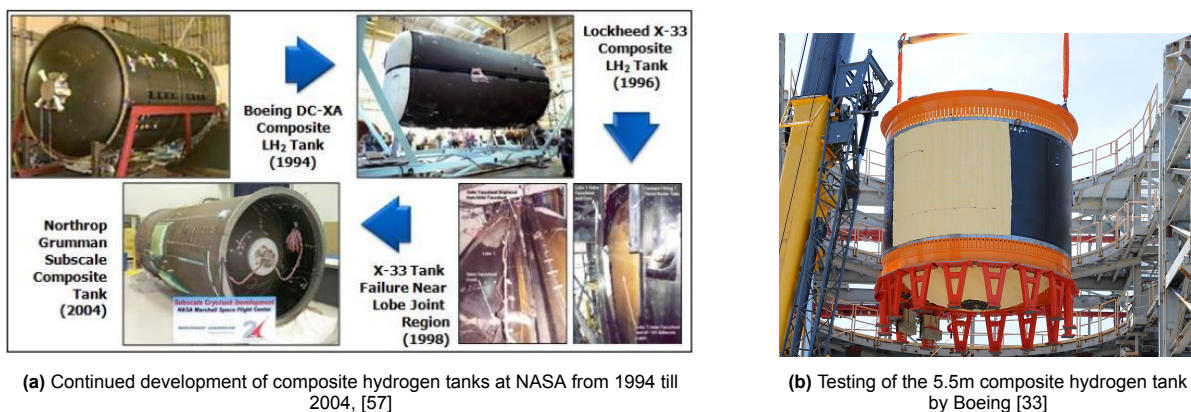


**Figure 1.1:** Composite liquid hydrogen tanks developed till 2004 Figure 1.1a and testing of a large scale tank, part of the CCTD program Figure 1.1b

The development of the composite cryogenic fuel tank wasn't only limited to the USA. Other European projects, including CHATT (Cryogenic Hypersonic Advanced Tank Technologies), also occurred. The project was run under the guidance of the DLR-SART between 2012 and 2015, and it was a multi-national collaboration. The project developed four different tank components in separate institutions to

investigate the feasibility of other manufacturing technologies like filament winding or automatic fibre placement. The metal liner tank, polymeric liner tank, liner-less tube component and four-lobe tank were built and tested for the CHATT project [93].

Another European development worth mentioning is the prototype of a highly optimised black upper-stage (PHOEBUS) project run by MT Aerospace and ArianeGroup. In this project, the new fully composite hydrogen tank is being developed for the next generation upper stage of the Ariane 6 rocket launcher [98]. Small-scale tanks were tested using liquid hydrogen, and actual tank components were manufactured for liquid oxygen and hydrogen storage [101].

Apart from the research done in the USA and Europe, the CFRP hydrogen tank was developed in Japan and China. In Japan, the research into the feasibility of the composite hydrogen tank was driven by the development of the SSTO vehicle in the early 2000s [53, 48]. More recent work in Japan focuses on developing the next-generation launchers for the Japanese Space Agency (JAXA) [76]. The same can be said about the Chinese efforts, where work is mainly related to developing the next-generation launchers [65].

Research into composite hydrogen tanks proved that many things could go wrong, especially looking at past failures like the X-33 project. Many challenges have been indicated, and much effort has already been made to overcome them.

## 1.2. Challenges

Many years of research on the CFRP liquid hydrogen tank identified the following challenges [31]:

- Large composite manufactured structure
- Usage of out-of-autoclave materials
- Mechanical and thermal cycling and effect on the structure lifetime
- Hydrogen permeation through the composite laminate
- Hydrogen leakage through cracks

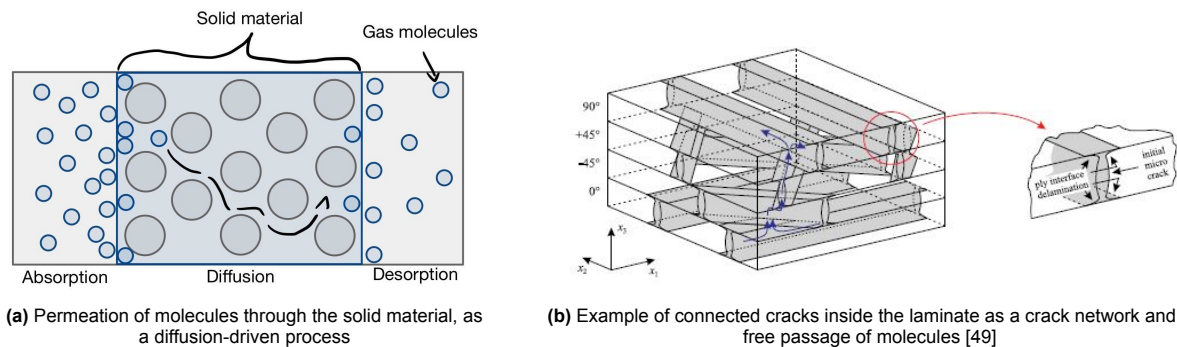
Some of those challenges have already been solved, as the progress into the composite liquid hydrogen tank for the launchers suggests. However, with the change of application from space to aviation, an entirely new set of requirements is needed, as the transition is not as straightforward as it may seem [69]. This creates even more challenges and obstacles for engineers. The previous challenges known for years are even more difficult to solve if the tank is placed into the aircraft frame. Most launcher tanks are rated at a maximum of a few to a hundred cycles. In the case of the aircraft, the number of cycles is in the range of thousands. This pushes the material capabilities even further. At the same time, the safety requirements are even more strict for aviation due to the large number of people onboard during normal operations. Currently, the only human-rated launcher with a future composite hydrogen tank is SLS block 1B, and astronauts will only use this vehicle version in 2028 [20].

Due to these strict safety requirements and a large number of thermo-mechanical cycles of the hydrogen tank during its operation, one challenge, in particular, became very difficult to solve in the aspect of aviation, namely permeation and hydrogen leakage through the tank walls. Hydrogen, when freely mixed in the air, can create an explosive mixture with oxygen [72]. Furthermore, the effectiveness of the vacuum insulation, which will most likely be used, can be reduced due to the inflow of the hydrogen molecules. This can cause the fuel to boil off and increase the pressure inside the tank. In the end, This set of events can initiate the tank's rupture if the safety mechanisms fail. Hence, hydrogen permeation and leakage must be researched before the composite hydrogen tank for aviation can be designed and manufactured. However, before this can happen, both phenomena must be understood.

## 1.3. Permeation and Leakage concerns

Even though permeation and leakage are usually linked and create similar concerns for engineers, they are two distinctive processes. In essence, permeation is the transport of molecules through the solid barrier [92, 36]. Hydrogen is the smallest molecule known to man, and it can permeate through many materials, for example, a resin in a composite laminate. Conversely, leakage is a passage of molecules through openings inside the material like cracks or delaminations [68, 44]. Both phenomena can be easily compared by looking Figure 1.2. On the left Figure 1.2a, one can see the diffusion-driven

process through the material, while on the right Figure 1.2b, the crack network is present through which the molecules can pass freely. The difference between leakage and permeation is only signified when looking at the number of molecules that pass from one side of the material to the other one [5]. Usually, the experiments prove the difference to be in a few orders of magnitude. Hence, even if the permeation is negligible through the material, the leakage might still be critical [105].



(a) Permeation of molecules through the solid material, as a diffusion-driven process

(b) Example of connected cracks inside the laminate as a crack network and a free passage of molecules [49]

**Figure 1.2:** Diffusion-driven process of molecules transport in Figure 1.2a and free passage of molecules through the crack network in Figure 1.2b

## 1.4. Experimental testing methods

Currently, testing is the only proven way to obtain accurate values for permeation and leakage for the composite material. The physics phenomenon driving the permeation and leakage of composite materials has yet to be entirely understood. The interactions of fibres with the resin and the influence of thermo-mechanical loading on the material are incredibly complicated and require extensive research to push the understanding further. Possibly in the future, the costly experimental work will be replaced by the simulations and numerical analysis that are currently being developed [90], [74], [47]. And even in this case, the models must be validated against the experiments. That's why understanding the physics of testing is still crucial to obtaining accurate and representable results for the composite hydrogen tank development. That's why the experimental work must be understood first to solve the permeation and leakage concerns.

Many types of experiments are performed in the literature to determine the permeation levels or at which point the material is prone to leakage. Those experiments are done at different geometries and sizes of the specimens. Starting from the simple coupons and ending at small-scale tank models. This variation can be overwhelming. Hence, to provide a general overview of the testing methods present in the research, different levels of permeation testing are introduced here. The levels presented in this study are based on the standard hierarchy of material testing, following a triangle testing structure.

Firstly, coupon-level testing is presented, where the specimen usually has a very simple geometry and is relatively small. After that, the element-level testing is described for the more complex specimen shapes. Then, the sub-scale testing is mentioned, where the testing is done on the small-scale versions of the tank. Finally, full-scale testing is presented for the experiments done on the actual tank.

### 1.4.1. Coupon level testing

Coupon-level testing is the most popular way of testing material for permeation and leakage as it is relatively simple. The geometrical shape of the specimen used in this type of testing is very straightforward, as it can be almost anything. Conversely, this lowers the operational cost of coupon-level testing compared to the other testing methods. This is because there is no need for special equipment and tooling for more intricate specimens. Despite the low cost, this method is usually the least accurate and is used for the first material screening [43].

This method generally consists of the specimen being connected on one side to a medium gas like helium or hydrogen. In contrast, the other side of the specimen is kept under vacuum conditions. The difference in the concentration of molecules on both sides of the sample creates the movement of the molecules, which was shown in the Figure 1.2a. Then, the molecules that pass through the material are quantified. The counting process of the molecules is done in many different ways, like manometric, volumetric, or leak detector method, and is further discussed in subsection 1.4.5. The leakage and

permeation values for the specific materials can be obtained from that.

In literature, coupon-level testing can also be performed by applying thermal or mechanical load to the specimen, increasing the representativeness of the test. Thermal loading is done by submerging the specimen in the cryogen bath [9], [5], [25] or placing the material specimen in the cryostat environment [92], [51], [66], [23]. Sometimes, the thermal loading is also done by custom-made devices and instruments like in the case of Grenoble et al. special cooling container [42], or cool head in the case of Friese [36].

For most mechanical load testing, the specimen is placed in the tensile testing machine [41], or significant pressure is applied to one side of the specimen [68], creating in-plane loading. Unfortunately, the loading obtained, regardless of the method used, does not represent the full-scale tank conditions. Coupon-level testing is regarded as a material screening step, even with an additional stress state imposed on the specimen and the temperature loading. The structure and loading conditions present in the CFRP tank walls are much more complex. Hence, more advanced testing is required to stimulate these conditions, for example, element-level testing.

### 1.4.2. Element level testing

To increase the representativeness of the test by being closer to the actual hydrogen tank conditions, the specimen needs to have a more complex shape. This way, the stresses present in the material can be matched closely to the tank state. Also, the dependency on the curvature and roundness can be better estimated. That's why some researchers tested the CFRP material for permeation or leakage by building specially shaped specimens.

The shape of the hydrogen tank from the literature should be tubular with semi-spherical or elliptical end-caps [39]. Hence, the specimens used to measure the permeation of the material should also resemble the actual tank shape. Based on this, the permeation on the element level is usually done on the tubular specimens [63], [104] or by imitating the end-cap shape [30], [54], [81]. In most cases, how the permeation is measured depends on the actual setup by one of the methods described in subsection 1.4.5. The load can be applied by pressure, external loading or special grips and the thermal loading is usually achieved by cryogenic liquid submersion or cryostat cooling.

The multi-axial testing method is one approach that doesn't necessarily follow the explanation but requires specially designed specimens. Hence, it should be placed in the element-level testing category as it increases the representativeness of the experiments but can't be defined as small-scale testing. In Japan, Hamori et al. [46] and Kumazawa et al. [62] opted for this type of setup. Similarly, the multi-axial testing rig was used in the USA to develop the CCTD project [54]. In such a setup, the stress state can be accurately matched to the tank conditions where hoop and longitudinal stresses don't match each other like in the tubular section. However, a curvature of the tank can't be captured using this method as the specimen is flat.

Despite the multiple different approaches of the element-level testing, certain limitations still exist, and to increase the representativeness of the experiments, the sub-scale testing method is needed. A more complex, tank-like specimen should be used to obtain even more accurate permeation and leakage testing results.

### 1.4.3. Sub-scale testing

Even though the element-level testing setups are, in most cases, capable of achieving conditions similar to those in the actual tank, they tend to be expensive and complicated to perform. That's why, in specific scenarios, it is easier to go directly to a small-scale version of the tank or a bottle test.

The sub-scale testing is usually the last step in the testing planning before the actual tank test is performed. It is typically done to save costs and allow for a few iterations if necessary. Testing is also much safer as the volume is much smaller than in the case of the actual tank.

The sub-scale level testing is usually performed by pressurising the miniature version of the tank with hydrogen and observing the leakage or measuring permeation over time. On the other hand, the temperature loading is achieved by filling the tank simply with liquid hydrogen or during the pre-tests with liquid Nitrogen [101].

In Europe, this type of testing on a small scale was performed by MT Aerospace for the development of the Ariane upper-stage hydrogen tank [101]. While in the USA, NASA conducted a few special tests at this scale before moving towards the actual tank [100]. One such test was done as part of the CCTD program, where the tank was downscaled to only a 2.4 m diameter version.

#### 1.4.4. Full-scale testing

Despite all the effort at the previous stages of the experimental work, the final testing of the full-size tank or slightly smaller version of it is often still required. It is still the only way to qualify a new tank, check all the operational conditions, and ensure that the tank stays intact and doesn't leak.

Unfortunately, this type of testing is costly as it requires a large-scale prototype that is tested to its limits and can't be reused for future projects. Furthermore, most hydrogen tanks have diameters in the range of a few meters, which means the facility where the test can be performed has to be big and capable, which drives the cost even further. That's why only a few full-scale tests of the composite hydrogen tank were performed. At NASA, the X-33 tank, the CCTD tank and finally, the Boeing prototype tank for the SLS upper-stage tank were tested in operational conditions. It is known that the most recent test was a complete success, but the X-33 tank experienced a catastrophic failure. In contrast, the CCTD tank had some issues during testing but ultimately achieved the allowable permeation value [67], [55]. The permeation testing in those types of tests is either done by measuring the decrease in the pressure inside the tank or by sniff test outside the test specimen. In some cases, the permeation measurement can also be performed locally, as it was done for the CCTD tank, where the flexible permeation setup was placed locally on the tank's surface [31].

After all the different methods for permeation testing from the literature have been described, the testing triangle, including all the categories, can be presented. In the Figure 1.3, the testing categories are visually represented, where the width of each level refers to the frequency of occurrence in the research.

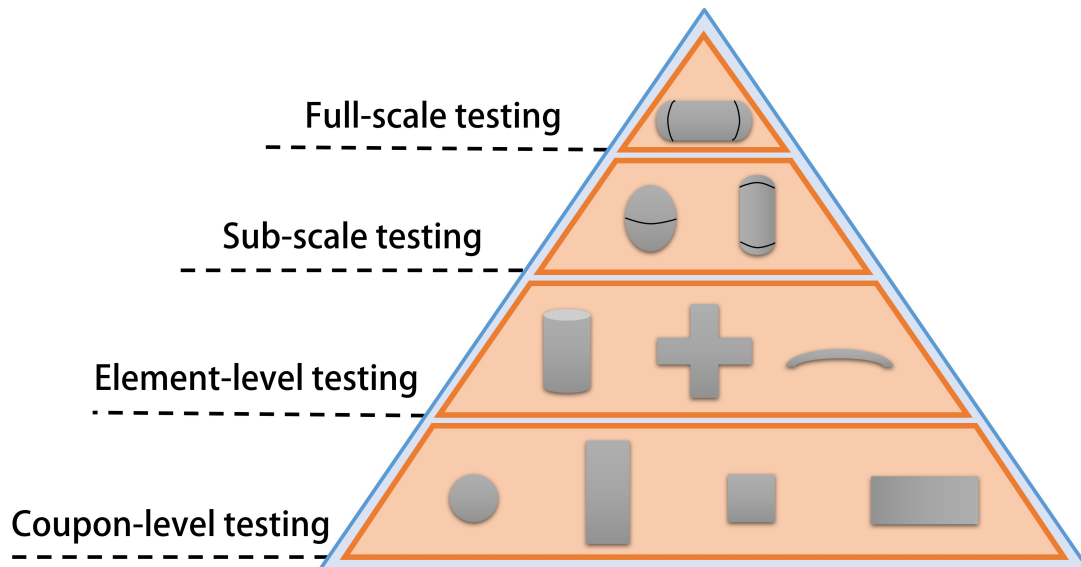


**Figure 1.3:** Testing triangle: Overview of different permeation testing methods in the literature and grouped into different categories.

#### 1.4.5. Methods of measurement

Regardless of the test setup or the specimen complexity, all permeation measurements are done almost exclusively using one of the three most common methods. In essence, permeation is defined as the amount of gas that passes through the solid material per unit of area, a unit of thickness under the unit of pressure gradient and a unit of time [19]. All the variables necessary for the permeation can be obtained with standard measurement methods, except for the number of gas molecules passing from the material. Different methods have been developed and used in the research to measure the number of gas molecules. Each of the methods is fundamentally different from each other, which means all of them have their advantages and disadvantages. Hence, all of them are presented below with specific examples from the literature if present.

##### Monometric method

Firstly, the monometric method is discussed, where the typical schematic of the testing setup is presented in Figure 1.4a. The monometric method uses mercury to determine the rise in pressure. The

sealed side of the specimen is evacuated, and any molecules that pass through the specimen cause the mercury to fill the reservoir slowly. Even though the monometric method seems simple, it is very rarely used. Mercury is a very toxic substance, and the calibration of the entire setup is challenging due to thermal expansion and sealing issues.

#### Volumetric method

A much more common method in literature to measure permeation is the volumetric method. The simple schematic diagram of such a setup is presented in Figure 1.4c. The bottom pressure chamber is open and subjected to atmospheric conditions. The transmission of the molecules through the specimen is measured by the increase in volume indicated by the liquid slug movement per unit of time. Then, the gas transmission rate is calculated using ideal gas law, which can later be changed to the permeance by applying a pressure differential across the specimen. Finally, the permeability is obtained by simply multiplying permeance by the specimen thickness [19]. A very accurate pressure sensor usually replaces the liquid slug in more recent setups. Due to the simplicity of this solution, the volumetric method was used in the following studies [19], [43], [59], [16], [103], [63]. Some researchers also tried to improve the accuracy of this method by creating unique models, for example, the quasi-steady method for permeability determination [56].

#### Leak detector method

One of the biggest problems with monometric and volumetric methods of measuring permeation is that they can't distinguish between different gas molecules passing through the measurement chamber. This is especially problematic if the seal used for the measurement has to be validated. That's why some researchers started implementing gas analysers or mass spectrometers into their measurement equipment [9], [23], [108]. Nowadays, all those instruments are placed in a leak detector package, as seen from the Figure 1.4b. The typical leak detector consists of vacuum pumps and a mass spectrometer that can count singular gas molecules [99]. Most leak detectors can detect Helium or hydrogen atoms. That's why they found their way into the permeability measurement of the CFRP specimens for the hydrogen tank development. Many researchers prefer this option as it registers the leak rate through the specimen straight away and significantly simplifies the entire setup [81], [83], [107], [46], [105], [5], [37], [30], [68], [62], [36], [104], [25], [60], [93].

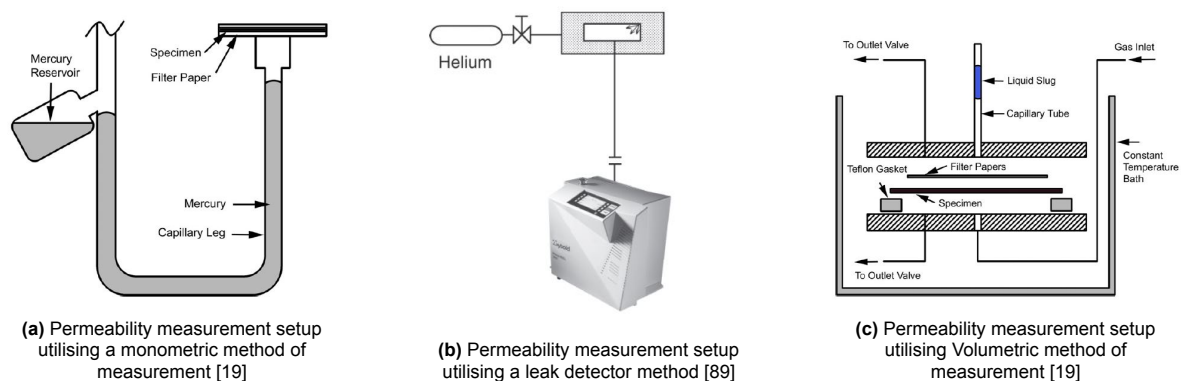


**Figure 1.4:** Graphical representation of the different methods used for the permeation and leakage measurement

Apart from the three presented methods, more straightforward approaches also exist in the literature, but they can be regarded as outliers. In most cases, they are not as accurate as the previous methods, and they can only detect the leakage but can't reliably quantify how severe the leakage truly is. One such method is the leak detection solution, where the foamy liquid is placed on one side of the specimen, and bubbles are observed when the leak path is present [15].

Out of all the methods described above, the measurement using a leak detector is the most common approach present in research. Hence, this method will be only considered for this study. It requires off-the-shelf components and can register helium and hydrogen leakage for the entire experiment duration. Finally, it can also be used to validate sealing and, in general, deliver very accurate results if calibrated correctly.

## 1.5. Research Gap

Looking at the presented literature regarding experimental work, it is clear that coupon-level testing is relatively common, and many researchers worldwide are already doing experiments at this scale. However, according to early NASA studies, "permeation at cryogenic temperatures needs to be evaluated under an applied load to simulate flight conditions" [43]. Hence, testing at the coupon level is not enough to push the composite hydrogen tank's development. However, looking at the other testing scales, Europe, in particular, is behind in the element-level and full-scale testing. In the case of the latter one, it is clear that no examples are currently present as this is usually the last step of the development. On the other hand, the lack of examples of the element-level testing methods in the literature presents a potential research gap. This level of testing, if performed correctly, can provide valuable information as the conditions present during testing can be much more representative than for coupon-level testing. Also, from the research already done in the USA and Japan, it is clear that element-level testing can provide a better understanding of the composite behaviour after thermo-mechanical loading and its influence on permeation and leakage [16], [59], [103].

### 1.5.1. Research question

Based on what was mentioned above, element-level testing presents a gap in research, especially in Europe. That's why this level of permeation and leakage testing was chosen as the future direction of this current research. Elements-level testing promises to deliver accurate results for relatively fast iteration before the sub-components are manufactured to minimise costs. However, despite extensive research in this area in the last 30 years in Japan [46] and USA [78] in particular, how different parameters and variables influence the testing outcome still needs to be determined. Connections between the specimen and the continuous structure of the tank have to be developed. Also, a deep understanding of the relationship between testing parameters and specimen feedback and its connection to the stress state of the full-scale hydrogen tank needs to be improved based on the findings from the literature. Hence, there is a need to determine how testing methods and influencers affect the testing and how they can be adjusted to represent the behaviour of the hydrogen CFRP tank accurately at the element-level testing. That's why the following research question has been developed to direct the efforts of this study and try to fill the gap present in the literature:

Main research questions:

- **How can the element-level testing of CFRP accurately represent the behaviour of a full-scale hydrogen tank on the topic of permeation and leakage**

To support this question, some additional supporting questions have also been developed. The questions have been grouped into two categories. First, the questions about the actual specimen and its relation to testing are outlined. Then, the more pragmatic questions are asked, in which the process of conducting the test is of interest.

#### 1. How to design a specimen for the element-level testing

- **What types of FEM modelling should be used for the specimen design and analysis for the element level testing**
- **How the specimen characteristics influence the permeation and leakage testing**
- **How the open edge specimen shall be designed and tested to represent the continuous structure of the full-scale tank**

#### 2. How to perform a representative permeation and leakage testing at the element level

- **What type of material pre-conditioning shall be performed to incorporate the operational characteristics of the full-scale tank accurately**
- **How tank conditions shall be generated during element-level testing to achieve representable results, such as cooling, boundary conditions, area of measurement, etc.**
- **How different parameters influence the permeation and leakage testing**

# 2

## Methodology

A more detailed look is given to the element-level testing already present in the literature in this chapter to answer the previously posed research questions. Different experimental methods from around the world are investigated and compared. Based on this comparison, the advantages and disadvantages of each approach are derived. Any potential areas of interest for the research are highlighted, including shortcomings and gaps present in the examples from the literature. From those experimental methods, a set of parameters is also defined and described, showcasing their influence on permeation and leakage testing from the literature. Furthermore, the crucial aspects of the hydrogen tank conditions, like the area of equal bi-axial strain, are discussed, which will be investigated later as part of the parametric study. Finally, the experimental research findings are then used to build a numerical model. The previously found parameters in the subsection 2.1.4 are refined and expanded to create the representative research spectrum. Then, the approach for the study of interest is given, starting from the research of the influence of the parameters, followed by the damage analysis and the thermal modelling. A parametric study is supposed to show the testing envelope to confirm that the representative tank conditions can be achieved. Damage analysis, on the other hand, grounds the findings, as it limits the envelope to the usable spectrum only. Thermal modelling gives more of a practical answer to the cooling characteristics necessary to reach the tank conditions. All those studies are done purely numerically, but their characteristics are either derived from the experimental approach from the literature or experience in testing from the Deutsches Zentrum für Luft und Raumfahrt (DLR), which supports this thesis research.

## 2.1. Experimental research and methodology

Element-testing methods for measuring permeation and leakage existed for almost 30 years. One of the first testing rigs was already built and used to investigate the X-33 vehicle failure as described by Robinson et al. [86]. Hence, despite the present lack of research in this field, especially in Europe, much information can be used to guide this research thesis. That's why this section provides a rundown of different techniques from the literature that can qualify as element-level testing. Firstly, a detailed look is given to the cross-setup testing, where the cross specimen is placed in the multiaxial tensile rig to simulate stress-state conditions of the hydrogen tank. Then, the tubular specimen testing is presented; as the name suggests, the specimen is simply a tube to which the load is applied by compression or internal pressure. After that, the bulge specimen testing is showcased, where the circular specimen is subjected to the pressure load to mimic the conditions of the tank end-cap. Each method has its advantages and disadvantages, which are derived from the presented examples. A critical view is given of each approach, and a comparison is presented. Then, based on the findings, a design approach of the testing setup is described that will later be used for the analysis. Furthermore, the operational testing approach is also defined to provide the necessary conditions and constraints.

### 2.1.1. Cross-setup testing

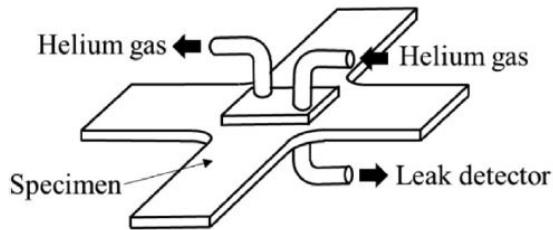
Like any other pressure vessel, a hydrogen tank can have many shapes. However, only one is the most optimal in the case of weight due to the superior stress distribution. Namely, the perfect sphere is the best shape for high-pressure storage. Unfortunately, this shape is rarely chosen due to factors like space efficiency or handling. However, in the case of space applications, the pressurant helium tanks are usually spherical as this geometry provides the most lightweight solution [12]. In most other instances, a pressure vessel is typically extended and can be divided into two distinctive sections: two hemispherical end-cap sections and the cylindrical part connecting both end-caps. In the case of the hydrogen tank development, this shape is also deemed the most probable candidate due to its superior volume efficiency, which is critical for tank placement inside the aircraft cabin [52]. The same goes for the space application, where a cylindrical tank is also preferred due to the sleek design of the launchers. One downside of such a shape is the uneven stress state present in the cylindrical portion of the tank. The stresses in the longitudinal and hoop directions are not equal to each other, as in the case of the purely spherical tank. The difference can be seen by looking at the governing equations for the hoop stress in the Equation 2.1, and for the axial stress in the Equation 2.2.

$$\sigma_1 = \sigma_h = \frac{pr}{t} \quad (2.1)$$

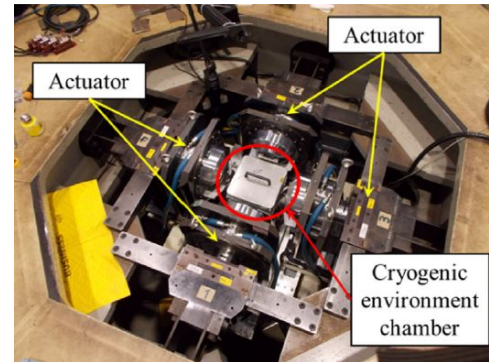
$$\sigma_2 = \sigma_a = \frac{pr}{2t} \quad (2.2)$$

This poses a problem during testing, especially with anisotropic materials like composite for the tank's development, as the standard uniaxial tensile machine is not enough to simulate the loading conditions. That's why special equipment, like a multi-axial tensile machine, must be used. One research group that chose such an approach in their research of permeation and leakage was a group from JAXA. Using a bi-axial tensile machine and a specially designed cross-shaped composite specimen, they could simulate the loading conditions of the tank and its influence on permeation and leakage [61]. In this way, the strain ratios in two primary directions could be adjusted separately. Hence, the typical strain ratio for the cylindrical portion of the tank could be obtained for hoop and longitudinal direction. The picture of such a bi-axial tensile rig can be seen in the Figure 2.1b. Furthermore, researchers from Japan used the environmental chamber to arrive at the cryogenic temperature, as seen from the Figure 2.1b. The liquid nitrogen temperatures were possible to obtain using this approach. However, to the author's knowledge, the permeation measurement for the CFRP specimen using both actuators (mechanical loading) and cryogenic chamber (temperature loading) simultaneously wasn't performed. Mechanical and temperature loading were imposed on the specimen separately but not simultaneously during the permeation testing. Gaseous helium was supplied to the pressure chamber placed on top of the specimen to measure permeation, as seen in the Figure 2.1a. Then, the molecules that passed through the material were measured using a leak detector attached to the specimen on the other side. The helium was delivered continuously to the specimen as both inlet and outlet were present in the pressure chamber.

In general, the cross-setup is a very flexible testing method, allowing for gradual load change in both directions. Also, the permeation measurement can be done quite easily as the specimen is completely flat during the experiment, not posing additional issues with the sealing. Finally, load cycling can be done straightforwardly by cycling the load on the tensile machine. However, the specimen is prone to stress concentrations due to the clamping placement and the overall shape. This proved problematic as the crack propagation can occur from an unrealistic direction, making the test results inaccurate. Other researchers like French et al. [35] designed a special cross specimen to counteract this effect.



(a) Simple schematics of the cross-specimen setup testing



(b) Loading and cooling device used for the cross-specimen permeation testing

**Figure 2.1:** Cross-specimen permeation testing instrumentation present at JAXA [46]

The only other setup resembling the bi-axial setup from JAXA was developed at NASA, but the specimen was strained from 8 different directions there. That testing rig was also designed during the X-33 failure investigation. The specimen was first sequentially strained in two directions, one after the other and kept at cryogenic conditions. After the mechanical and thermal induced damage on the specimen, a circular specimen was cut from the laminate and placed inside the octagonal rig, where the permeation was measured with induced mechanical loading [88]. The sequential uni-axial testing can be seen from the Figure 2.2a [86], and the octagonal tensile rig is presented in the Figure 2.2b [100].



(a) Sequential bi-axial testing under cryogenic conditions presented in the study of Robinson et al. [86]



(b) Multi-axial permeation setup [100]

**Figure 2.2:** Examples of the multi-axial permeation rigs developed by NASA

### 2.1.2. Small-cylinder testing

To achieve simultaneous permeation measurement at mechanical and temperature loading, another setup was developed at JAXA. The schematic of such a testing rig is shown in the Figure 2.3a. This testing method was meant to test tubular specimens under load and cryogenic temperature [106]. Such an approach meant that other composite manufacturing methods could be tested for permeation and leakage. For example, the filament-wound specimens could be tested using this testing technique. To

apply the load, the specimen was strained using a tensile machine attached to the top of the specimen. The cryogenic temperature, on the other hand, was achieved by placing the entire rig into the liquid nitrogen dewar [104]. Helium gas was then applied on the outside of the specimen to measure permeation, creating a gas pocket protected by the special conical shield. Then, on the inside of the specimen, a helium leak detector was connected that measured any leakage through the specimen. Unfortunately, the chosen approach for this specific setup meant continuous permeation measurement wasn't possible. The specimen was strained in a stepped manner, and after the leak detector detected significant leakage, the load was also decreased in a stepped manner. Hence, only substantial leakage was measured after the considerable damage to the specimen had been done.

Another novel approach was developed in France [63], where the tubular specimen was clamped in the special rig, and the tube was pressurised to apply load as presented in the Figure 2.3b. The load application is more representative of this method than the JAXA approach. Still, it also meant that a unique sealing concept had to be developed to avoid any leakage in the sealing area, as the large deformation was present there due to the loading forces. The pressure inside the specimen was continuously monitored to measure permeation. Any pressure drop, in this case, would mean leakage or permeation of helium molecules. The leak detector solution was present to determine where the leakage was coming from on the outside of the tube. The presence of bubbles, in this case, indicated the leakage location. This measurement method was validated against the metallic tube to see if any pressure drop could come from the sealing area [63]. Unfortunately, the setup wasn't meant for the cryogenic application; only room temperature testing was possible.

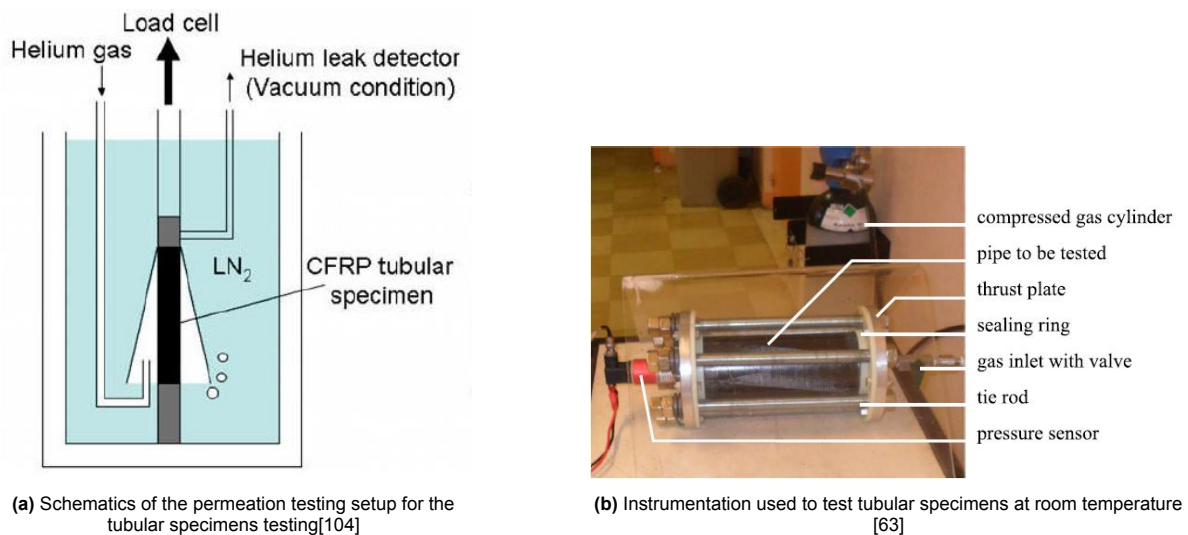


**Figure 2.3:** Permeation setups used for the tubular specimen testing Figure 2.3a by [104] and Figure 2.3b by [63]

A similar approach for testing the tubular specimen was implemented for the CHATT project [93]. The sizeable tubular specimen was placed inside the tensile rig and pressurised with helium. Then, any leakage was detected by the leak detector using the sniffing method. The sniffing method is usually used to detect the leakage area zone, but it doesn't provide accurate values for the magnitude of the leakage. Hence, during this testing, only the location of the leaks was checked.

As seen from the examples, this method provides significant issues at the sealing region if internal pressure is used for the loading. Furthermore, the permeation measurement can't be performed straightforwardly as only pressure drop or sniffing techniques have been used in the literature so far. Accurate permeation measurement would only be possible if the entire cylinder were enclosed, but cryogenic temperature conditions and proper sealing are still significant problems to tackle. However, small-cylinder testing is the only method capable of testing tubes through filament winding, a popular method of creating pressure vessels. Moreover, it can provide representative loading conditions without stress concentrations if designed correctly for the cylindrical part of the tank. However, the loading conditions are not as flexible to adjust as in the case of cross-specimen testing.

### 2.1.3. Bulge setup testing

Both cylinder and cross-shape specimen testing are primarily used to simulate the loading conditions present in the cylindrical part of the tank. However, the other section, namely the end cap, needs a different approach. That's why a bulge bi-axial testing method was developed. Such a setup appeared first during NASA research, where a large membrane was used to represent the endcap of the hydrogen tank. The setup developed then can be seen in Figure 2.4a. In this setup, a relatively thin specimen considered a membrane was clamped between two hemispherical containment shells. The specimen was a one-piece CFRP panel of a hemispherical shape with a radius of around 2000 mm. In this setup, a polar boss could also be placed in the middle of the specimen to examine the influence on the stress concentration and leakage. One part of the containment shell was evacuated to measure permeation, and the other was pressurised with a gaseous medium, helium. The evacuated part was then connected to the measurement instruments, including the residual gas analyser. Stresses on the specimen were imposed by simply increasing pressure in the top part of the containment shell, and the temperature loading was done using the cryostat. Unfortunately, due to the clamping and large force acting on the laminate, stress concentrations were present near the edges of the specimen. Local reinforcement was added to the laminate to counteract this [30].

During the X-33 tank failure investigation, another bulge bi-axial testing rig was developed at NASA at the Marshall Space Flight Center (MSFC). In the case of this setup, the circular CFRP laminate was clamped into the Invar clamping device. The laminate, before clamping, was completely flat. Still, during the assembly procedure, the laminate was experiencing out-of-plane bending due to the slight taper at the edge of the clamping ring. The taper was adjusted as best as possible to match the stresses of the tank and expand the area of equal bi-axial stresses. The entire setup was filled with liquid hydrogen and pressurised to impose stresses and thermal loading. To measure the permeation, a flexible mylar sealing developed by NASA Langley Research Center [84] was used on the laminate's top surface as seen in Figure 2.4b. Finally, the mylar seal was connected to the leak detector, and the permeability of the laminate could be estimated. The measurement area was only 2 in (50.8 mm) in diameter, while the entire specimen was 25 in (635 mm). This was done to limit the measurement to the area where the equal bi-axial zone was present inside the laminate. The specimen was cryo-cycled before placement into the measurement device [88] to impose damage to the specimen and see the operational conditions' effect. After the X-33 failure investigation, this setup was also used in the CCTD project to measure permeation at the early stages of development [100].

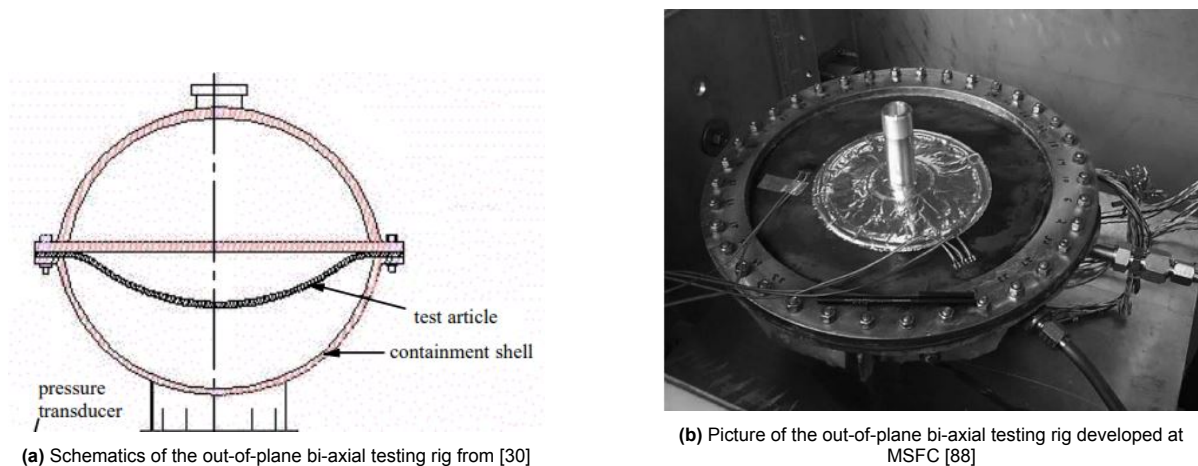


**Figure 2.4:** Graphical representation of the Monometric method Figure 1.4a and Volumetric method Figure 1.4c

Outside of NASA, a similar setup that resembled the bulge bi-axial testing rig was also developed in Europe. The working principle of this rig was almost precisely the same as for the setup designed at MSFC, as seen from the Figure 2.5. However, the size of the specimen in comparison to the NASA setup was much smaller, and the permeation was measured on the entire specimen surface and not only at a specific zone of equal bi-axial strain. The gas pressure created the mechanical loading on the specimen. In this case, helium was used. The entire setup was submerged in the liquid nitrogen bath to reach cryogenic temperature. The leak detector was connected to the chamber above the specimen

to measure permeation [81].

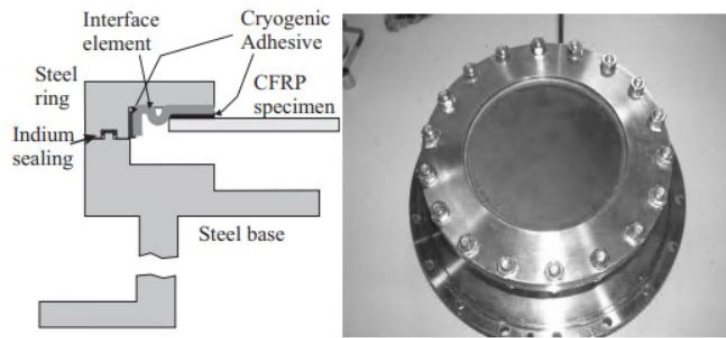


**Figure 2.5:** Out-of-plane bi-axial testing rig for the permeation and leakage measurement developed by Raffaelli [81]

For all the setups presented above, one of the biggest problems was the stress concentration and unequal stresses due to the clamping and open-edge specimen shape. To counteract it, the local reinforcement was used [30], a tapered clamping ring [78] or an elastic interface element [81]. Furthermore, the stress state for all the setups was limited to equal bi-axial strain. This is the only area of the representative stress state of the tank for the end cap section. Moreover, this is also the only method capable of testing polar bosses or feed-throughs that will most likely be present in the actual tank.

Looking at all the presented element-level testing methods that were developed for permeation and leakage testing in the last 30 years, one can see that they are mainly used for different reasons. Hence, despite their disadvantages, they are all necessary to progress the research for developing the composite liquid hydrogen tank. All of them have their characteristics and can't be used interchangeably; for the unequal stress state of the cylindrical part of the tank, only cross-setup testing can be used, while for any filament wound part, the cylindrical testing is the only option available currently. Bulge bi-axial testing, on the other hand, is the best option if the end cap laminate should be tested. However, to answer the posed research question from the previous chapter, only one method will be investigated further and developed into the numerical model. This way, the research focus can be narrowed to fit the imposed timeline.

That's why bulge bi-axial testing was chosen as the main focus of the current research. This decision was made as this type of setup is being developed by the DLR, which supports this thesis research. Factors like the flexibility and capabilities of the bulge bi-axial testing also played a role in this decision. This is mainly because this is the only method able to test end-cap laminates, which are regarded as the most demanding parts, based on the manufacturing limitations for the composites. Furthermore, based on the available literature, it is the only setup capable of performing thermomechanical permeation and leakage testing under representative conditions. Hence, the bulge bi-axial testing results are particularly interesting for the hydrogen tank development.

Other element-level testing methods should also be investigated if the imposed timeline constraints were absent. There needs to be a better understanding of the working principle for all of the element-testing methods, and the development of the hydrogen tank would highly benefit from research in this area. For example, the recent study from French et al. [35] proved that specimen design is crucial for cross-setup testing and can significantly change the results due to crack formation. Furthermore, the tubular specimen testing with the actual permeation measurement apparatus would greatly help design the tank's cylindrical section. That's why other testing methods, even though necessary for tank development, are left as a recommendation for other studies in this field.

#### 2.1.4. Parameters of interest

To develop a bulge bi-axial testing method and answer posed research questions, parameters defining this type of setup should be first understood. Hence, the parameters present in the literature are defined here, where special care is taken to provide their influence on the testing conditions but also the permeation and leakage testing. Firstly, the material-specific parameters are provided where the choice of matrix and fibres and the layup orientation are discussed. The most used combination for the tested specimens is provided, and the choice for the later study is characterised. Then, the loading

conditions during bulge bi-axial testing are presented together with its limitations and dependencies. After that, the testing parameters, such as cooling and gas medium used during testing, are described. Finally, specimen geometry is also characterised, where parameters like thickness, area and curvature are discussed, and a choice is made for the setup development.

### Material and Layup

Most CFRP laminates have relatively similar permeation, as most resins have similar molecular structures [87]. However, the fibre volume content tends to change the permeability of certain materials. The higher the fibre volume content, the lower the registered permeation. This is caused by the fact that fibres can be regarded as an impermeable medium. Molecules can only pass through a much more permeable matrix of the composite [92].

The situation changes while looking at materials that have been pre-conditioned. The most desirable material should be insensitive to cracking due to thermal or mechanical loading. During the first material screening experiments, it was determined that toughened epoxy-based systems outperformed other material choices [87]. Toughened epoxy tends to be more resilient to cracking, primarily due to thermal cycling [18]. The same studies proved that medium modulus fibres work best due to their relative stiffness to the resin. That's why most of the research work for the permeation was done on only a few material systems, like IM7/8552 [81], [36], [30], [78], [35] or IM7/977-2 [37], [80], [38], [42], [15], [59], [74], [11]. Both material systems are characterised by using medium modulus fibre and toughened epoxy. The latter system was used during the development of the X-33 tank [87]. Hence, it was a typical research candidate in the literature for the studies and failure investigation.

Furthermore, during one of the Air Force studies [10], it was discovered that thin plies of composite laminates could act as permeation barriers due to their resistance to cracking. In essence, thin plies are much thinner layers of the standard composite system. Due to their thickness, they seem to inhibit any crack propagation in the thickness direction [11]. And many studies confirmed the initial findings. Hence, thin plies can be found in the tank developed for the CCTD [67]. However, recent studies show that thin plies are not very good at handling out-of-plane loading like impact loading. They tend to cause significant delamination and accelerate leakage compared to standard materials, as shown by Yokozeki et al. [107].

Based on those findings, it was decided that the IM7/8552 is a good candidate for the numerical analysis for the development of the bulge bi-axial testing setup. Other materials candidates are very similar and wouldn't provide vastly different results based on the mechanical aspect. However, this doesn't mean they can't have other results regarding the permeability or leakage value; those must be determined experimentally. The same goes for the usage of thin plies, as despite their proven potential, they will be left out of this study to keep the focus of the research.

The chosen material system with its characteristics can be found in the Table 2.1, which was determined based on the study from the Sheerer et al. [91].

Temp [K]	$E_x$ [GPa]	$E_y, E_z$ [GPa]	$u_{xy}, u_{xz}$ [-]	$u_{yz}$ [-]	$G_{xy}, G_{xz}$ [GPa]	$G_{yz}$ [GPa]	$CTE_x$ [10-6K-1]	$CTE_{y,z}$ [10-6K-1]
77	160	13.3	0.24	0.3	8.65	5.15	-0.19	18.7
293	159	9.6	0.27	0.34	5.01	3.56	-0.05	33.8

**Table 2.1:** Material characteristics at room and cryogenic temperature for the IM7/8552 material system [91]

Aspects like a void fraction or moisture in the laminate were also indicated to influence the permeation and the leakage. However, little research has been done in this area to provide any conclusions. That's why this aspect will be left out of further research and should act as a recommendation for future studies.

In the case of composite laminates, material properties are not enough to fully describe its characteristics. The stacking sequence of the individual layers is also necessary. But this can also change characteristics like crack propagation and, consequently, leakage. That's why the aspect of the composite layup was also researched in the literature. It was shown that the material permeability changes depending on the fibre orientation of the individual layers inside the laminates [11] [62]. However, this change is usually relatively low and can come from other unaccounted variables during testing. However, it was noticed in some studies that cracking, especially through-thickness cracking, depends heavily on the fibre direction of the neighbouring layers. It was shown that a significant change in fibre orientation of more than 45 degrees tends to stop the through-thickness crack propagation [35]. While

for angles lower than 45 degrees, the crack propagation is still taking place [35]. Such a finding confirmed that cross-ply layers resist cracking in the thickness direction better than the quasi-isotropic laminates. Unfortunately, this type of sequence, similar to the thin plies, was also fragile when considering out-of-plane loading. Large delaminations can occur after the impact loading. Hence, significant changes in the fibre directions shall be avoided.

Three symmetric layups were considered for future study to see how the different layups change the thermo-mechanical response of the laminate. All of them are provided in the Figure 2.6. Due to its proven cracking resistance, the cross-ply was chosen as the main configuration, while the other layups were used as an additional study.

$$\begin{array}{ccc}
 \text{QI} = \begin{bmatrix} 0 \\ 45 \\ -45 \\ 90 \\ 90 \\ -45 \\ 45 \\ 0 \end{bmatrix}_s & \text{CP} = \begin{bmatrix} 90 \\ 0 \\ 90 \\ 0 \\ 0 \\ 90 \\ 0 \\ 90 \end{bmatrix}_s & \text{UD} = \begin{bmatrix} 0 \\ 0 \\ 0 \\ 0 \\ 0 \\ 0 \\ 0 \\ 0 \end{bmatrix}_s
 \end{array}$$

Figure 2.6: Chosen symmetric layups for the research

### Loading

From the available element-level testing in the literature, the loading conditions applied to the specimen for the bulge bi-axial testing usually depend on the pressure. In this case, the specimen is regarded as a membrane and deflects in the out-of-plane direction due to the high pressure [68]. The larger the pressure of the gas medium, the larger the stress and strain present in the laminate. However, this type of dependency can be regarded as a significant downside of this testing method. Because pressure or, more importantly, the difference in pressure on both sides of the specimen is also the driving force of the diffusion and, in effect, the permeation. As it can be seen from the equation Equation 2.3, the larger the pressure on the feed side, the higher the flux of molecules. That's also why certain researchers examined the effect of pressure on the permeation measurement. However, the conclusions weren't aligned with each other. According to Rafelli [81], the pressure didn't affect the permeation, while Meng et al. [68] saw the influence of pressure on his results. In both instances, the pressure influence was measured against the leak rate.

$$J_{ss} = DS \frac{p_f^n}{l}. \quad (2.3)$$

To counteract this problem, in some cases, a pre-load was applied to the specimen, creating a certain stress level before the pressure was even applied [78]. Although this would minimise the pressure dependency, the method was optimised for one pressure level only and wasn't actually flexible for other pressure settings. The solution to this problem could be the usage of different pre-loads, but in most cases, this would mean an increase in cost as the pre-load is done through the unique taper metal rings as discussed by S. Oliver [78].

Another issue of the pressure acting as a load is the fact that with the increased pressures, large stresses are also present in the specimen, and significant care has to be taken to minimise the stress concentrations due to the clamping setup. Furthermore, to achieve a realistic stress state of the specimen, the specimen on which the pressure is acting can't be too small as another aspect of loading done using external pressure of the medium is the dependency of the area on which the pressure is acting. From physics, it is known that force from the pressure also depends on the area. Hence, one can increase the laminate area or pressure to achieve an even bigger force acting on the specimen. For the representable results, it is critical not to increase the pressure too much, higher than the pressure in the actual tank. That's why the specimens used in the out-of-plane permeation and leakage testing

tend to be quite large. The diameter of the specimen is in the range from 300 millimetres [81] to 25 inches (635 mm) [78] from the test setups available in the literature.

The literature makes it unclear what pressure to use for bulge bi-axial testing. If the representative testing conditions are considered, the pressure should be in the range of up to 8 bar by the estimate from the European Commission study [3]. However, this pressure might not be enough to reach the representative strains in the laminate if a relatively small specimen is used. According to S Oliver, [78] strains between 0.004 and 0.005 represent the tank conditions. Hence, to obtain representative conditions in the specimen, it was decided that this strain range should be the goal for this analysis. But simultaneously, the available pressure was limited to 25 bar per recommendation from the DLR, as their setup can't reach higher values.

### Testing parameters

Apart from pressure, temperature is also present in the equation for diffusion-driven processes. Permeation is faster at higher temperatures, as the movement of the molecule is also much faster. At low temperatures, on the contrary, because of the low molecular movement, the permeation can even be stopped [51]. In this case, the activation energy necessary for the permeation is higher than the testing temperature. Unfortunately, this is only true for the permeation and not for leakage. The molecules can still pass through the material even at cryogenic temperatures if the leakage path is present [104]. That's another reason why research into leakage is critical for developing the hydrogen tank.

Hence, the results can vary depending on the setup used in the experiment. Many ways exist to cool down the specimen and achieve the cryogenic temperature during testing. However, the achievable temperature is different for each of those methods. In the best case, all the experiments should be performed at the temperature of the liquid hydrogen (-253 degrees Celsius) [5], [85]. Unfortunately, this is rarely possible due to safety concerns or other limitations. Hence, liquid nitrogen [104], helium or cryostat [92], [23], [30], [66] methods are used more often. Although those methods are commonly used in the literature, their effect on the representativeness of the experiment is not entirely understood and should be part of future research. As this analysis is meant to aid the development of the actual setup used in the laboratory, the hydrogen testing was disregarded on safety grounds. Hence, the current research will focus mostly on the temperature of liquid nitrogen instead (77 K).

Similarly, depending on the method and medium used, the rate at which the specimen achieves its minimum constant temperature is also different. This rate influences the temperature gradient present in the laminate. A high-temperature gradient can cause significant thermal stresses in the material. But in this case, this is representative of the hydrogen tank conditions in which the tank will be filled with liquid hydrogen, and the material in direct contact with the cryogen will cool down quickly. In contrast, the other part of the tank will remain relatively warm [58]. However, this also depends on the chosen operational conditions, as it might happen that the tank will be pre-cooled to avoid the large thermal gradients. Nonetheless, rapid cooling is the most challenging for the material, and to keep the results conservative, this condition should be investigated further in this research.

Hence, both the achievable cryogenic temperature and the cooling rate are essential to achieve representable permeation and leakage experiments. That's why those two aspects have to be modelled to see the influence on the stress state of the laminate and notice any limitations.

The hydrogen tank, as the name suggests, will contain hydrogen, and it would seem that hydrogen gas should be used to measure permeation through the CFRP material. And this is true for some of the experiments, especially the ones performed at NASA [85], [5], [41]. Unfortunately, hydrogen is very dangerous, primarily because only 4 % of hydrogen in the air creates an explosive mixture [72]. That's why other gases were used to determine the permeation since the beginning of the hydrogen tank development. One of the most common ones is helium, the closest molecule to hydrogen because of its size. Especially considering that hydrogen is a molecule consisting of 2 atoms, while helium is present in nature as a single atom. Based on the literature, it is understood that helium permeation measurements obtain more conservative results than the ones using hydrogen [81], which is beneficial, at least for the material screening testing. Furthermore, most equipment, like leak detectors, can detect hydrogen and helium. Other gases used for the permeation in literature are argon [43] or nitrogen [56], mainly used because they are inert. However, their usage in the literature was short-lived, and the respective setups were later upgraded to helium or hydrogen, as the results were inaccurate.

Another reason not to use hydrogen is the background noise. In the experiments where hydrogen was used for the permeation measurement, it was detected that the hydrogen had a significant

measurement error caused by the background hydrogen in the atmosphere, even though hydrogen concentration in the lower atmosphere is lower than that of helium. However, the results could be impacted by the equipment sensitivity concerning hydrogen, which wasn't valid for the helium testing. In general, the concentration of hydrogen is measured to be 50 ppb [45], while helium is 5 ppm [77] in the atmosphere.

Despite the benefits of using helium in permeation and leakage testing, hydrogen testing must still be performed. This is the only way to achieve genuinely representative results for any kind of testing. However, due to cost concerns and safety, hydrogen measurements are mostly done at the sub-scale or full-scale level of testing. But in this case, the tank is filled with liquid hydrogen, and both pressure and temperature are the same as the actual condition [101]. For element-level testing, it would also be beneficial to use hydrogen, but in most cases, helium is good enough, as it allows for a quicker turnover between the tests. That's why helium will also be considered in this study.

### Specimen geometry

The final sets of parameters that are influencing the bulge bi-axial testing results are the ones related to the specimen geometry. Thickness, for example, also affects the stress state present in the laminate and not only the area and pressure. This can be explained by looking at the simple form of the stress equation (Equation 2.4, which depends on the cross-section area. The higher the thickness, the higher the cross-section area, which lowers the laminate's stresses. This is especially critical to obtain the right stress state for the correct pressure level. To make the experiment as representative as possible in the element-level testing, the combination of the specimen's area, the specimen's thickness, and the pressure must create the right stress state, representing the one from the tank. However, from the literature, it is clear that it is not always possible, as other aspects also have a role. That's why the best possible compromise must be achieved between all those factors to reach the best possible conditions for hydrogen tank development testing. In future research, all those aspects will be analysed, and their dependencies will be modelled to arrive at the representative testing, indicating any possible limitations.

$$\sigma = F/A \quad (2.4)$$

The thickness of the specimen also affects the physics of the permeation. From the equation Equation 2.3, it is clear that thickness has a particular influence, noted by the letter  $l$ . It doesn't change the maximum permeation level, as it depends on other factors. But it delays the moment when the steady state permeation flux is reached. This can be easily explained by looking at the Equation 2.5, where none of the variables depends on thickness. Thicker laminates are also less prone to leakage as it is much harder for a crack to propagate through more layers. But crack easily due to the cooling as they have higher residual stresses. Unfortunately, thicker laminates are also heavier, and there is a limit to how thick they can be to be still acceptable for the hydrogen tank application.

$$P(T) = P_0 e^{-E_p/RT} \quad (2.5)$$

That's why when this research is considered, a thickness of 2 mm was chosen as a central configuration for the laminate, where each ply has a thickness of 0.125 mm. The entire laminate consists of 16 plies arranged in the cross-ply sequence as discussed in subsection 2.1.4. However, as described above, thicker laminates are of interest and will also be part of the current study.

Apart from the thickness, the specimen area, or, in the case of the bulge bi-axial testing, the specimen diameter is also important, as it affects the measurement area. In almost all cases from the literature, it is limited by the vacuum containment chamber size. The defined testing area is then used to normalise the measured data. In this way, the data can be compared between different setups across different researchers [44].

The testing area also influences the accuracy of the measurement. In the case of the element level testing, the area of equal bi-axial strain is not the same as the area of the specimen. Due to the clamping, this area is heavily limited. Only the centre of a laminate has an equal bi-axial strain, as shown by Oliver [78]. For the MSFC rig, the testing area used during the measurement was only 2 inches (50.8 mm) in diameter, in contrast to the 25 inches (635 mm) specimen size. However, this area was chosen as it delivered representative data of the tank conditions, which is critical for accurate testing. Hence, determining the area of the equal bi-axial strain is vital and will be part of future research. Furthermore, for the flexibility of the measurement, the area of the bi-axial strain shall be maximised.

Hence, clamping, as well as the size of the specimen, shall be optimised for the proper testing area. However, the upper limit of the specimen was set to be around 650 mm as larger specimens would require a significant change of already existing supporting architecture present at the DLR.

On certain occasions, the testing area was also defined across the specimen's cross-section [5]. This way, the permeability and leakage measurements were done for the in-plane movement of molecules. Such a measurement was interesting to see if the movement of molecules in the in-plane direction can happen and how severe it can be.

To summarise, the parameters that influence permeation and leakage testing have been defined based on the examples from the literature. Some aspects like diameter, cooling and testing area were only discussed, and their representative values will only be determined after the analysis is completed. For the other parameters like material system, the IM7/8552 was chosen with the characteristics provided in the Table 2.1. The cross-ply will be used as a layup as a central configuration for the study, but other types, like quasi-isotropic and uni-directional, will also be analysed. Furthermore, the thickness was defined to be 2 mm as a representative example of the specimen geometry. However, the effect of the thickness will be part of the parametric study to analyse the thermo-mechanical response of the thicker laminates as well. Factors like gas medium were only briefly introduced, but the helium properties will be used in thermal simulations, as this is the most likely candidate for testing at the DLR facility.

### 2.1.5. Design approach

After the relevant parameters for the bulge, bi-axial testing has been defined, and some of them have even been determined for the numerical study, almost all the necessary information is available to start the modelling for the numerical analysis. However, before this can happen, certain assumptions and design decisions must be made to streamline the modelling process. From the literature, specific issues for the bulge bi-axial setups have been introduced, such as stress concentrations near the clamping or sealing issues. To avoid these issues in the future, some design decisions can already be made. This way, future numerical analysis can start following relevant geometries and constraints.

#### Shape of the testing setup and clamping aspect

Looking at the examples from the literature for bulge bi-axial testing, one of the most significant differences present is the difference in how the curvature of the specimen is achieved. Estrada et al. [30] proposed already pre-fabricated curved laminate with straight clamping edges. On the other hand, S. Oliver [78] described the method that starts with the flat laminate, and only the assembly step creates a curvature in the laminate. Both approaches are presented in the Figure 2.7. The method provided by Estrada seems more straightforward, but due to the change in the curvature near the clamping, the stress concentration was present in the laminate, and the plate manufacturing was much more demanding than in comparison to the flat sample. In the case of the bulge setup from Oliver, the stress concentration wasn't longer an issue, but the process of specimen assembly was demanding and non-trivial as it required multiple steps. Furthermore, the curvature couldn't be determined purely based on the manufacturing processes. It was a combination of factors like the angle of the taper clamp, the thickness of the specimen and the testing pressure. This contrasts with the actual tank, where the curvature will be defined after the manufacturing step. However, some changes to the shape most likely happen after the pressurisation of the tank, as the elastic deformation will take place.

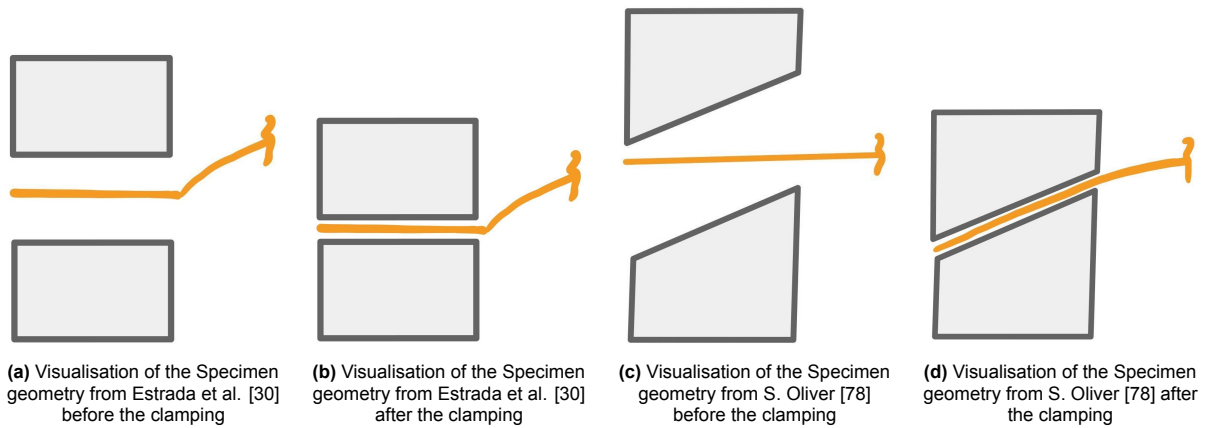


**Figure 2.7:** Specimen geometries from the literature for the bulge bi-axial testing

Considering all these, it was determined that combining both approaches could lead to even better results and should be investigated in this study. Firstly, the taper clamp should be used as investigated by S. Oliver in his thesis [78] to minimise stress concentrations. However, to avoid pre-stressing of the laminate during the assembly procedure, the curvature of the specimen should align with the clamping ring, as depicted in the Figure 2.8. This means that the tested curvature during bulge testing can be defined during the manufacturing procedure. The consequences of such an approach will be investigated during the numerical analysis. Critical aspects already noticed in the previous research include stress concentration near the clamping region, specimen slippage, and equal bi-axial strain area.

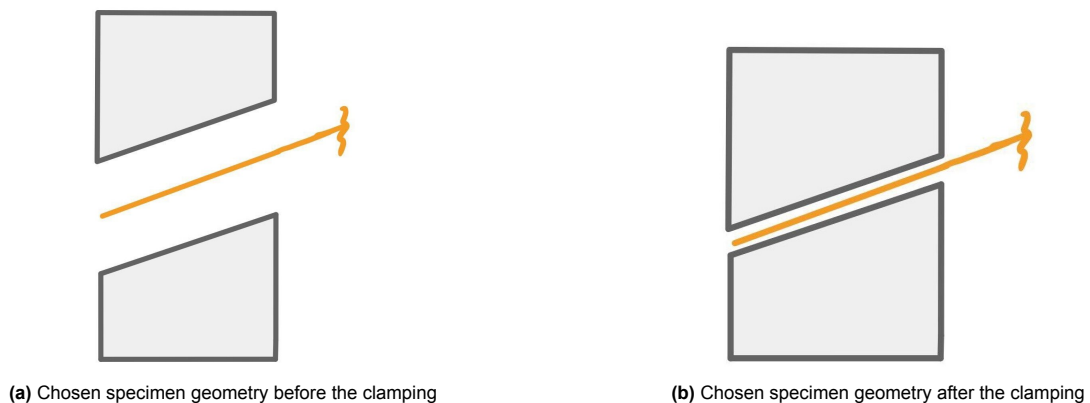


**Figure 2.8:** Chosen approach for the numerical analysis regarding clamping and specimen geometry

As was already discussed, the curvature of the actual hydrogen tank is determined during the design and manufacturing step. Hence, it is recommended to use the correct dimensions for the curvature to create a proper model for the numerical analysis. However, as the aviation tank still needs to be completed, there are no proper references concerning the dimensions of the potential tank. In the case of the space industry, such references fortunately already exist. The future SLS hydrogen tank will supposedly have a tank with curvature of 4700 [mm] based on the initial renders as shown in the Figure 2.9a. The tested CCTD tank had a curvature of 5000 [mm] [100], as presented in Figure 2.9b. However, by looking at the already existing parametric studies of the hydrogen tank that could fit into the existing aircraft airframe, the curvature is around 2000-3000 [mm] [50]. Hence, the decision was made to choose a generic dimension between both reference points, namely 3600 [mm]. These dimensions will be used for the main configuration, but other extremes of the outlined range will be examined during the parametric study to determine the influence of the curvature on the thermo-mechanical state of the specimen.

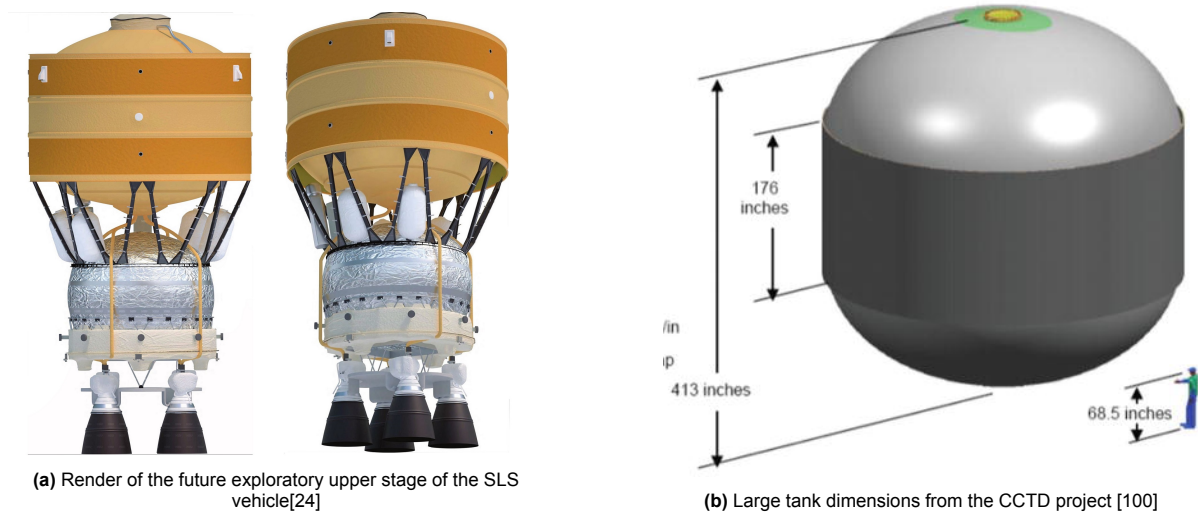


**Figure 2.9:** Tank dimensions for the SLS upper stage and the test article from the CCTD project

### Sealing aspect

Once the clamping and the primary curvature of the specimen have been defined, the proper sealing is another crucial design consideration of the bulge bi-axial testing setup. To achieve accurate and reliable data for the permeation testing, the essential aspect is the tightness of the entire system. This includes all the piping and feed system lines and the primary seal in contact with the specimen. The last one is especially interesting for this study as it influences aspects like clamping area and the out-of-plane compressive load acting on the specimen.

From the literature, a detailed design of the sealing concept is usually not provided, but some general approaches can still be derived from the available examples. Due to the cryogenic temperatures, metal sealing, for example, indium wire, is the preferred option. This type of sealing stays malleable even at very low temperatures and can provide adequate sealing in harsh conditions. In most designs from the literature, the number of seals varies depending on the approach. However, in all the available cases, additional seals act as a redundancy. They provide an additional sealing barrier if one of them fails during the experiment.

That's why a simple redundant indium wire seal will be used in the numerical study to keep the analysis realistic. But, a more detailed look should be given to this aspect in an actual design to avoid any issues with the sealing. However, due to the time constraints, the chosen approach seems adequate, where the seal region will be determined based on the specimen diameter and available sources for the clamping pressures.

### Cooling aspect

Another critical element of permeability testing is cooling. As described in the literature study, many methods were used before to reach the temperature of the hydrogen tank. However, the desired temperature can be reached only by using liquid hydrogen during testing. Unfortunately, this method significantly increases operational demands to perform testing. Liquid hydrogen is dangerous to handle, and special equipment is required to use it safely. That's why, in general, liquid nitrogen is used more often in research. In the case of this study, liquid nitrogen temperature will also be used, but the effect of this simplification will be examined during thermal analysis.

Furthermore, to simplify the thermal analysis, the initial simulations will assume uniform temperature distribution and cooling, simulating submersion cooling conditions. However, those assumptions will later be compared to the results obtained from the thermal analysis. Also, other methods will be examined and compared against the actual tank conditions to determine the most representative cooling approach.

### Other design assumptions

To complete the model design, some other assumptions must also be made. Most importantly, following designs from the coupon level testing and the experience of the DLR, the specimen will be locked entirely inside the metallic enclosure. Hence, this study won't use unique designs like flexible membranes from the thesis of S. Oliver [78].

The metallic enclosure will have a top vacuum chamber connected to the leak detector and a bottom chamber that is connected to the gas supply, in this case, helium. The initial design of such an approach can be seen in the Figure 2.10. From the figure, the specimen's shape can be seen, as well as the redundant sealing and the clamping done through a set of bolts. The exact geometry of the specimen, pressure in the chamber, and clamping force will be determined at the end of the study, as all of those unknowns depend on the previously defined parameters. Based on these research findings, the design recommendation for the actual setup will be made in the end.

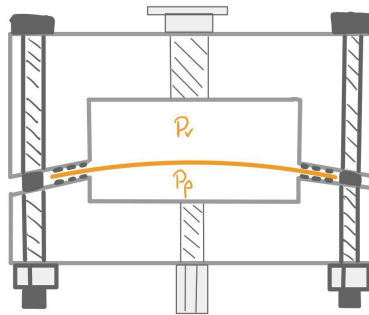


**Figure 2.10:** Initial design approach for the bulge bi-axial testing setup used to build a numerical simulation

Once the initial design has been determined, the preliminary shape of the specimen and aspects such as clamping and sealing are known. This way, the build-up of the numerical model is possible as all the necessary elements of the model are defined. However, before that process can start, the operational conditions during testing shall also be discussed to understand what type of steps will be studied and analysed.

### 2.1.6. Operational approach

Apart from the design aspect, the operational aspect of the bulge bi-axial design must also be discussed and determined. Otherwise, the numerical model won't be adequately defined, or certain elements present in the real-life testing will be omitted. To create the representative testing method, those aspects have to be considered, like, for example, the process of cooling the specimen from the autoclave temperature to the room temperature. That's why the steps that will be present during actual testing will be introduced, and constraints concerning the testing will also be discussed.

#### Steps present during testing

Firstly, the steps the specimen would go through during testing must be assumed. The autoclave step would be required to produce the specimen for the testing made out of composite. Other out-of-autoclave options are also possible, but they won't be part of this thesis. Usage of the autoclave means that the specimen would experience an elevated temperature that can cause thermal stresses inside the laminate during cooling to room temperature. That's why these steps have to be considered, and the numerical simulation should start with the specimen with the elevated temperature. To arrive at conservative results, this temperature was chosen based on the study from Both [13], which was defined to be 407.15 [K] for the IM7/8552 material system. After the specimen reaches room temperature, the assembly process can start, which would end with the clamping step. During this, the out-of-plane compression force would start acting on the laminate. Once the enclosure is secured, it will be cooled down to cryogenic temperature to simulate conditions the material would experience with contact with the liquid hydrogen. Once the temperature is stabilised, the loading step will commence. In this step,

the gas medium will exert pressure on one side of the laminate. To provide the overview of all the mentioned steps, the visualisation is provided in the Figure 2.11.

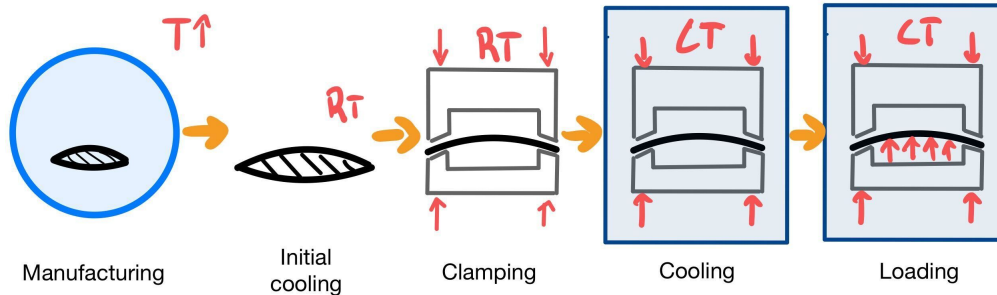


**Figure 2.11:** Assumed steps that specimen would experience before and during permeation and leakage testing with the bulge bi-axial testing approach

These steps were assumed based on the testing practices used by the DLR but also derived from the assembly procedures described by the S.Oliver [78]. Each of them changes the state of the specimen that must be included in the numerical study. Temperature and loading conditions will be defined following this assumption.

## 2.2. Numerical research and methodology

This research, as described at the beginning of this chapter, focuses primarily on numerical analysis to aid the development of the bulge bi-axial testing setup. For this purpose, the ABAQUS 2021 Standard software is utilised. Even though the permeation and leakage testing is the main objective of the future setup, this part is left out of the analysis. Based on the available examples, the investigation concentrates on the thermo-mechanical influence of the parameters defined in the literature. Furthermore, the design and operational approach are used as a starting point to build the numerical model. However, certain simplifications and assumptions must be made first to complete the simulation setup. Then, the parameters that were determined in the subsection 2.1.4 are linked to the model, and the uniform nomenclature for all of them is introduced. Then, the numerical setup is presented where the boundary conditions are defined, together with the steps based on the operational approach. Once that is achieved, the model is verified, where the chosen mesh is checked for convergence, and the right strategy for meshing is chosen. After that, the main parametric study and its chosen methodology are introduced. Based on the findings, the method to evaluate the equal bi-axial zone is also presented there. Following the parametric design approach, the chosen damage analysis is described, with an overview of the considered reinforcements. Finally, the practical aspect of testing is modelled and analysed, starting with the thermal modelling constraints and boundary conditions. In the end, different cooling options are introduced, and the approach to studying them is defined.

### 2.2.1. Simplification and assumptions

Starting with the initial design introduced in the subsection 2.1.5, some assumptions must first be made to streamline the modelling process. Even though the presented model is relatively simple, as it doesn't include details such as pipes and sensors, it still can be considered a large and complex model for Finite Element Modelling simulations. The computer memory would have been used to generate enclosure and sealing, and the runtime of the simulation would have been unnecessarily long. When looking at the defined parameters of interest, most of them are related to the specimen itself and not the entire setup. Hence, most of the initial analysis will be simplified to the specimen analysis only. In essence, the rig's shape highly depends on the final specimen geometry and required conditions that will be derived from the initial results of the analysis. Such an approach significantly reduces the computing time and speeds up the modelling process. However, using this simplification, any effects of the enclosure or sealing on the specimen are neglected. This effect shouldn't be too substantial, as the goal of this

analysis is also to minimise such dependencies. One of the most probable issues is the slippage of the specimen from the sealing due to the difference in the thermal expansion between the enclosure and the laminate, but this effect will also be investigated in a separate study.

To create a realistic model of the specimen itself, the load from the bolts (the clamping) is applied through the pressure load, acting on the outside ring of the specimen as explained in detail in the subsection 2.2.3. The actual loading is introduced by a surface pressure loading acting on the inner area between the bottom clamped region.

Furthermore, all other conditions, such as cooling, are assumed to be perfect. This means that the cooling happens at the entire laminate surface at the same time. The effect of heat convection or non-uniform cooling is wholly neglected.

Finally, the specimen is assumed to be without any defects. This means that the laminate is in pristine condition, without any gaps or voids commonly present in the composite parts after the manufacturing process.

### 2.2.2. Parameters and Variables

Based on the experimental approach, parameters like thickness, material, curvature and layup have been determined for the numerical study. Other parameters, including diameter and pressure, were left as a variable for the analysis. However, one configuration should be agreed upon to start the modelling, to which all other simulations will be referred. Furthermore, all the parameters must be consistently defined across all the studies. Hence, the following approach for defining the parameters used is presented in the Figure 2.12, at least for the curvature, diameter and thickness.

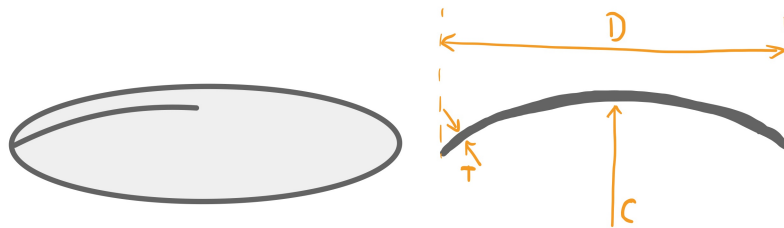


Figure 2.12: Representative of the parameters definition

In the case of the layup, other crucial aspects have to be defined, namely the coordinate system used. For all the simulations, the standard coordinate as defined in the ABAQUS is used as presented in the Figure 2.13. Following the defined directions, the 0-degree plies in the layup follow the X (11) coordinate, where the fibres follow the curvature of the laminate. Similarly, the 90 degree plies follow the Z (33) coordinate.

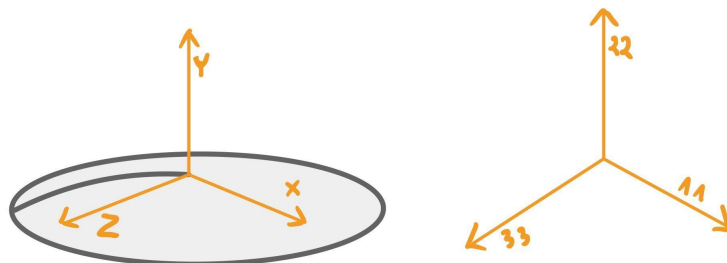
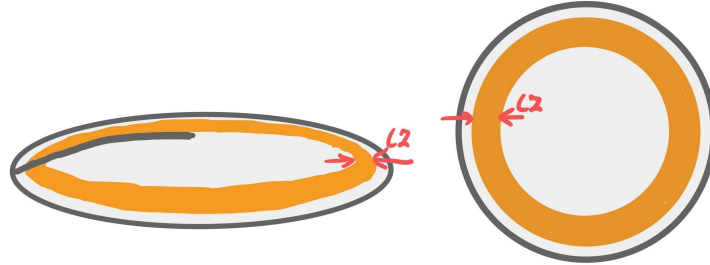


Figure 2.13: Coordinate system used for the numerical analysis

Finally, as presented in the subsection 2.2.1, the clamping force was assumed to be acting on the outside ring of the specimen. This means that the compressive force is distributed over the area that is called the Clamping Zone (CZ) as shown in the Figure 2.14. This area is defined through the experimental knowledge of the DLR, where the 150 mm diameter specimen had around 15 [mm] broad sealing region at the compression force of 110 [kN]. Hence, all other specimen diameters were extrapolated from that point, taking a 5 mm gap from the edge of the specimen as a margin.



**Figure 2.14:** Clamping zone at which the clamping force is applied to

After the clamping zone, all the specified parameters needed to create the numerical model are known. As the main configuration, the specimen with the following characteristics was chosen based on the experimental data and the outlined assumptions: Thickness (T 2 [mm]), Curvature (C 3600 [mm]), Diameter (D 450 [mm]), Layup (CP), Material (IM7/8552), Pressure (20 [bar]), Clamping Zone (CZ 35 [mm]), Clamping Force (900 [kN]). To understand how those parameters are connected and defined, the overview of all the presented specimen characteristics is provided in the Figure 2.15. In this picture, all the necessary zones of the specimen are also presented. The desired outcome of this research is to define how those parameters affect the testing and the specimen design.

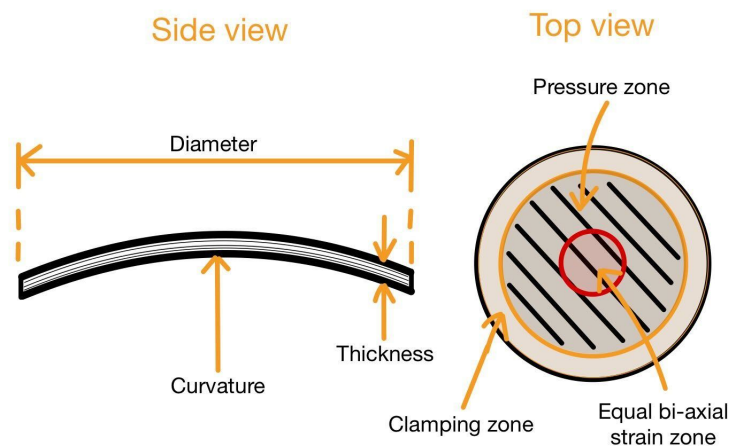


**Figure 2.15:** Overview of all the parameters involved in the numerical analysis research

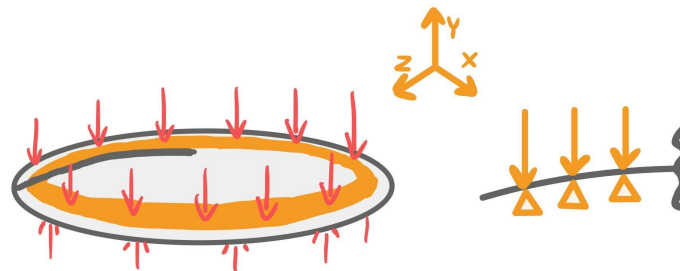
### 2.2.3. Numerical Model Setup

The build-up of the numerical analysis starts with modelling the specimen based on the parameters defined in the previous section. To achieve 2 [mm] thick laminate, each layer of the 0.125 [mm] thickness is created and stacked on top of each other 16 times. Then, each layer's ply orientation is achieved separately to accomplish the cross-ply laminate. Once the specimen geometry is set and the material's properties are defined, the load application and boundary conditions are introduced to the model, where details of that process are described below. Furthermore, the steps for the simulation are set

following the approach from the subsection 2.1.6. Once that is done, the specimen is meshed following the chosen partition approach, and the element type is assigned. Details of the element type and meshing definition are presented below as well.

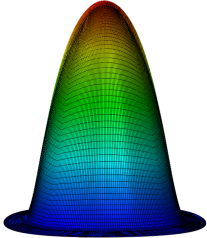
#### Boundary and load introduction conditions

The clamping boundary conditions are introduced to the system to simulate the clamping conditions introduced by the bolt compression force. This is done by applying the constant vertical pressure load acting on the defined clamping zone. The vector of the force is completely aligned with the y-axis of the coordinate system as shown in the Figure 2.16. At the same time, the bottom part of the specimen is constrained in the movement in the vertical direction. The constraint is applied only to the width of the clamping zone.



**Figure 2.16:** Chosen boundary conditions for the clamping of the laminate

The vertical pressure loading was chosen after the tests with pressure loading normal to the specimen surface, which proved to generate unrealistic results compared to the actual conditions. Both options for the clamping were compared to the model where the enclosure was present, and a significant discrepancy was visible for the specimen where the pressure was introduced in the normal direction to the surface. The laminate during clamping was bending inward as shown in the Table 2.2; the deformation is scaled by a factor of 100. This bending, even though present in the more complex model as presented in the Table 2.2, was much smaller and closer to the non-bending conditions present for the model with the vertical clamping force. The difference in the vertical displacement between the different models can be seen in the Table 2.2. Looking at the results, it was determined that the boundary conditions with the vertical clamping pressure are much more realistic than the conditions with the normal pressure for the bulge bi-axial testing setup. It is believed that the bending present for the model with the enclosure is caused by the offset between the edge of the specimen and the line of force from the bolts, and it is highly dependent on how much margin is left between the edge of the enclosure and the specimen.

Type of BC	Actual	Vertical Pressure	Normal Pressure
Deformation scale=100			
U2 displacement [mm]	2.58E-01	7.27E-02	4.31

**Table 2.2:** Effect of the different boundary conditions on the specimen

In the case of the pressure load acting on the specimen, the entire bottom surface of the laminate

between the clamping zone is selected. The force is then perfectly aligned with the vector normal to the surface.

### Simulation steps

As the specimen goes through the different conditions that were outlined in the subsection 2.1.6, the different states have to be also reproduced in the simulation. Five distinctive simulation steps are created following the steps shown in the Figure 2.11. At each step, the conditions of the specimen are adjusted. In general, either the temperature changes or the loading application. To illustrate at what point which force is acting on the specimen or at which temperature the model is analysed, the Figure 2.17 is provided.

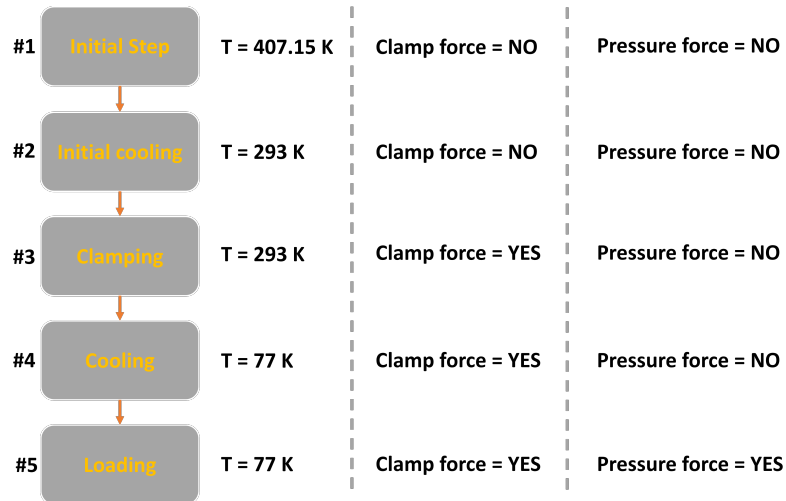


**Figure 2.17:** Steps with different loading conditions and the temperature of the laminate used during the numerical analysis

#### Initial step

During the initial step, the model is introduced. The initial set temperature is  $T = 407.15$  [K] across the entire volume of the laminate. This temperature considers the laminate's elevated temperature during the manufacturing process as explained in the subsection 2.1.6. No other loads are present at this step, and no analysis is performed.

#### Initial cooling

During this step, the end temperature is set to room temperature (assumed to be  $RT = 293$  [K]). This means that the specimen cools down, simulating the normal cool-down process of the laminate after the manufacturing cycle. Thanks to this step, the thermal stresses normally present in the material due to the manufacturing cycle are considered. For the duration of this process, no other forces are present. To avoid the uncontrolled motion of the specimen, one middle node in the model is constrained.

#### Clamping

In this step, the specimen is clamped inside the enclosure. This process constrains the vertical movement of the laminate at the edges. The clamping is imposed on the laminate as presented in the subsection 2.2.3. The bottom part of the laminate is constrained in the y-axis movement, while a clamping pressure is acting on the top part of the specimen. The temperature at this step is still kept at room temperature.

#### Cooling

After the specimen is constrained in vertical movement, it is cooled down to the liquid nitrogen temperature  $T = 77$  [K]. The clamping force during this step is still active but not adjusted. During this

step, the specimen shrinks due to the change in temperature, but the movement is restricted due to the clamping conditions, causing internal stresses.

### **Loading**

At the final step of the simulation, the specimen is subjected to the main pressure loading conditions. The selected magnitude of the distributed force acts on the entire inner area from the bottom of the specimen during this step. To provide accurate results, the loading is done through pressure, as this will be the unit of the force during actual testing conditions. Temperature and the clamping force are active at this step and not adjusted from the last step.

### **Element type**

After the model is set up and all the steps are created, the element type is assigned to the specimen model. As the goal of the analysis is to obtain the most representative conditions for the bulge bi-axial test setup, the solid elements are chosen as the elements of choice. The C3D8R elements are assigned to the entire composite laminate model, following structured mesh partitioning of the given geometry.

The model build-up is concluded once the correct elements are assigned to the model. The specimen with the parameters defined as the main configuration is ready for analysis, but verification has to be performed before this can occur. This way, it can be checked if the model is working as intended and if the process of obtaining the results is efficient.

## **2.2.4. Model verification**

The approach for the model verification includes a mesh convergence, mesh strategy study and verification. The mesh convergence checks if the chosen number of elements is sufficient to obtain reliable results. The meshing strategy looks into the efficiency of the simulation to determine if the most optimal meshing is used. This way, the computing time of the simulation can be optimised while the accuracy of the results stays the same. Finally, verification confirms if the analysis results are actually correct. In the case of this study, due to the lack of representative references from the literature, the verification is done by utilising the semi-analytical solution to a similar problem.

### **Mesh convergence study**

After the model has been finalised and delivers results, one of the first things to do is to check the minimal number of elements used in the simulation to obtain reliable and accurate data. That's why the mesh convergence is performed where the number of elements is increased gradually to see if the analysis results converge and at what point.

For this reason, the set of five different mesh sizes was prepared as shown in the Table 2.3. As can be seen from the mesh pictures, a standard structured mesh was chosen by simply dividing the part into four separate quarters. The choice of the mesh size was decided based on the element number. The goal was to approximately double the element number at each refinement. By comparing the study results at different numbers of elements, the desired mesh size can be then chosen.

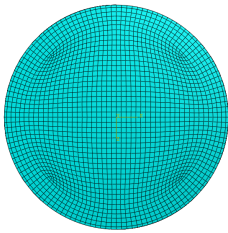
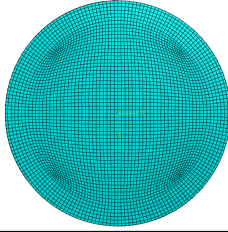
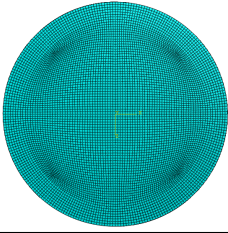
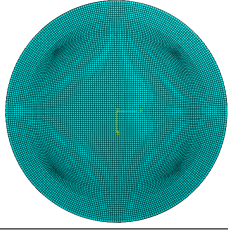
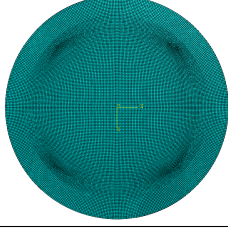
Nr.	Mesh	Element size avg.	Element number
1		10	64343
2		7	120640
3		5	238336
4		4	371040
5		3	673024

Table 2.3: Chosen mesh sizes for the mesh convergence study

**Meshing strategy**

A meshing strategy is also performed to see if the chosen meshing provides sufficient efficiency for future studies. To see how different meshing options influence the results and the computing times, a set of four different meshes is prepared as presented in the Table 2.4. Due to the specimen's geometry, the crucial improvement for the different meshing options is minimising the element distortion. As a result, the first meshing uses a square partitioning in the middle of the specimen to avoid distortions in the centre. The second and the third check the circular partitioning using tetrahedral elements. The results are also referenced to the standard partitioning used for the mesh convergence to provide a complete comparison.

SQS	TET-BIG	TET-SMALL	STS

**Table 2.4:** Set of meshes used in the meshing strategy study

### Verification

Once the right number of elements and the right meshing strategy are determined, model verification can take place. In normal circumstances, the verification would be done using reference models provided in the literature. However, two models that resemble the actual analysis from S.Oliver [78] and Estrada et al. [30] are not truly applicable. The specimen's shape and the assembly procedure used in those studies differ significantly from the approach chosen in this study. Hence, matching the current model to those references would result in an unrealistic comparison.

That's why, for verification purposes, the analytical solution is used. This approach was inspired by the similar verification of S. Oliver [78] for his model.

Unfortunately, the only analytical model found is for the monolithic circular plate, not the composite laminate. However, this is deemed acceptable at this stage as other verification forms were unavailable or not applicable for this particular case. The more advanced models created by S.Oliver [78], Estrada et al. [30] or Raffaelli [81] couldn't be used as a verification as their boundary conditions were entirely different from the ones used for this research.

As an analytical model, the approximate solution for the large deflection of the circular plates with clamped edges by A. Nadai was used [96], as presented in the Equation 2.6, where (a) is the radius of the plate, (q) the distributed load, (E) elastic modulus, (h) the thickness of the plate. This analytical method gives the solution for the mid-point displacement due to the distributed load (pressure, for example), and it agrees very well with the experiments.

$$w_0 = 0.662a \sqrt[3]{\frac{qa}{Eh}} \quad (2.6)$$

The aluminium model is created to perform the verification, followed by the model built-up, using the chosen mesh and number of elements. The edges are clamped, and the pressure is acting on the plate in the same way as for the actual analysis. Then, the results for the mid-point displacement are compared to those found using the A. Nadai solution.

### 2.2.5. Configuration for the parametric study

One of the most critical research questions asked at the beginning of this research is the influence of different parameters on permeability and leakage testing. A parametric study is chosen to determine the effect of the testing variables. This method allows multiple simulations to be run when only one variable is changed at a time. This way, it is possible to determine the influence of each parameter separately.

To start, a set of variables previously defined in the subsection 2.1.4, namely diameter, curvature, thickness, pressure and layup, are used in this study. For most of the parameters, a group of around five variables are chosen, as seen in the Figure 2.18. This number was selected to determine whether

the parameter has a linear or other type of relationship. In the case of the layup, only four layups are tested, and in the case of the curvature, six. For the curvature, an additional flat specimen is chosen as an extreme point, and in the case of the layup, three options were deemed sufficient. The choice of diameter is based on the literature examples, as the smallest setup had 150 [mm] in diameter and the largest one around 650 [mm]. For the curvature, the options are determined in such a way as to cover the entire spectrum presented in subsection 2.1.5 for both aviation and space industry examples. The choice is more or less arbitrary in the case of the thickness, but a 10 [mm] specimen was considered an extreme case as a possible laminate thickness. On the other hand, maximum pressure was already determined in subsection 2.1.4, and other options are chosen to cover the entire spectrum with equal 5 [bar] division. Lastly, the layup possibilities are chosen to see the influence of varied stiffness of the laminate as presented in the subsection 2.1.4.

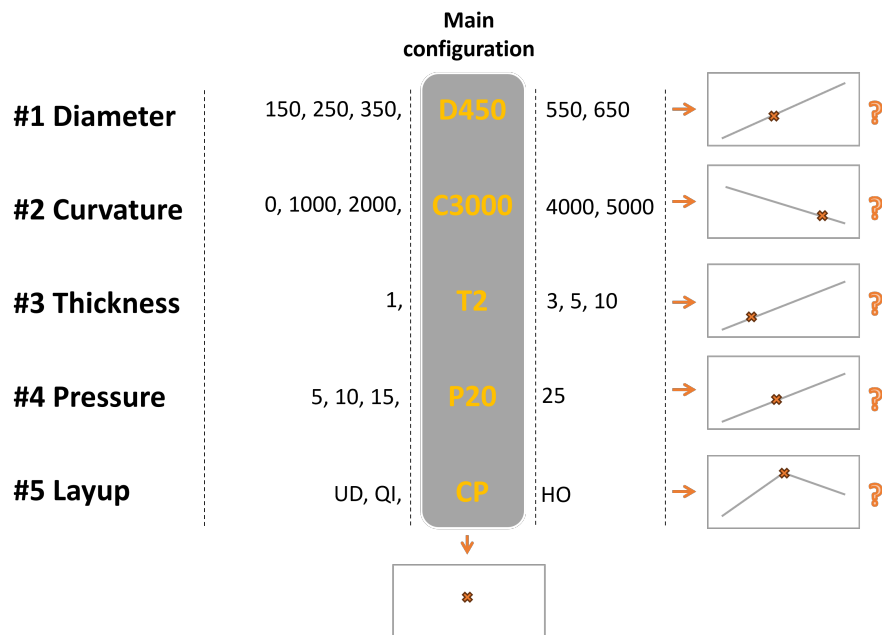


Figure 2.18: The chosen parametric study matrix with all the variables used

A main configuration is used to structure the parametric study as depicted in Figure 2.18. The main configuration acts, in this case, as a central reference point to which all other results are compared. For each analysis, only one variable is changed across the chosen spectrum, while other parameters stay unchanged, the same as for the main configuration. For example, in the case of the study of the pressure effect, the diameter, curvature, thickness and layup are 450 [mm], 3000 [mm], 2 [mm] and cross-ply, respectively, while the pressure varies from 5 to 25 [bar]. This approach allows for a decrease in the number of simulations. Instead of testing the entire spectrum of the possible options, the most essential combinations are analysed instead. The other missing points in the testing matrix are derived from the obtained results.

### 2.2.6. Equal bi-axial zone

During the literature study, it was noticed that to obtain the representative results for the bulge bi-axial testing method, the measurement should be taken only at the zone of equal bi-axial strain, as shown by S.Oliver [78]. This type of specimen stress state represents the actual real tank conditions. It is critical, then, to evaluate this zone for the different parameters and possibly maximise it.

A separate study is performed to see how the parameters tested during the parametric study also influence this zone's size. As a methodology, the approach from S.Oliver [78] is chosen where the equal bi-axial strain was deemed to exist as long as the ratio between the two principle strains didn't vary more than 5 % from the ideal ratio. This means that equal bi-axial strain is present in the laminate as long as the ratio between the X and Z-strain stays between 1.05 and 0.95.

### 2.2.7. Damage Analysis setup and implementation

Generally, composite materials fail differently than standard homogenous materials like metals. It is not enough to look at von Mises's stresses to determine whether the material is still intact. To understand the composite failure mechanism, the damage criterion that checks different failure modes present in the composite material has to be used.

Thanks to the years of research about composite failures, many different damage criteria exist, like Hashin, Puck or LARC05, and can be used in this analysis. Unfortunately, in the ABAQUS 2021 standard, only one damage criterion is fully supported: the Hashin damage initiation criterion. However, in the case of the model used in this analysis with solid elements, Hashin can't be used as its implementation is limited to the shell elements. Thankfully, since the last version of ABAQUS 2021, the new damage criteria called LARC05 can be easily implemented into the model for the Abaqus Standard and works with solid elements.

#### Damage criterion - LARC05

LARC05 is based on the research from Pinho et al. [79]. It can be used for the three-dimensional models implemented in the Abaqus Standard. The LARC05 damage criterion supports both unidirectional and composite lamina.

#### LARC05 - damage initiation criteria

To understand the working principle of the LARC05 damage criterion, one can take a look at four distinctive material failure conditions that are considered in LARC05 presented in Figure 2.19

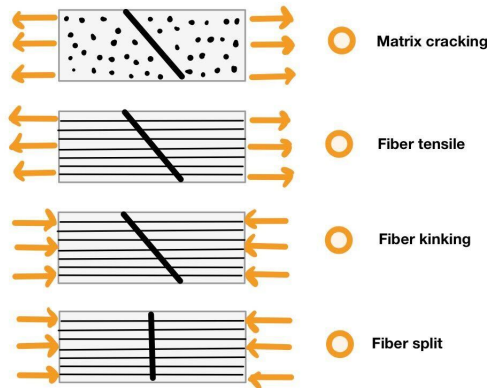


Figure 2.19: LARC05 damage criteria

Each of the presented criteria is defined in the following way:

#### Matrix cracking

$$F_m^{\text{crack}} = \sqrt{\left(\frac{\tau_T}{S_T - \eta_T \sigma_N}\right)^2 + \left(\frac{\tau_L}{S_L - \eta_L \sigma_N}\right)^2 + \left(\frac{\langle \sigma_N \rangle_+}{Y_T}\right)^2} \quad (2.7)$$

Where:

$$\begin{cases} \sigma_N &= \sigma_{22} \cos^2 \alpha + \sigma_{33} \sin^2 \alpha + \sigma_{23} \sin(2\alpha) \\ \tau_T &= \frac{1}{2} (\sigma_{33} - \sigma_{22}) \sin(2\alpha) + \sigma_{23} \cos(2\alpha) \\ \tau_L &= \sigma_{12} \cos \alpha + \sigma_{31} \sin \alpha \end{cases} \quad (2.8)$$

The angle  $\alpha$  denotes the critical plane orientation, which is numerically found, but for this research, the value of 53 degrees is used.

#### Fibre tensile

It is only valid for the ( $\sigma_{11} \geq 0$ ):

$$F_f^{tens} = \frac{\sigma_{11}}{X_T} \quad (2.9)$$

#### Fibre splitting

It is only valid when ( $-\frac{X_c}{2} \leq \sigma_{11} \leq 0$ ):

$$F_f^{split} = \sqrt{\left(\frac{\tau_{23}^m}{S_T - \eta_T \sigma_2^m}\right)^2 + \left(\frac{\tau_{12}^m}{S_L - \eta_L \sigma_2^m}\right)^2 + \left(\frac{\langle \sigma_2^m \rangle_+}{Y_T}\right)^2} \quad (2.10)$$

#### Fibre kinking

Only true for ( $\sigma_{11} \leq -\frac{X_c}{2}$ ):

$$F_f^{kink} = \sqrt{\left(\frac{\tau_{23}^m}{S_T - \eta_T \sigma_2^m}\right)^2 + \left(\frac{\tau_{12}^m}{S_L - \eta_L \sigma_2^m}\right)^2 + \left(\frac{\langle \sigma_2^m \rangle_+}{Y_T}\right)^2} \quad (2.11)$$

Then, the stresses in the fibre-misalignment plane for both fibre kinking and splitting are computed in the following way:

$$\begin{cases} \sigma_2^m &= \sin^2 \varphi \sigma_{11} + \cos^2 \varphi \sigma_{22}^\psi - 2 \sin \varphi \cos \varphi \tau_{12}^\psi \\ \tau_{12}^m &= \sin \varphi \cos \varphi (\sigma_{22}^\psi - \sigma_{11}) + (\cos^2 \varphi - \sin^2 \varphi) \tau_{12}^\psi \\ \tau_{23}^m &= \tau_{23}^\psi \cos \varphi - \tau_{31}^\psi \sin \varphi \end{cases} \quad (2.12)$$

Where  $\sigma_{ij}$  denotes stresses for the fiber-kinking plane:

$$\begin{cases} \sigma_{22}^\psi &= \cos^2 \psi \sigma_{22} + \sin^2 \psi \sigma_{33} + 2 \sin \psi \cos \psi \tau_{23} \\ \tau_{12}^\psi &= \tau_{12} \cos \psi + \tau_{31} \sin \psi, \tau_{31}^\psi = \tau_{31} \cos \psi - \tau_{12} \sin \psi \\ \tau_{23}^\psi &= \sin \psi \cos \psi (\sigma_{33} - \sigma_{22}) + (\cos^2 \psi - \sin^2 \psi) \tau_{23} \end{cases} \quad (2.13)$$

The model keywords must be adjusted to implement the damage criteria to the ABAQUS model. Firstly, the damage initiation criteria are defined based on the known material properties. In the case of the IM7/8552 material system, the following material properties are used for the room and cryogenic temperature, as presented in the Table 2.5, based on the study done by Sheerer et al. [91].

It's important to note that in the case of the LARC05, the in-situ material properties have already been considered. This means that material properties don't have to be adjusted to accommodate the influence of the adjacent layers. Otherwise, an analytical model from [14] should have been used.

Temp [K]	$X_t$ [MPa]	$X_c$ [MPa]	$Y_t, Z_t$ [MPa]	$Y_c, Z_c$ [MPa]	$S_{xy}, S_{xz}, S_{yz}$ [MPa]
77	2700	1700	50	400	170
293	2700	1700	50	200	88

Table 2.5: Material strength properties derived from the work of Sheerer et al. [91]

#### Reinforcement considerations

Possible reinforcement options are also considered in the study to minimise the damage and reduce the chance of specimen breakage during testing. As shown by Estrada et al. [30], the area of the laminate in the close vicinity to the clamping zone is especially vulnerable to excessive stress concentrations. Hence, a circular reinforcement can be added to the specimen to avoid material failure in that region. Other options to strengthen the laminate also exist, but two options are considered for this type of analysis. Metallic and composite rings are placed around the clamping zone, covering the entire zone where the load is applied and some parts of the free laminate. As the centre of the specimen is likely

used for the permeation and leakage measurement, it should be kept free. That's why the considered reinforcement rings don't cover the inner portion of the laminate.

Several reinforcements are tested to understand how the reinforcement affects the laminate's damage, strain, and stress values. Apart from the variability in material, different widths and thicknesses of the reinforcement are also analysed. Aluminium 6061-T6, steel (304 Stainless) and CFRP (IM7/8552) are picked as different material options with the properties for both room and cryogenic temperature taken from the National Institute for Standards and Technology (NIST) [95]. In the case of the thickness, the values of 1, 2, and 4 [mm] are picked, and the reinforcement widths of 60, 80, and 100 [mm] are used as defined in Figure 2.20. To see the influence of each parameter on the specimen, a similar approach to that used for the parametric study was defined, where each variable is changed one at a time. The main configuration in this case to which all others are referred can be seen in the Table 2.6, highlighted in orange. Finally, the influence of double vs single reinforcement is also examined.

The same cross-ply laminate is used in the CFRP reinforcement case. However, the influence of the reinforcement orientation with respect to the specimen is also analysed, where the cross-ply reinforcement is rotated 45 degrees with respect to the specimen orientation.

Parameters	Material	Thickness [mm]	Width [mm]	Sided
Option 1	Aluminium	RT 1	RW 60	Single
Option 2	Steel	RT 2	RW 80	Double
Option 3	CFRP	RT 4	RW 100	

Table 2.6: Reinforcement parameters and variables used in the analysis

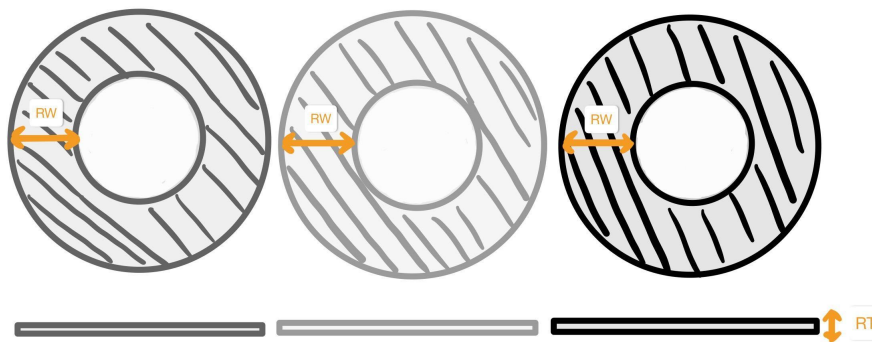


Figure 2.20: Possible specimen reinforcement, with the definition of width and thickness parameter

The approach for the analysis includes the creation of the thin reinforcement ring in ABAQUS, directly matching the curvature of the specimen. To streamline the analysis process, the tie constraint is used to connect the reinforcement to the specimen.

### 2.2.8. Practical testing consideration

The final consideration for this study is the practical aspect of the bulge bi-axial testing setup. The main point for this aspect is the cooling procedure to obtain the required cryogenic temperature. The goal is to investigate different options for cooling and evaluate its practical approaches. That's why, firstly, the thermal modelling is performed where the standard submersion method of thermal load introduction is investigated. This approach is based on the constraints put on the design from the DLR and the boundary conditions derived from the initial design of the testing rig. Finally, the method of evaluating and analysing other cooling options is also introduced.

#### Thermal modelling approach

Three thermal models are prepared to evaluate the bulge bi-axial testing setup's submersion method of cooling. To construct the models, the following material properties were used as presented in the Table 2.7 [97], [102], [29].

Firstly, the model of the entire setup is entirely submerged in a liquid nitrogen bath at a temperature equal to 77 [K]. The liquid nitrogen is assumed to be a perfect sink, and the setup temperature is assumed to be initially at room temperature. Also, the properties of liquid nitrogen are used for the thermal conductivity.

In the case of the second model, liquid nitrogen is replaced with cold gaseous nitrogen, with an assumed temperature of 100 [K]. Similar to the previous case, the setup is also kept initially at room temperature, but the thermal conductivity used in this case is for the nitrogen gas. After the temperature of the testing setup reaches the assumed temperature, the submersion step is done, and the testing rig is cooled to the liquid nitrogen temperature.

The effect of pre-cooling the setup can be examined using those two approaches. Furthermore, the values of the system's heat flux and the cooling rate can be estimated.

Finally, as a last model, the effect of the helium gas is investigated. As the loading step happens after the setup has reached the cryogenic temperature, the helium gas can warm up the specimen, deteriorating the representativeness of the test. That's why, to evaluate this effect, the model is created where the initial temperature of the setup is equal to 77 [K], and the volume used to pressurise the system is replaced with the warm helium gas. The temperature of helium is assumed to follow the curve present in the Figure 2.21. In this case, the initial temperature is equal to 0 degrees [C], and it decays to -196 degrees [C] after around 200 seconds. This assumption was made due to practical reasons, as more detailed estimates would require CFD simulations.

	Conductivity [W/mK]	Density [kg/m3]	Specific heat [Jkg/K]
CFRP	k11 = 4.89	1800	800
	k22 = 0.58		
	k33 = 0.58		
Indium	82	7310	233
Steel	15	8900	420

Table 2.7: Thermal properties of the materials used for the cooling analysis

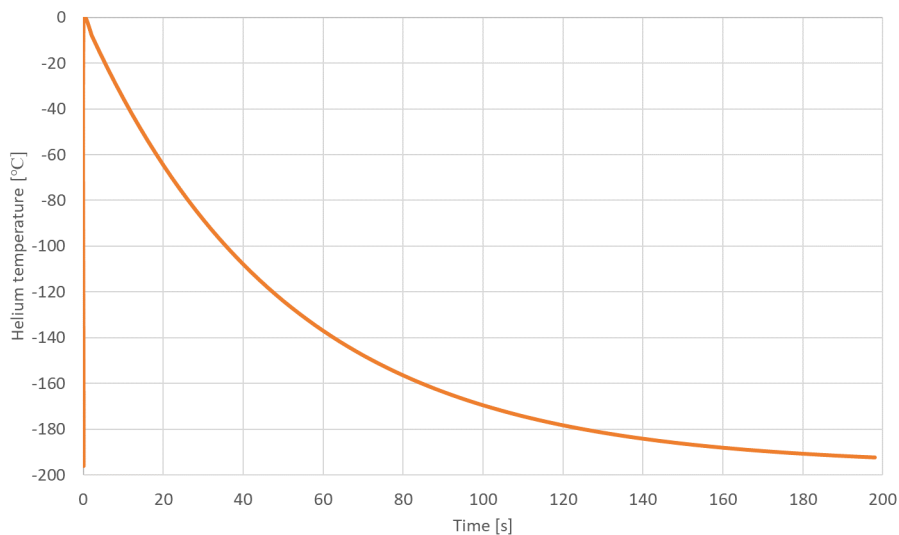
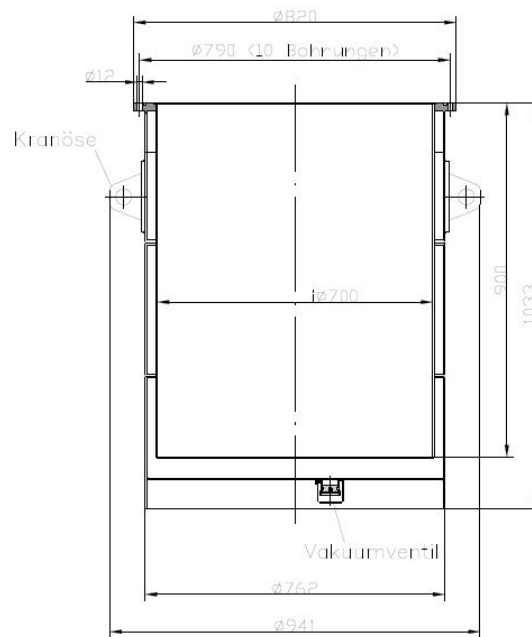


Figure 2.21: Assumed temperature over time of the Helium applied to the system

### Constraints

To make the thermal simulation realistic, certain constraints must be considered. As it was introduced at the beginning of the chapter, the initial thermal analysis will be based on the simple submersion cooling method as it was done by the [81], for instance. In this type of method, the major constraint is the size of the cryogen vessel that is used to store liquid nitrogen, for example. In the case of this research, DLR's large cryogenic Dewar is used as a reference. From this dewar, the dimensions, as

well as the capacity, are known and will be used for the thermal simulation. The technical drawing of this vessel can be seen in the Figure 2.22.

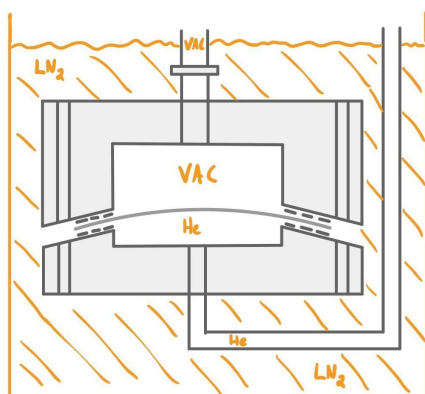


**Figure 2.22:** Dewar used by the DLR to perform the submersion testing

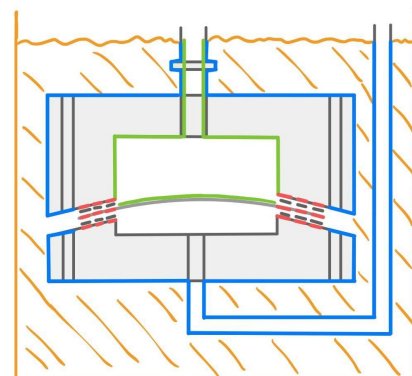
### Boundary Conditions

A different set of boundary conditions must be used to create the thermal model. For this purpose, details like bolt holes, seals and feed lines, as presented in the Figure 2.23a, are added to the initial design of the setup.

Then, different heat flux coefficients are assigned to the surfaces in contact with different mediums like vacuum, liquid nitrogen or helium. Also, the thermal conductivity coefficient is set for the solid elements that are in contact with each other. The different surfaces present in the testing rig can be seen in the Figure 2.23b. For the purpose of simplicity, the thermal radiation present in the vacuum chamber is disregarded. Also, the piping above the liquid nitrogen is only cooled by the cold nitrogen gas at a temperature of 100 degrees [C]. The conductivity between the seals, the specimen, and the enclosure is assumed to be almost perfect, equal to 0.8.



(a) Updated testing setup used for the thermal modelling



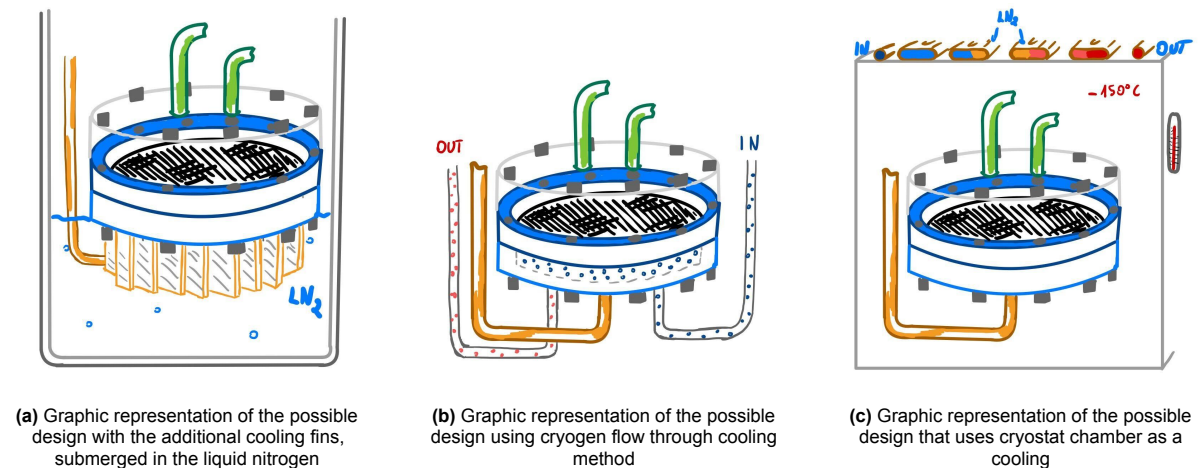
(b) Representation of different boundary conditions present in the thermal model

**Figure 2.23:** Approach for the modelling and boundary conditions introduction for the thermal analysis

### Cooling options

As the final step of this analysis, different cooling options are also considered and compared to the findings found using the submersion method. Compared to the mechanical loading for the bulge bi-axial testing setup, the cooling process can be much more complex. Even looking at the examples from the literature, one can notice various options for cooling specimens for permeation and leakage testing. This means that no one solution could fit all methods, primarily if the experiment aims to measure the specimen's permeation and leakage at the tank's representative conditions. The state-of-the-art techniques use cryostat, cryogen immersion or flow-through systems [42] to cool the specimens to the desired temperature. All the methods have their advantages and disadvantages. Still, the most crucial question for this research is which method can provide more representative testing characteristics for element-level permeation and leakage testing.

Different methods must be modelled first to make this decision and design the right cooling system. The most significant difference between the methods is the cooling rate and the minimum achievable temperature. And the comparison can only be made if the models for different cooling designs are made in the FEM software. This way, the temperature flux can be recorded, and the final state of the specimen can be compared to the hydrogen tank conditions. Possible designs that will be checked and expanded upon are presented below in the Figure 2.24. This testing will be done by adjusting the already prepared model for the liquid nitrogen submersion to create different cooling options. Firstly, the addition of cooling fins will be tested as present in the Figure 2.24a. Then, the effect of cold gas cooling will be examined, where before the helium is applied to the system, the pressure chamber will be filled with cryogenic gas as shown in the Figure 2.24b. In this case, a flow-through system will be tested as the heat could be evacuated in this way. Finally, a traditional cryostat system will be analysed and compared to the submersion cooling method as present in the Figure 2.24c.



(a) Graphic representation of the possible design with the additional cooling fins, submerged in the liquid nitrogen

(b) Graphic representation of the possible design using cryogen flow through cooling method

(c) Graphic representation of the possible design that uses cryostat chamber as a cooling

**Figure 2.24:** Three possible designs for the cooling method of the out-of-plane bi-axial setup for the permeation and leakage testing.

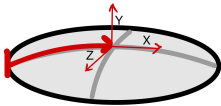
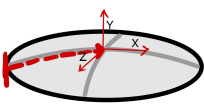
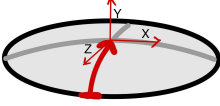
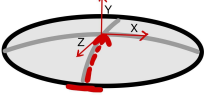
# 3

## Results

This chapter outlines the results of all the proposed analyses from the previous chapter. The effect of each defined parameter is showcased based on the strain and stress results. The damage analysis outcome is also presented to find the suitable characteristics for the specimen, where the influence of different reinforcements is outlined. Finally, the outcome of the thermal modelling is outlined, where the specific heat of the setup and the rate of cooling for the liquid nitrogen submersion method are determined. Furthermore, the cooling performance of other considered cooling options is investigated, where the rate of cooling and the minimum achievable temperature are presented for all the tested approaches.

### 3.1. Parametric study results

In this section, the results of the parametric study are shown. The strain LE11 and LE33 values and the stresses S11 and S33 are provided for different node paths across the specimen. For this set of results, the x-path and the z-path are provided according to the Table 3.1. For most of the results, only the data from the x-path is presented due to the choice of the main layup. However, to see the difference between the specimen sides, the values of stress and strain are plotted for paths and the top and bottom of the specimen. Each path starts at the specimen's edge and continues till the centre.

X-path (top)	X-path (bottom)	Z-path (top)	Z-path (bottom)
			

**Table 3.1:** Chosen paths across the specimen for the results presentation

Each tested parameter is presented separately. Firstly, the effect of the diameter is shown, and then the results of different curvature values are plotted. After that, the strain and stress values are presented for the different magnitudes of specimen thickness and testing pressure. Finally, the effect of the different layups is also shown. The zone of equal bi-axial strain is also plotted for all the different parameters. The graphs are provided for the specimen's top and bottom path, and the assumed strain ratio for the zone is highlighted with an orange colour.

### 3.1.1. Effect of the Diameter

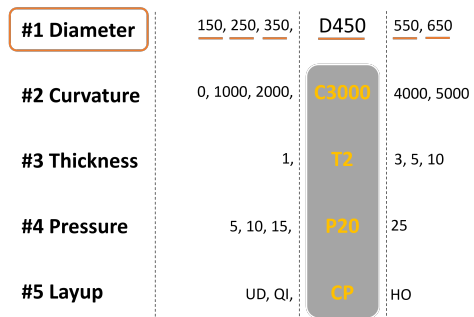


Figure 3.1: Variables analysed for the diameter effect study

The numerical simulations are run for a set of predefined values to see the effect of the different specimen diameters. Six analyses were performed with 150, 250, 350, 450, 550, and 650 [mm] specimen diameters, respectively. Other parameters were set to the values of the main configuration as presented in the Figure 3.1. From each simulation, the values of strain and stresses are plotted following the paths defined at the beginning of the section. Firstly, however, the vertical displacement due to the pressure loading is provided for all different specimen sizes in the Figure 3.2. Each line in the plot represents the outer contour of the laminate after the loading step. As it can be noticed, the

starting point of the displacement for each specimen starts at a different location. This is caused by the clamping zone that is scaled with the diameter. For the largest specimen, the clamping zone continues beyond 50 [mm] into the laminate. Finally, the plot is only shown for half of the laminate, which means the rightmost point is the specimen's centre.

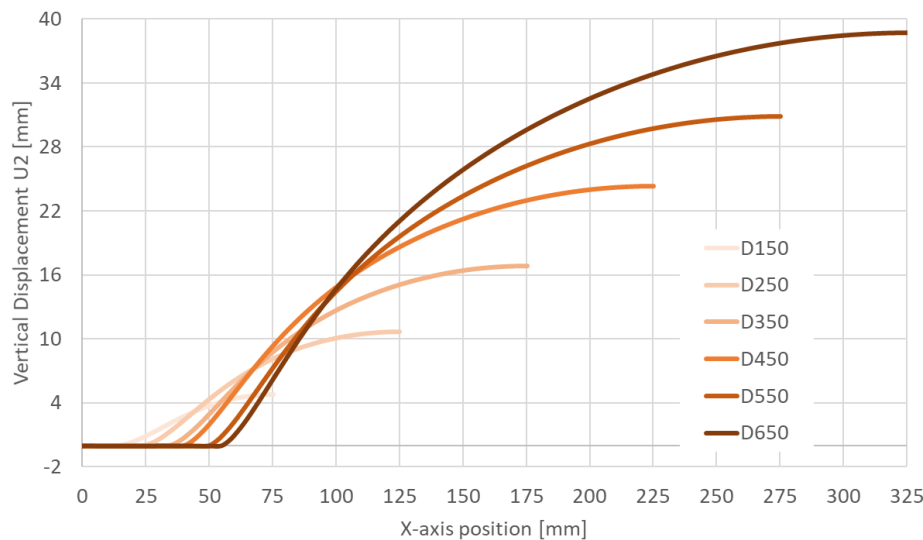


Figure 3.2: Vertical displacement of the specimen for the different values of the diameter.

#### X-path Top

To see the effect of different options for the specimen's diameter, the stress and strain values are provided in the Figure 3.3. Firstly, the values along the X-axis, at the top of the laminate, are shown. Stress S11 in the Figure 3.3a, Stress S33 in the Figure 3.3b, Strain LE11 Figure 3.3c, and finally strain LE33 Figure 3.3d. Once again, the shift in the stress peak between the specimens is caused by the growing clamping zone with the specimen diameter. Each line for both stress and strain ends at the point of half specimen diameter. If the plot continued across the entire length of the specimen, the stresses and strains on the missing side would be depicted as the mirror image of the existing lines.

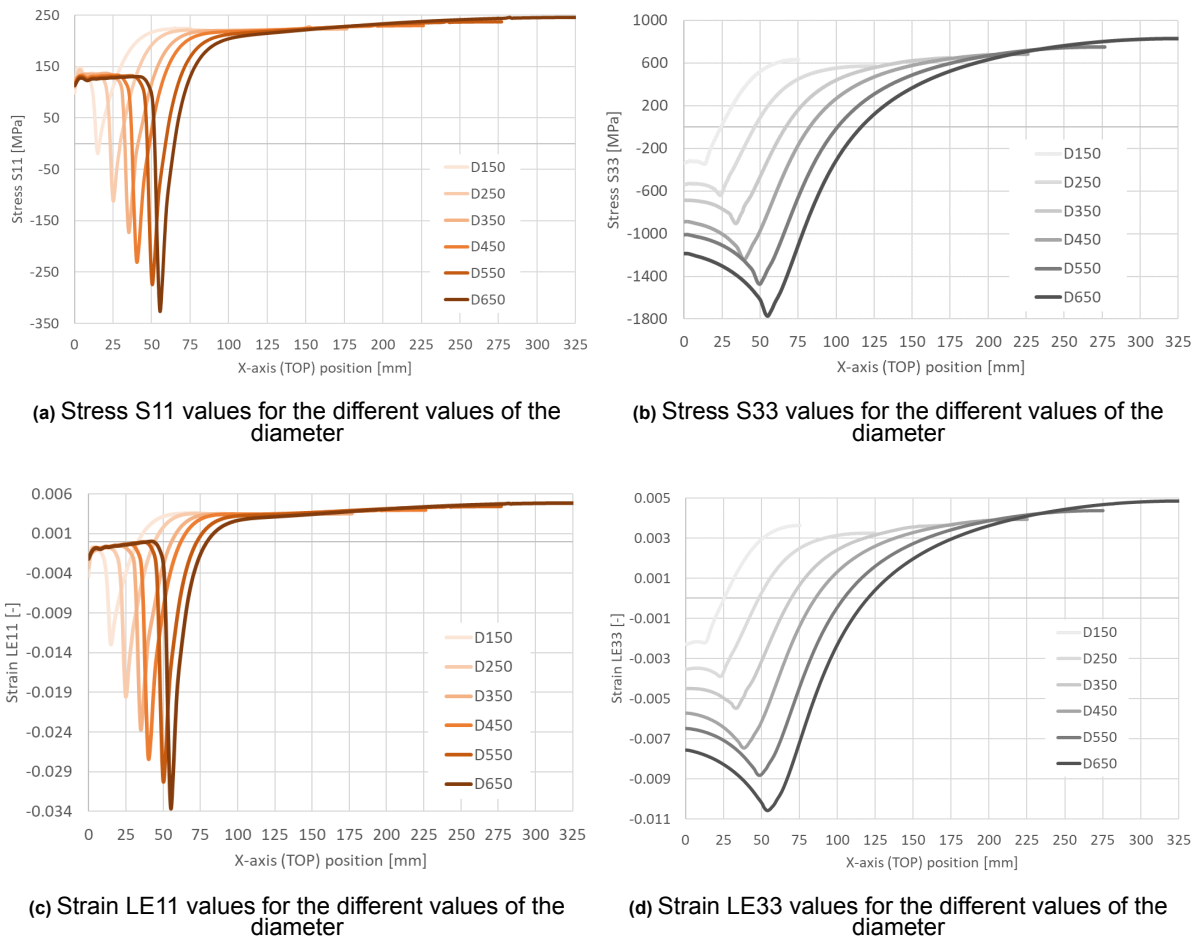
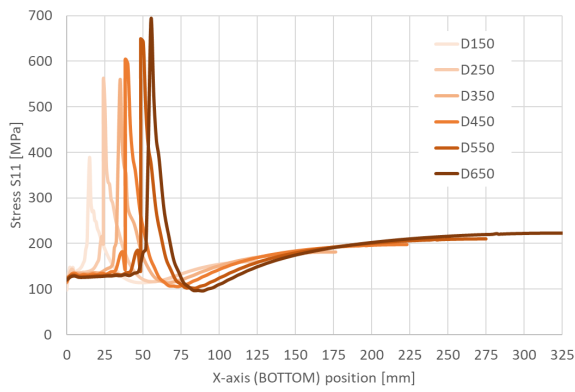


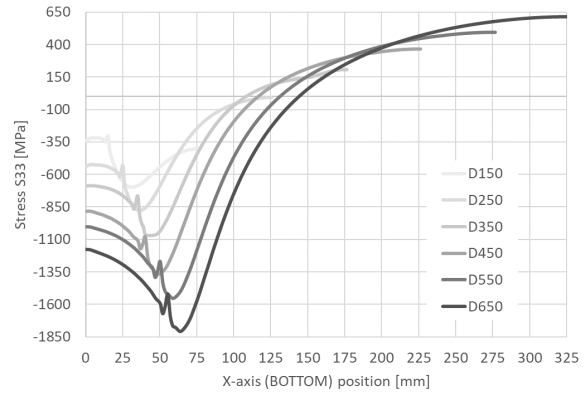
Figure 3.3: Results for the diameter study. Values provided along the X-axis at the top of the specimen

#### X-path Bottom

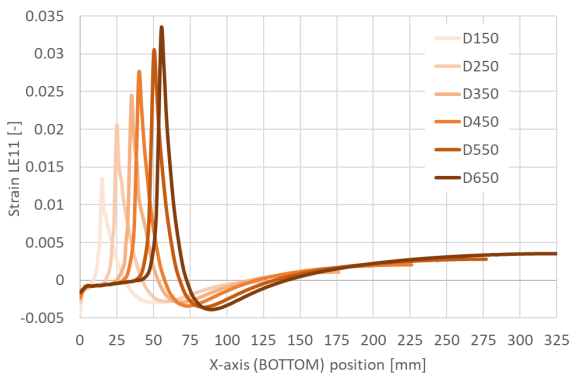
To give better insights into the specimen behaviour, the stress and strain values along the x-axis at the bottom of the specimen are provided Figure 3.4. The results for the Stress S11 in the Figure 3.4a, Stress S33 in the Figure 3.4b, Strain LE11 in the Figure 3.4c, Strain LE33 in the Figure 3.4d. Compared to the top path, the peak stress for the S11 is positive, as the laminate is in tension and not in compression. The specimen is subjected to the bending motion that creates compression at the top and tension at the bottom in the rotation point.



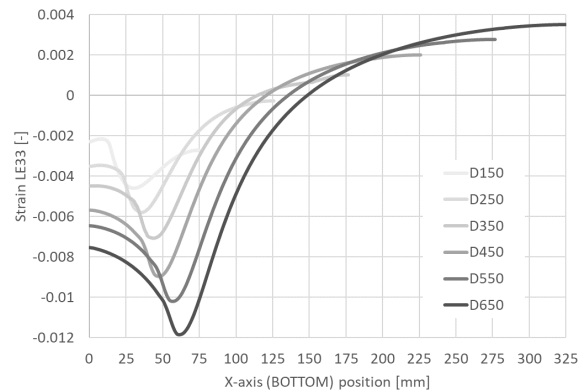
(a) Stress S11 values for the different values of the diameter



(b) Stress S33 values for the different values of the diameter



(c) Strain LE11 values for the different values of the diameter

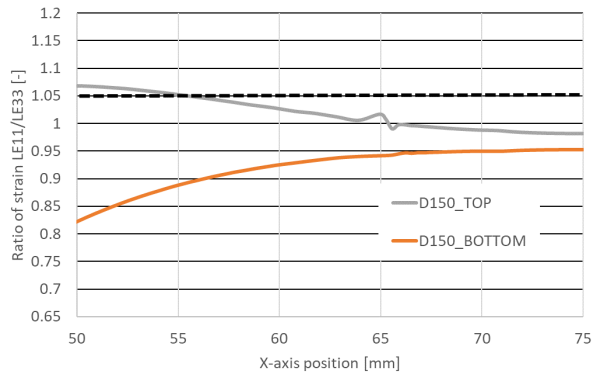


(d) Strain LE33 values for the different values of the diameter

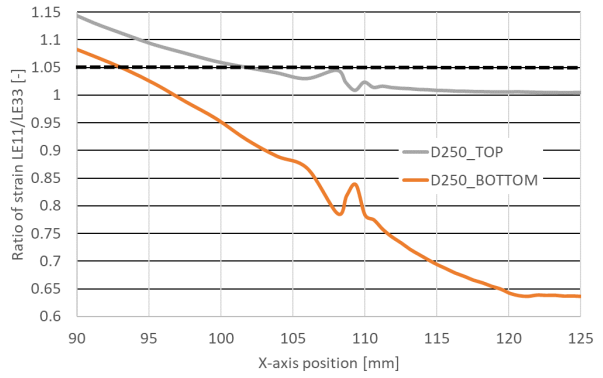
**Figure 3.4:** Results for the diameter study. Values provided along the X-axis at the bottom of the specimen

### Equal Bi-axial strain

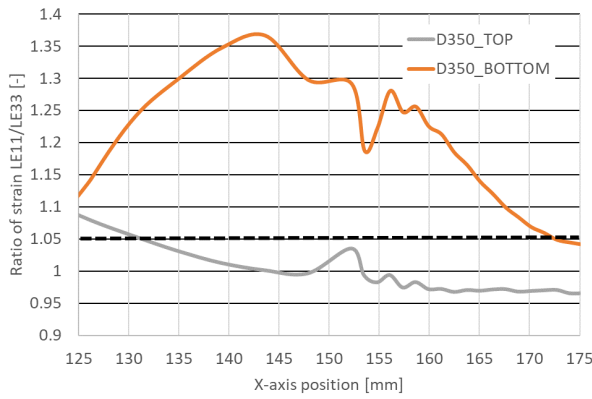
Once the strain values were known for the different curvature values, the strain LE11/LE33 ratio was plotted. The results of this analysis can be seen for both the top and bottom path of the specimen. As all the tested specimens have different sizes, the equal bi-axial zone is presented for each diameter separately. The results for all the derived values can be seen in the Figure 3.5. The assumed ratio for the equal bi-axial zone is highlighted in orange by the dotted line. The position of the X-axis is limited only to the relevant zone. The zone starts in the middle of the specimen and goes outwards until the strain ratio crosses the 5% mark.



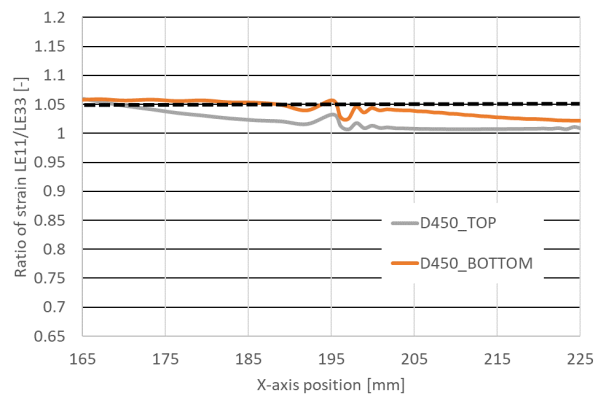
(a) Strain ratio at the top and bottom of the specimen with the diameter of 150 [mm]



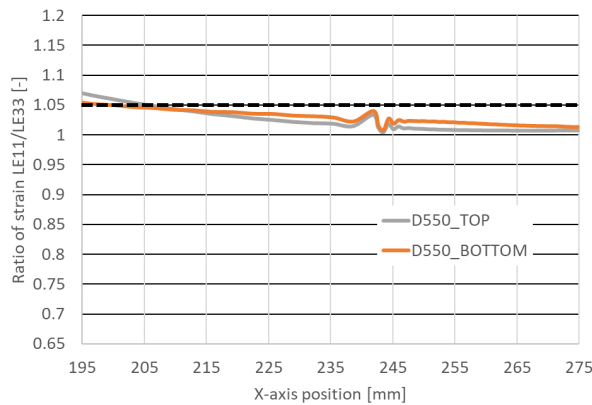
(b) Strain ratio at the top and bottom of the specimen with the diameter of 250 [mm]



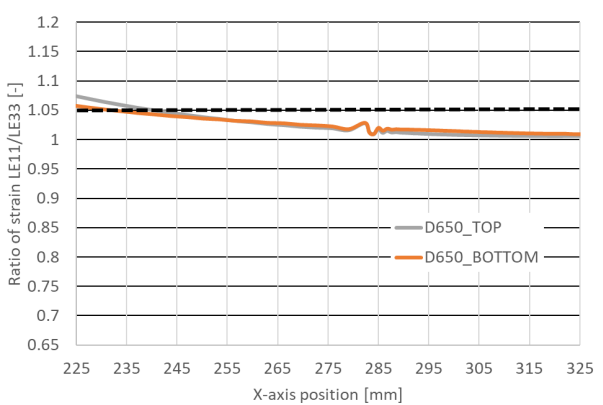
(c) Strain ratio at the top and bottom of the specimen with the diameter of 350 [mm]



(d) Strain ratio at the top and bottom of the specimen with the diameter of 450 [mm]



(e) Strain ratio at the top and bottom of the specimen with the diameter of 550 [mm]



(f) Strain ratio at the top and bottom of the specimen with the diameter of 650 [mm]

**Figure 3.5:** Results of the equal bi-axial zone analysis, concerning specimen diameter for the top and bottom of the specimen

### 3.1.2. Effect of the Curvature

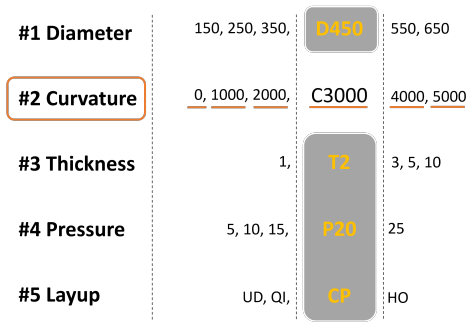


Figure 3.6: Variables analysed for the curvature effect study

Now, the results for the curvature parameter are provided. The tested variables can be seen in the Figure 3.6. Hence, six simulations were run again for the curvatures of 0, 1000, 2000, 3000, 4000, and 5000 [mm]. The rest of the testing characteristics were kept the same as for the main configuration, shown in the grey block.

The results are provided along the path to provide a comparison between the different values of the curvature. Due to the choice of the layup, namely, the cross-ply used in this analysis, only the X-axis path is sufficient to provide the relevant data. However, to gain insight into the specimen's behaviour across the thickness, the results have been provided both for the top

and bottom path of the specimen.

Firstly, however, the outcome of the curvature analysis for the vertical displacement is shown in the Figure 3.7. Each tested specimen is presented as a grey dotted line for reference. The C0000 specimen is simply flat. As can be seen from the plot, each loading displacement starts at the exact location of the end of the clamping zone, which is the same for the specimen with the same diameter. Furthermore, thanks to the reference lines, not only relative displacement but also absolute displacement is visualised.

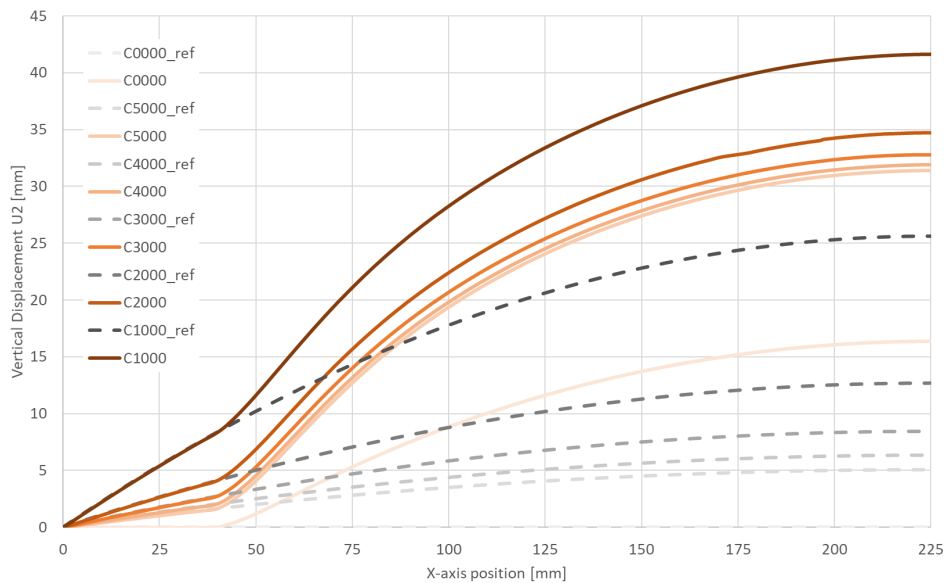
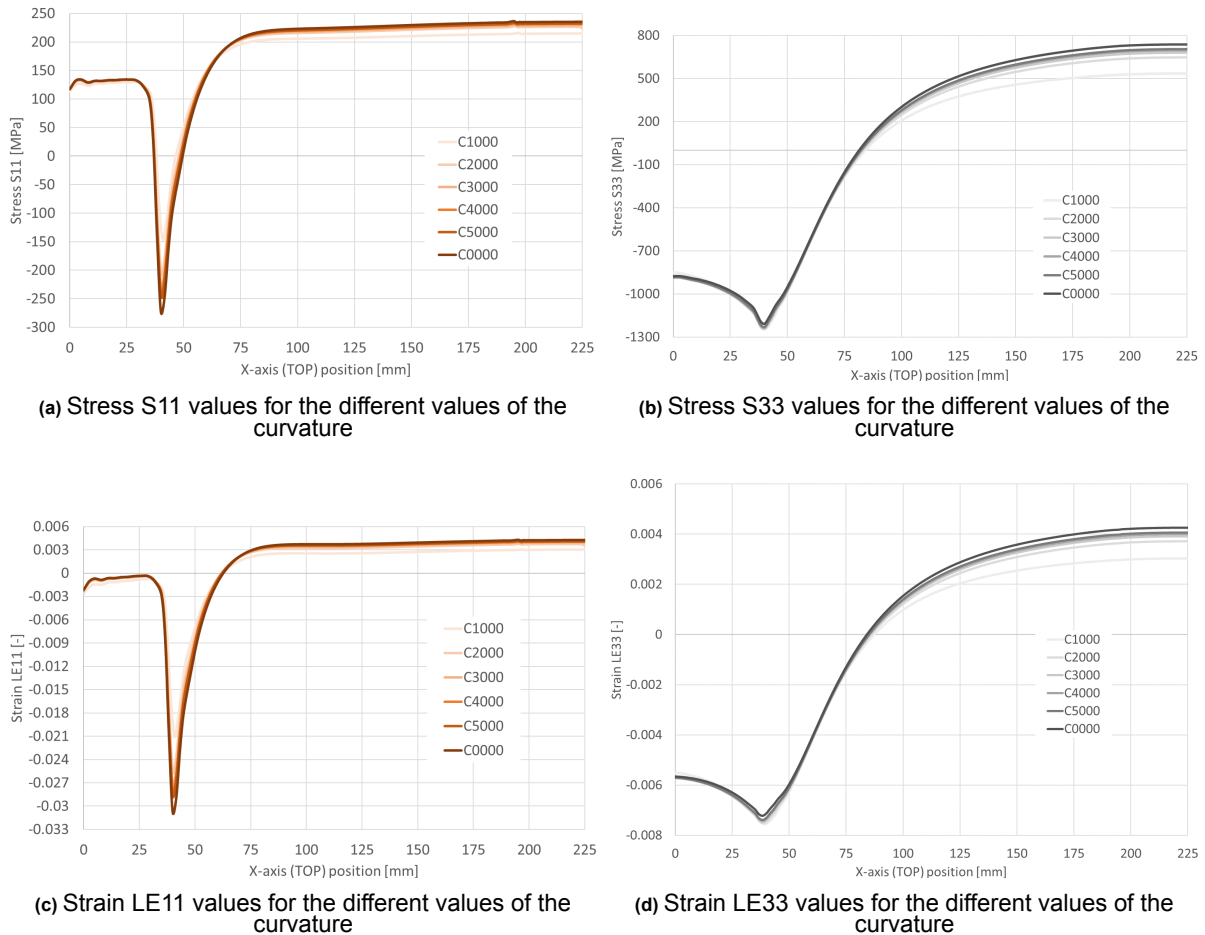


Figure 3.7: Vertical displacement of the specimen for the different values of the curvature.

#### X-path Top

To compare different options of curvature for the specimen, the stress and strain values are provided in the Figure 3.8. Firstly, the values along the X-axis, at the top of the laminate, are shown. Stress S11 in the Figure 3.8a, Stress S33 in the Figure 3.8b, Strain LE11 Figure 3.8c, and finally strain LE33 Figure 3.8d. The colours of the lines in the plot are sequenced according to the increasing curvature, where the flat specimen can be regarded as a specimen with infinite curvature.



**Figure 3.8:** Results for the curvature study. Values provided along the X-axis at the top of the specimen

### X-path Bottom

To give better insights into the specimen behaviour, the stress and strain values along the x-axis at the bottom of the specimen are provided Figure 3.9. The results for the Stress S11 in the Figure 3.9a, Stress S33 in the Figure 3.9b, Strain LE11 in the Figure 3.9c, Strain LE33 in the Figure 3.9d. The stresses at the bottom of the laminate are mostly positive as the specimen is in tension due to the bending motion. The difference across the different curvatures is primarily noticeable around the stress peak.

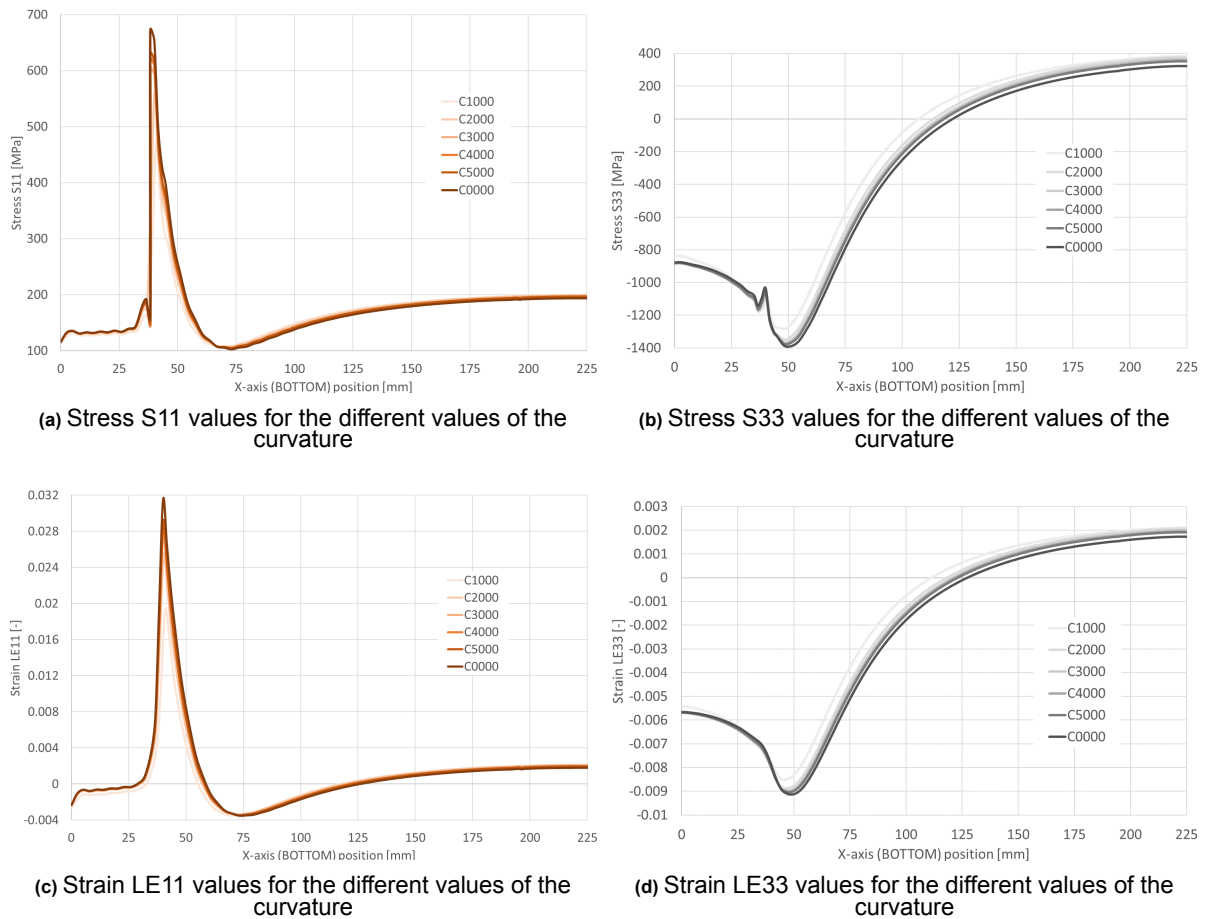


Figure 3.9: Results for the curvature study. Values provided along the X-axis at the bottom of the specimen

### Equal Bi-axial strain

Once the strain values were known for the different curvature values, the strain LE11/LE33 ratio was plotted. The results of this analysis can be seen for both the top and bottom path of the specimen.

#### X-path Top

Firstly, the values at the path on the top of the specimen are provided in the Figure 3.10. The assumed ratio for the equal bi-axial zone is highlighted in orange by the dotted line. The position of the X-axis is limited only to the relevant zone. In this case, the zone starts at 225 [mm], which is the specimen's centre and continues outward until the strain ratio crosses the 5% mark. The actual zone can be calculated by subtracting the crossing point from the specimen radius and multiplying it by 2, as the zone is symmetric due to the choice of the layout.

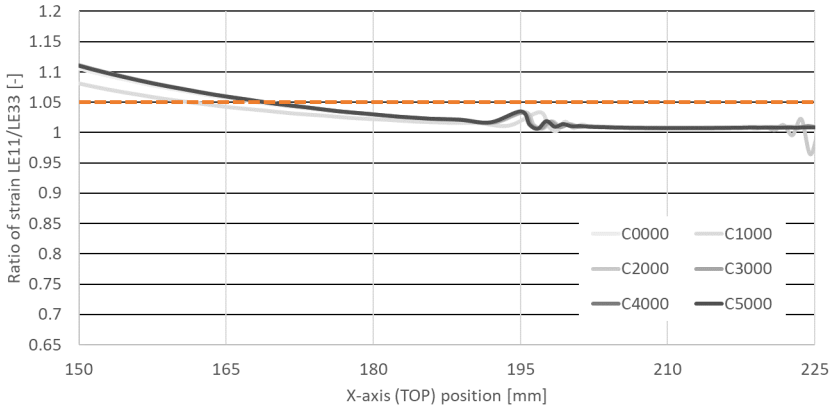


Figure 3.10: Results of the equal bi-axial zone analysis, concerning specimen curvature for the top of the specimen

**X-path bottom**

Then, also the values at the path on the bottom of the specimen are provided in the Figure 3.11. The assumed ratio for the equal bi-axial zone is highlighted in orange by the dotted line. The position of the X-axis is limited only to the relevant zone. In the case of the specimen with a curvature of 2000 [mm] also, the bottom limit should be taken into account, as the bi-axial zone is assumed to be present between the strain ratio of 95% and 105%.

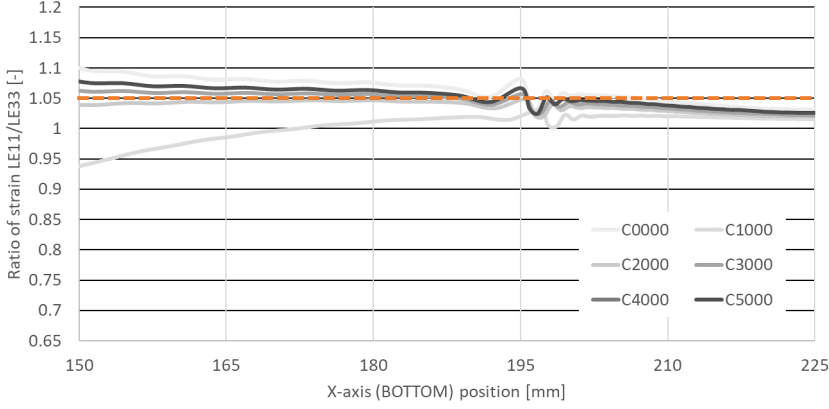


Figure 3.11: Results of the equal bi-axial zone analysis concerning specimen curvature for the bottom of the specimen

### 3.1.3. Effect of the Thickness

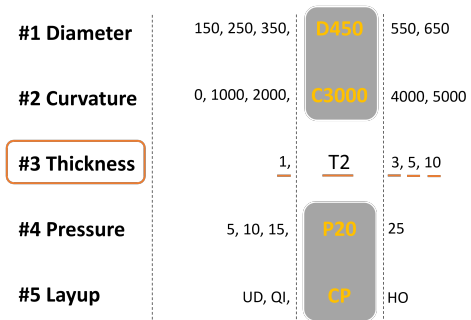


Figure 3.12: Variables analysed for the thickness effect study.

Now, the results for the different specimen thicknesses are provided. The tested variables can be seen in the Figure 3.12. Hence, five simulations were run for the specimen thicknesses of 1, 2, 3, 5, and 10 [mm]. The rest of the testing characteristics were kept the same as for the main configuration, shown in the grey block.

The results are provided along the path to compare the value difference for all the specimen thicknesses. Due to the choice of the layup, namely, the cross-ply used in this analysis, only the X-axis path is sufficient to provide the relevant data. However, to gain insight into the specimen's behaviour across the thickness, the results have been provided both for the top and

bottom path of the specimen.

Firstly, however, the vertical displacement's outcome of the thickness analysis is shown in the Figure 3.13. The reference line in this case is not shown as it is precisely the same as for the specimen with the curvature of 3000 [mm] from the previous study for all thickness values. The clamping zone ends in the exact location for all tested specimens at 35 [mm] into the laminate. The displacement is shown only in the absolute sense.

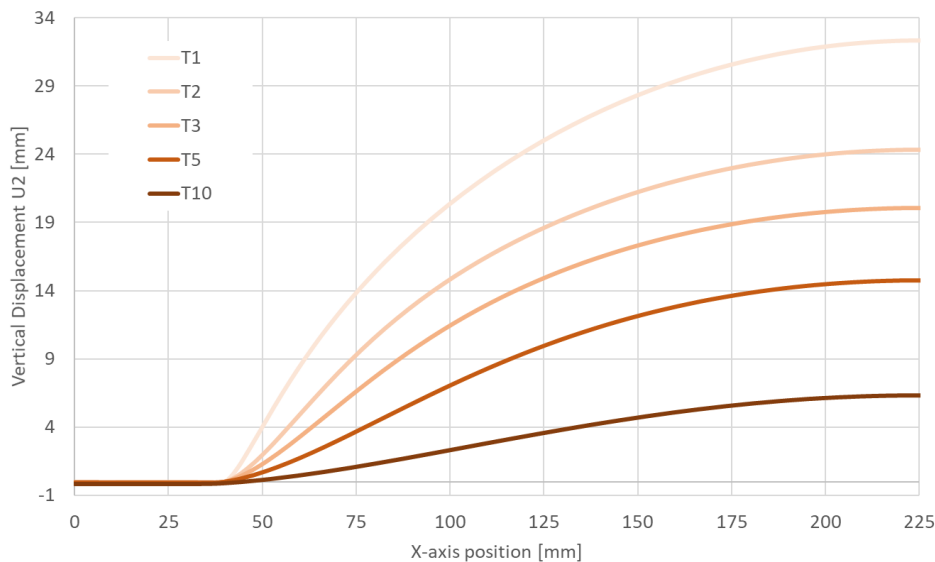
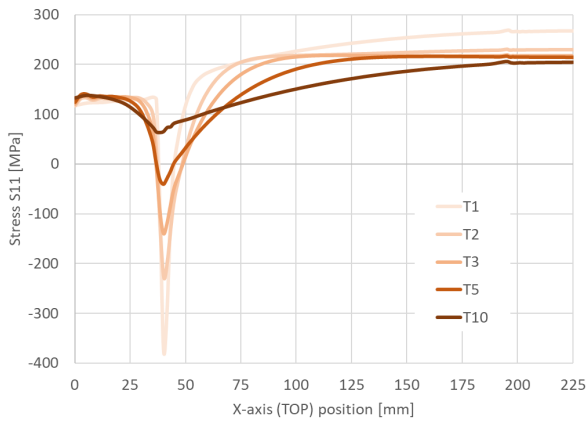


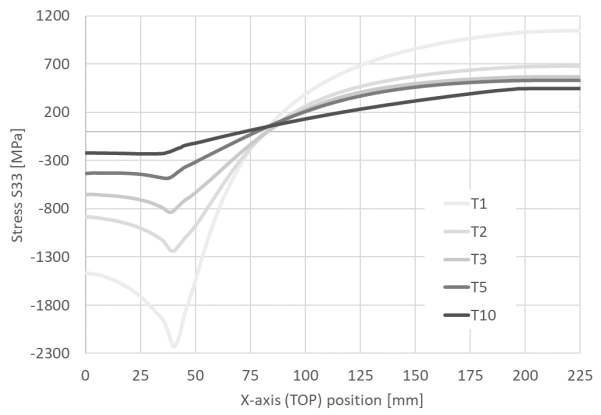
Figure 3.13: Vertical displacement of the specimen with different thicknesses

#### X-path Top

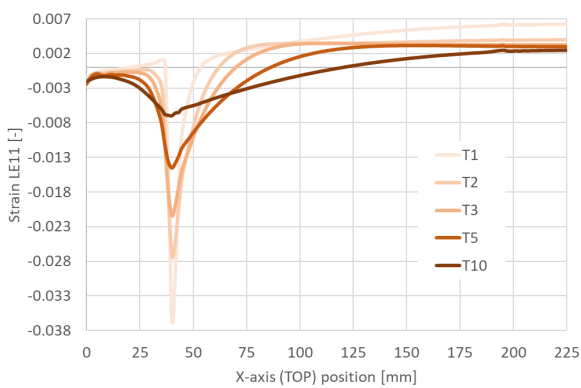
To compare different options of the specimen thickness, the stress and strain values are provided in the Figure 3.14. Firstly, the values along the X-axis, at the top of the laminate, are shown. Stress S11 in the Figure 3.14a, Stress S33 in the Figure 3.14b, Strain LE11 Figure 3.14c, and finally strain LE33 Figure 3.14d. The thinnest laminate, depicted with the brightest colour, is also the least stiff. Hence, it has the largest stresses and strains present caused by the pressure loading.



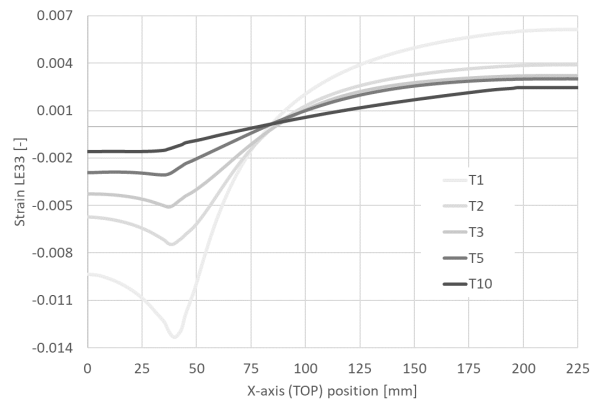
(a) Stress S11 values for the different values of the specimen's thickness



(b) Stress S33 values for the different values of the specimen's thickness



(c) Strain LE11 values for the different values of the specimen's thickness



(d) Strain LE33 values for the different values of the specimen's thickness

**Figure 3.14:** Results for the thickness study. Values provided along the X-axis at the top of the specimen

**X-path Bottom**

To give better insights into the specimen behaviour, the stress and strain values along the x-axis at the bottom of the specimen are provided Figure 3.15. The results for the Stress S11 in the Figure 3.15a, Stress S33 in the Figure 3.15b, Strain LE11 in the Figure 3.15c, Strain LE33 in the Figure 3.15d.

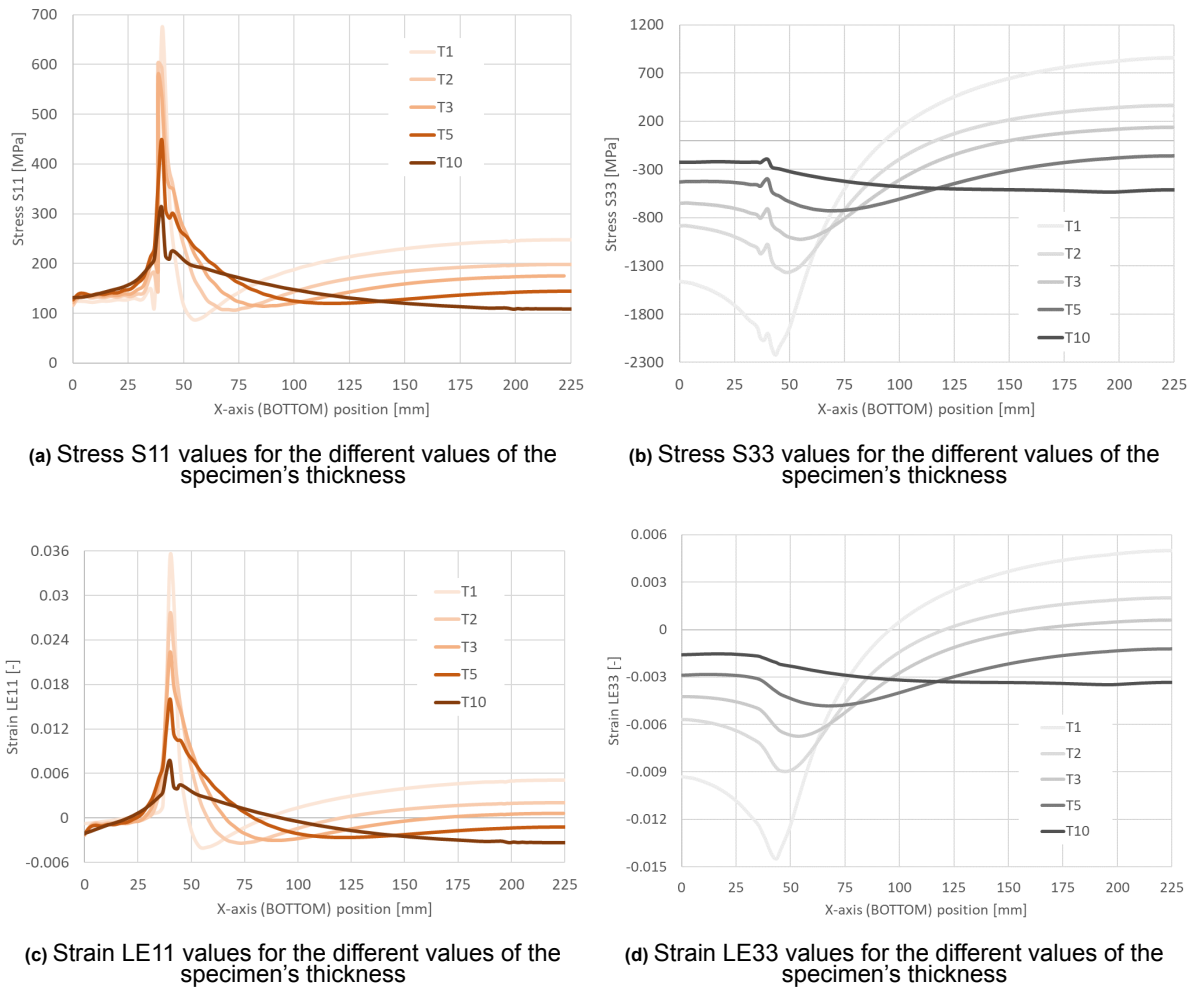


Figure 3.15: Results for the thickness study. Values provided along the X-axis at the bottom of the specimen

### Equal Bi-axial strain

Once the strain values were known for the different thickness values, the strain LE11/LE33 ratio was plotted. The results of this analysis can be seen for both the top and bottom path of the specimen.

#### X-path Top

Firstly, the values at the path on the top of the specimen are provided in the Figure 3.16. The assumed ratio for the equal bi-axial zone is highlighted in orange by the dotted line. In this case, both the upper and the lower limits of the assumed acceptable ratio are shown. The position of the X-axis is limited only to the relevant zone. Starting at the specimen's centre and continuing outwards till the crossing point of the specimen with the biggest equal bi-axial strain zone.

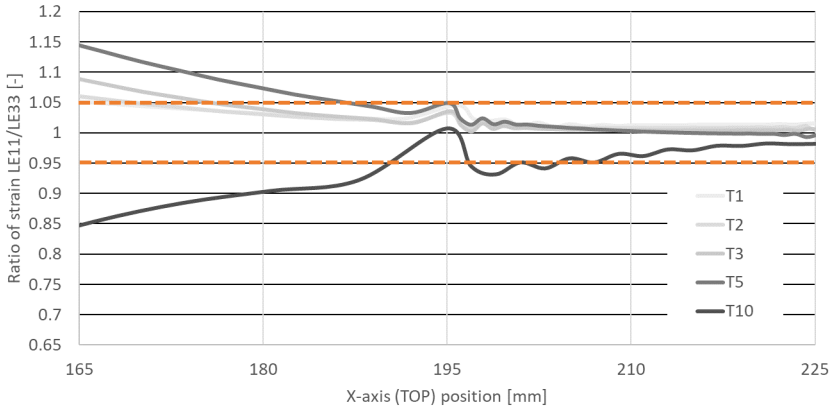


Figure 3.16: Equal bi-axial zone distribution at the top of the specimen

**X-path bottom**

Then, also the values at the path on the bottom of the specimen are provided in the Figure 3.17. The assumed ratio for the equal bi-axial zone is highlighted in orange by the dotted line. The position of the X-axis is limited only to the relevant zone.

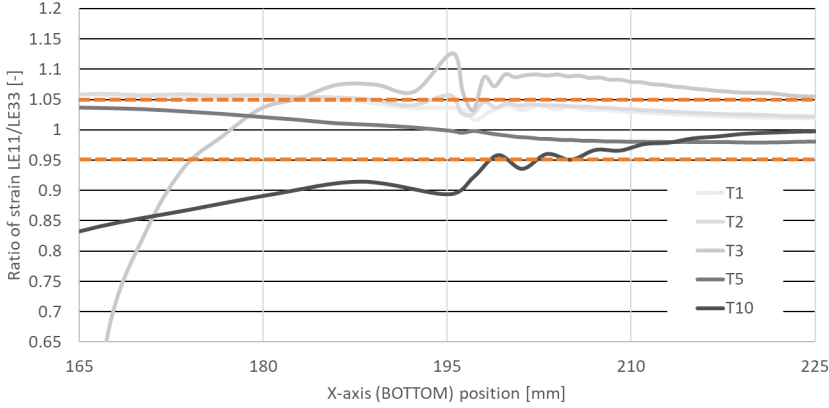


Figure 3.17: Equal bi-axial zone distribution at the bottom of the specimen

### 3.1.4. Effect of the Pressure

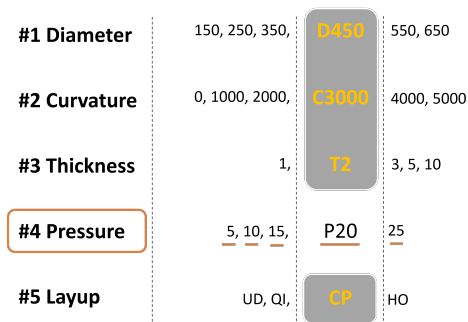


Figure 3.18: Variables analysed for the pressure effect study

The results for the different pressures are provided as a fourth simulation set. The tested variables can be seen in the Figure 3.18. Hence, five simulations were run for the following pressure values: 5, 10, 15, 20, and 25 [bar]. The rest of the testing characteristics were kept the same as for the main configuration, shown in the grey block.

The results are provided along the path to compare the difference in stress and strain due to the change in pressure. As the cross-ply laminate was used in this study, only the X-axis path is sufficient to provide the relevant data. However, to gain insight into the specimen's behaviour across the thickness, the results have

been provided both for the top and bottom path of the specimen.

Firstly, however, the outcome of the pressure analysis for the vertical displacement is shown in the Figure 3.19. Each analysis is presented as a grey line, while an orange dotted line shows the undeformed specimen used as a reference. Both the absolute and the relative displacement are visualised in this case. The absolute displacement can be calculated by subtracting the reference value from the total value.

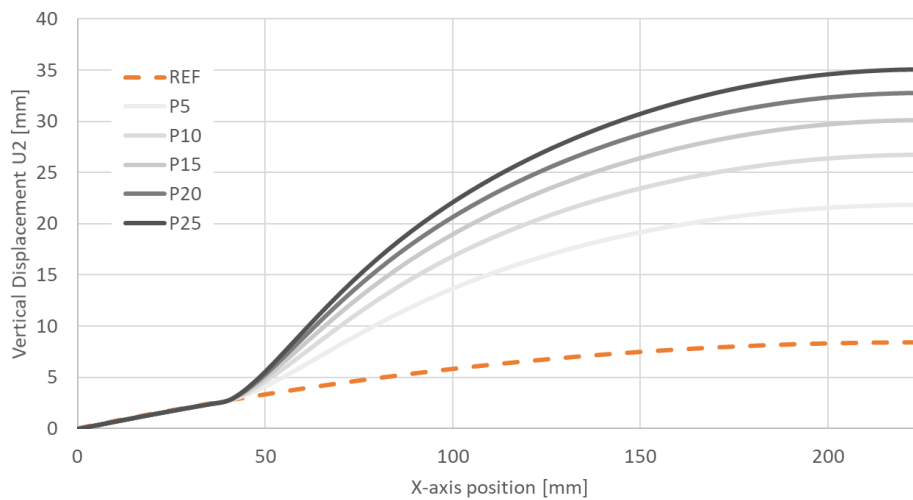
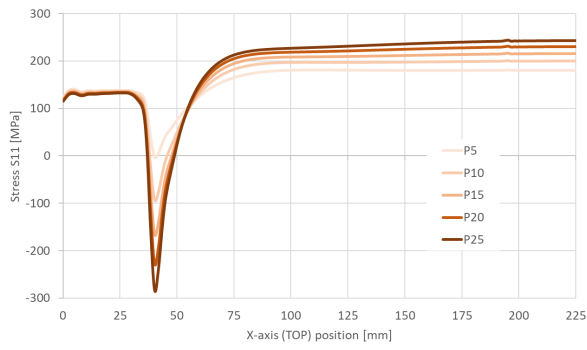


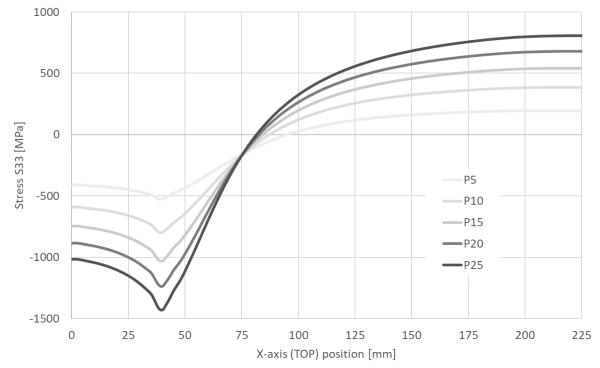
Figure 3.19: Vertical displacement of the specimen for the different values of the pressure

#### X-path top

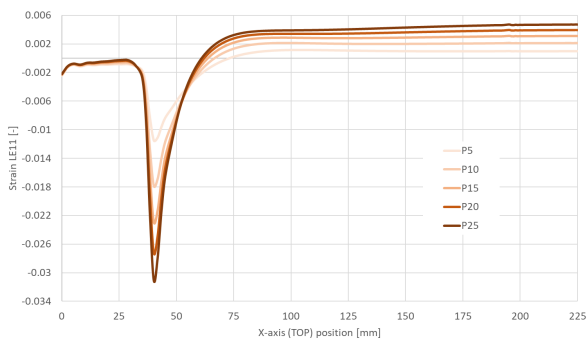
To compare different pressure values for the specimen testing, the stress and strain values are provided in the Figure 3.20. Firstly, the values along the X-axis, at the top of the laminate, are shown. Stress S11 in the Figure 3.20a, Stress S33 in the Figure 3.20b, Strain LE11 Figure 3.20c, and finally strain LE33 Figure 3.20d. The colours of the lines are getting darker as the pressure increases. The difference between the tested specimens can be seen almost across the entire laminate length, excluding the clamping zone.



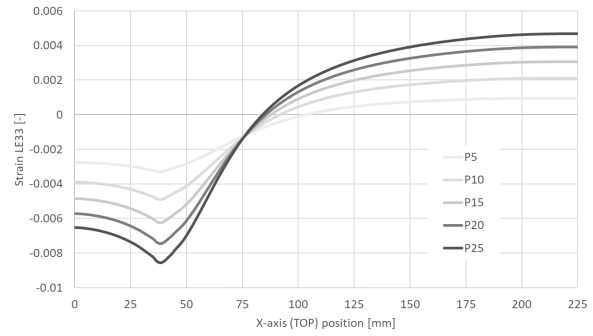
(a) Stress S11 values for the different values of the pressure



(b) Stress S33 values for the different values of the pressure



(c) Strain LE11 values for the different values of the pressure

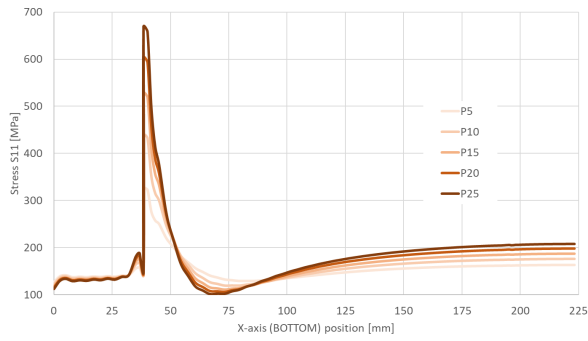


(d) Strain LE33 values for the different values of the pressure

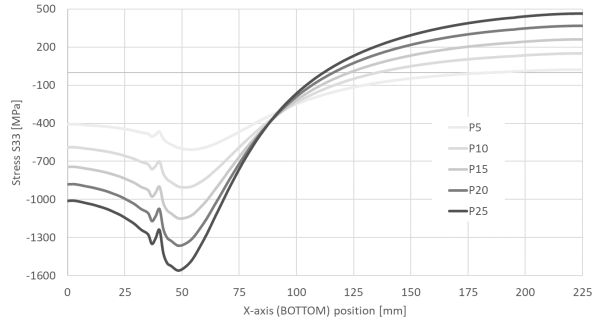
**Figure 3.20:** Results for the pressure study. Values provided along the X-axis at the top of the specimen

**X-path bottom**

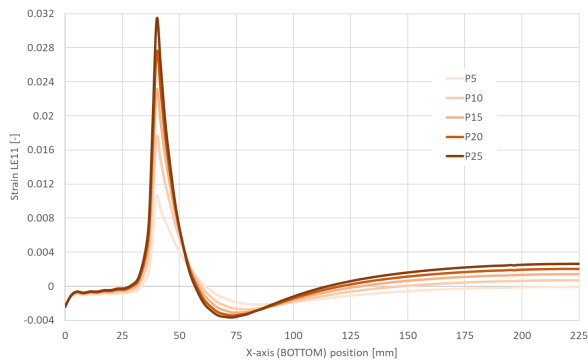
To give better insights into the specimen behaviour, the stress and strain values along the x-axis at the bottom of the specimen are provided Figure 3.21. The results for the Stress S11 in the Figure 3.21a, Stress S33 in the Figure 3.21b, Strain LE11 in the Figure 3.21c, Strain LE33 in the Figure 3.21d.



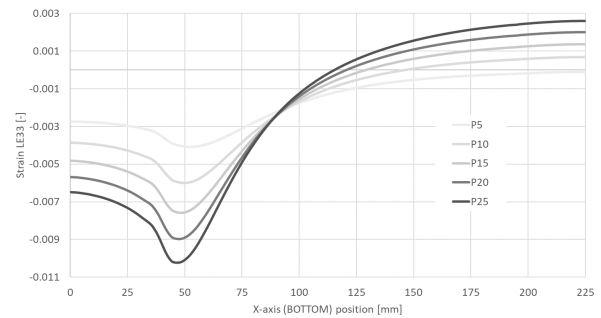
(a) Stress S11 values for the different values of the pressure



(b) Stress S33 values for the different values of the pressure



(c) Strain LE11 values for the different values of the pressure



(d) Strain LE33 values for the different values of the pressure

Figure 3.21: Results for the pressure study. Values provided along the X-axis at the bottom of the specimen

### Equal Bi-axial strain

Once the strain values were known for the different pressure values, the strain LE11/LE33 ratio was plotted. The results of this analysis can be seen for both the top and bottom path of the specimen.

#### X-path Top

Firstly, the values at the path on the top of the specimen are provided in the Figure 3.22. The assumed ratio for the equal bi-axial zone is highlighted in orange by the dotted line. The position of the X-axis is limited only to the relevant zone.

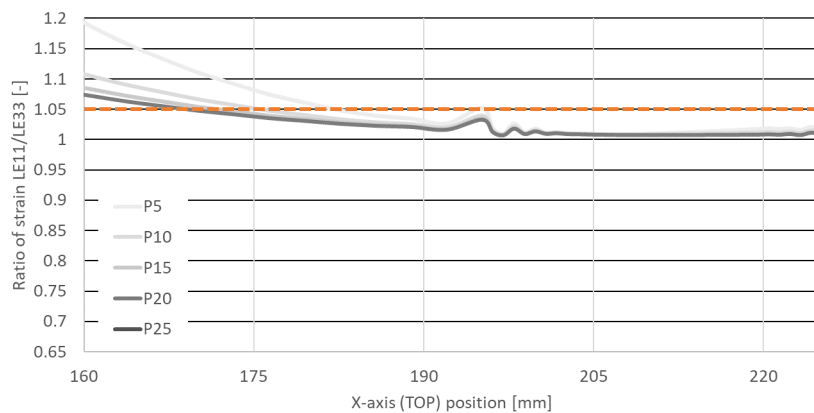
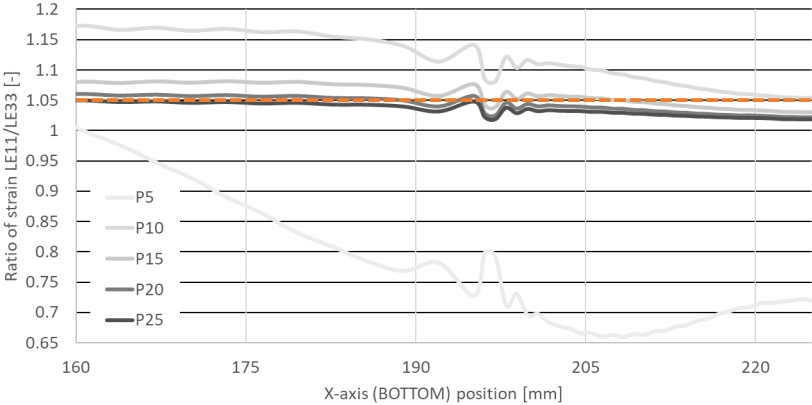


Figure 3.22: Equal bi-axial zone distribution at the top of the specimen

**X-path bottom**

Then, also the values at the path on the bottom of the specimen are provided in the Figure 3.23. The assumed ratio for the equal bi-axial zone is highlighted in orange by the dotted line. The position of the X-axis is limited only to the relevant zone. The zone starts in the middle of the specimen and continues outwards until the specimen with the most extended bi-axial strain zone crosses the assumed limit; in this case, it is laminate with the 25 [bar] pressure. The specimen with 5 [bar] pressure loading doesn't even develop the right strain ratio, as its curve starts at the ratio of 0.72.



**Figure 3.23:** Equal bi-axial zone distribution at the bottom of the specimen

### 3.1.5. Effect of the Layup

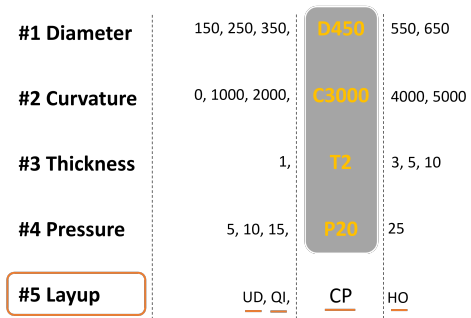


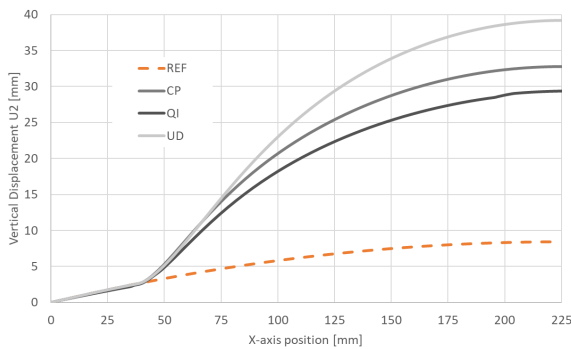
Figure 3.24: Variables analysed for the layup effect study

The results for the different layups are provided as a final analysis of the parametric study. The tested variables can be seen in the Figure 3.24. Hence, only three simulations were run for the following layup configurations: Quasi-isotropic (QI), Cross-ply (CP) and Uni-directional (UD). The rest of the testing characteristics were kept the same as for the main configuration, shown in the grey block.

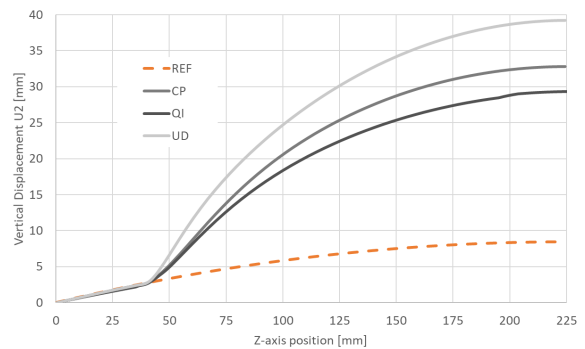
The results are provided along the path to compare the difference in stress and strain due to the change in pressure. In the case of this study, the values are provided for both paths in the x-coordinate and z-coordinate. Furthermore, to gain insight into the specimen's behaviour

across the thickness, the results for the x-path have been provided both for the top and bottom sides of the specimen.

Firstly, however, the outcome of the layup analysis for the vertical displacement is shown in the Figure 3.25a for x-path and in the Figure 3.25b. Each analysis is presented as a grey line, while an orange dotted line shows the undeformed specimen used as a reference. The results are provided in both coordinate paths to show the displacement asymmetry for the UD laminate.



(a) Vertical displacement of the specimen for the different layup options for the x-path



(b) Vertical displacement of the specimen for the different layup options for the z-path

Figure 3.25: Vertical displacement of the specimen for the different layup options

#### Z-path top

To compare different pressure values for the specimen testing, the stress and strain values are provided in the Figure 3.26. Firstly, the values along the Z-axis at the top of the laminate are shown. Stress S11 in the Figure 3.26a, Stress S33 in the Figure 3.26b, Strain LE11 Figure 3.26c, and finally strain LE33 Figure 3.26d. The colour of the lines changes with the change in the overall stiffness of each layup.

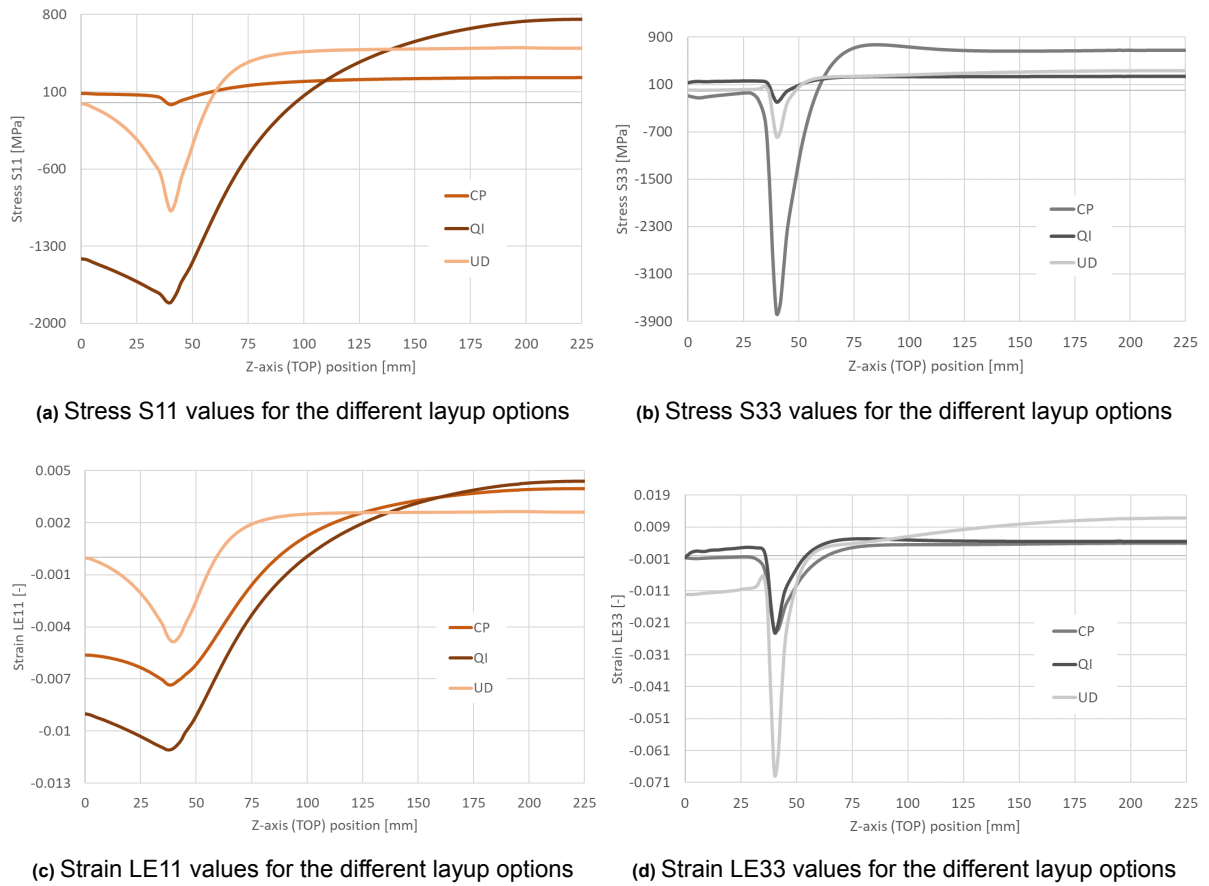


Figure 3.26: Results of the layup study. Values provided along the Z-axis at the top of the specimen

**X-path top**

Then, the stress and strain values are provided along the X-axis at the top of the laminate in the Figure 3.27. Stress S11 in the Figure 3.27a, Stress S33 in the Figure 3.27b, Strain LE11 Figure 3.27c, and finally strain LE33 Figure 3.27d.

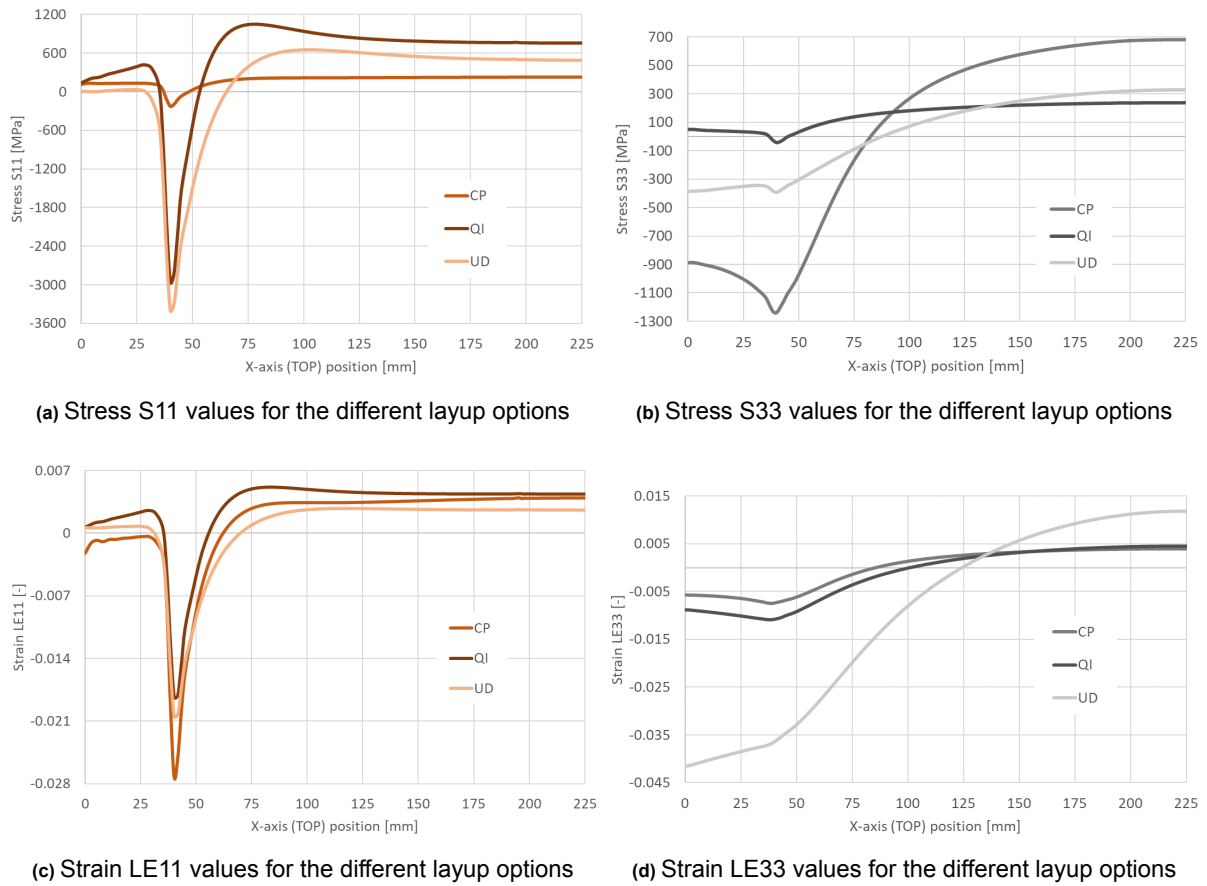


Figure 3.27: Results of the layup study. Values provided along the X-axis at the top of the specimen

**X-path bottom**

To give better insights into the specimen behaviour, the stress and strain values along the x-axis at the bottom of the specimen are provided Figure 3.28. The results for the Stress S11 in the Figure 3.28a, Stress S33 in the Figure 3.28b, Strain LE11 in the Figure 3.28c, Strain LE33 in the Figure 3.28d.

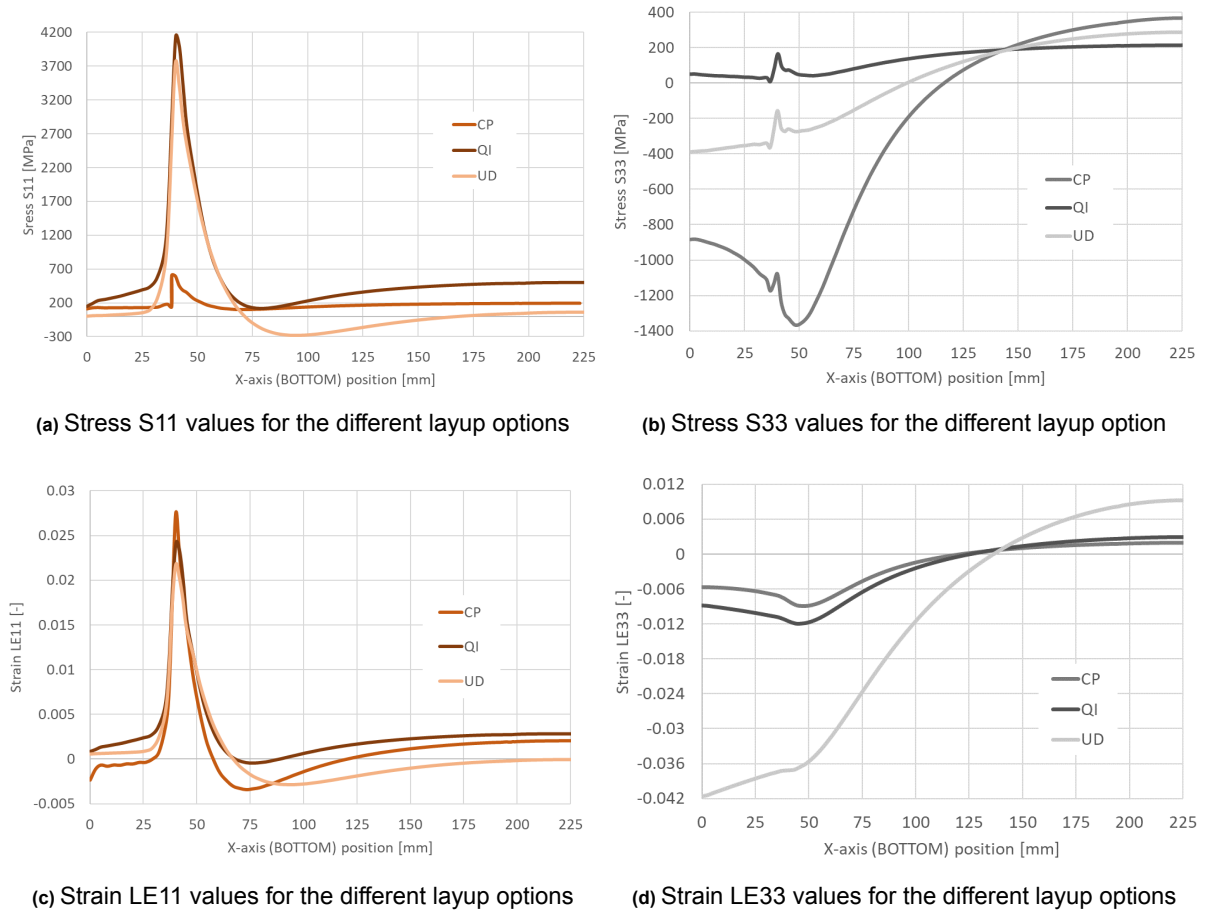


Figure 3.28: Results of the layup study. Values provided along the X-axis at the bottom of the specimen

### Equal Bi-axial strain

Once the strain values were known for the different layup options, the strain LE11/LE33 ratio was plotted. The results of this analysis can be seen for both the top and bottom path of the specimen. The unidirectional laminate wasn't included in the presented graphs as it didn't produce an equal bi-axial zone.

#### X-path Top

Firstly, the values at the path on the top of the specimen are provided in the Figure 3.29. The assumed ratio for the equal bi-axial zone is highlighted in orange by the dotted line. The position of the X-axis is limited only to the relevant zone. The zone starts at the 225 [mm] mark, which is the specimen's centre, and continues until the last curve crosses the orange highlighted line. The UD laminate results are not shown in this case as this layup option didn't develop the equal bi-axial strain.

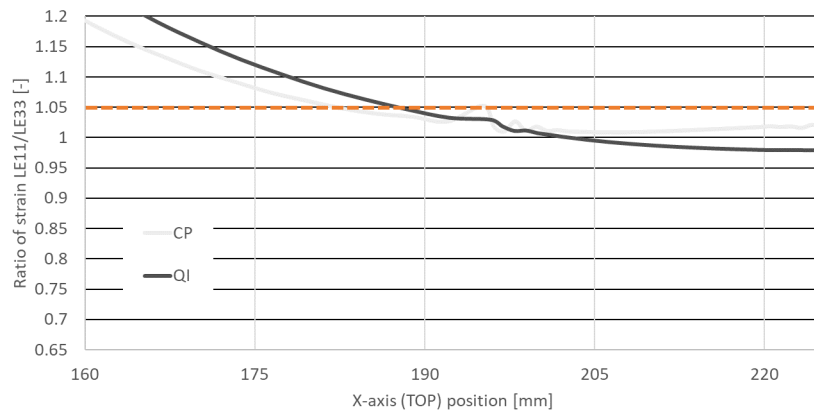


**Figure 3.29:** Equal bi-axial zone distribution at the top of the specimen

### X-path bottom

Then, also the values at the path on the bottom of the specimen are provided in the Figure 3.30. The assumed ratio for the equal bi-axial zone is highlighted in orange by the dotted line. The position of the X-axis is limited only to the relevant zone.

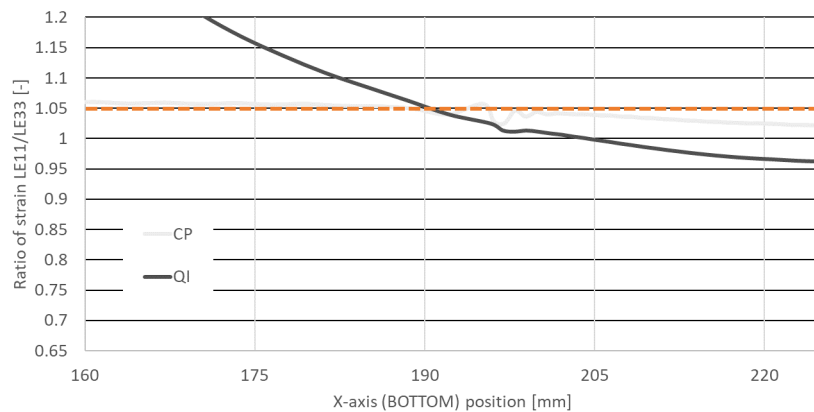


**Figure 3.30:** Equal bi-axial zone distribution at the bottom of the specimen

## 3.2. Damage Analysis results

To see if the damage is present in the specimen, the same specimen that was used for the parametric study was also tested for damage using the LARC05 damage criterion. The results for this study are present in the Figure 3.32, where the first appearance of each damage criterion is visualised with the stars, following the legend presented in the Figure 3.31. The results are plotted for the element near the specimen's centre (Figure 3.32a) and at the critical region near the clamping (Figure 3.32b). The values of stress and strain are provided for both locations. The steps used in the simulation are separated via a grey dotted line as seen in the Figure 3.32. Four steps are present for the first analysis without the reinforcement, but only three steps are shown in the case of the further analysis. This is the limitation of the ABAQUS software, where the tie constraint couldn't be deactivated for the initial cooling step. Hence, only the relevant steps where the reinforcement would be present are shown. Fortunately, the stress and strain present in the laminate after the initial cooling are minimal.

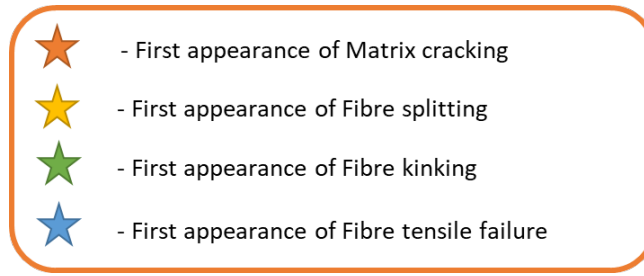
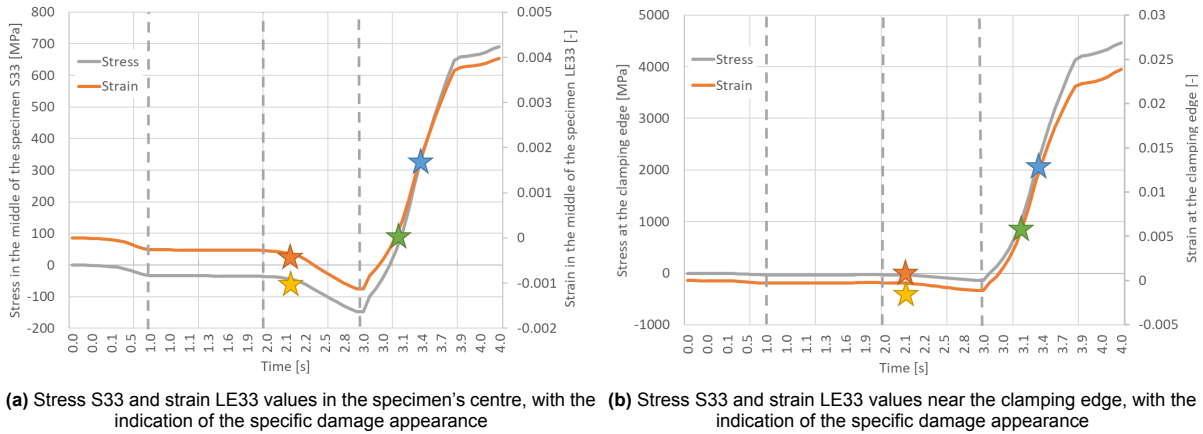


Figure 3.31: Legend for the damage analysis graphs



(a) Stress S33 and strain LE33 values in the specimen's centre, with the indication of the specific damage appearance (b) Stress S33 and strain LE33 values near the clamping edge, with the indication of the specific damage appearance

Figure 3.32: Stress and strain values for the specimen with the indication of the first damage appearance

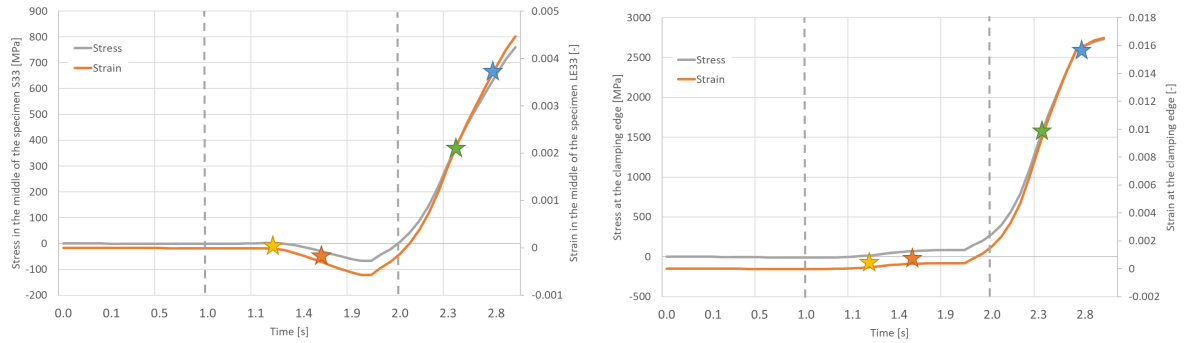
The specimen's status just before the first damage appearance for different damage criteria can be seen in the Table 3.2. The provided visualisation is the ABAQUS representation of the damage for all the elements present in the model. The damage is present when the value reaches 1. The legend is also provided in the table for ease of reading. The matrix cracking and fibre splitting are presented from the top side of the specimen, while the fibre kinking and fibre tensile failure are provided from the bottom. The specimen status after the first damage initiation is not provided as the LARC05 damage criterion can't provide damage evolution. Hence, the results at later stages of the analysis are not relevant.

Matrix cracking	Fiber split	Fiber kinking	Fiber tensile
LARCMCRTC Envelope (max) (Avg: 75%) +1.000e+00 +9.602e-01 +9.205e-01 +8.807e-01 +8.410e-01 +8.012e-01 +7.615e-01 +7.217e-01 +6.820e-01 +6.422e-01 +6.025e-01 +5.627e-01 +5.229e-01	LARCFSCRT Envelope (max) (Avg: 75%) +1.000e+00 +9.500e-01 +9.011e-01 +8.501e-01 +8.001e-01 +7.501e-01 +7.002e-01 +6.502e-01 +6.002e-01 +5.503e-01 +5.003e-01 +4.503e-01 +4.004e-01	LARCFKCRT Envelope (max) (Avg: 75%) +1.000e+00 +9.167e-01 +8.333e-01 +7.500e-01 +6.667e-01 +5.833e-01 +5.000e-01 +4.167e-01 +3.333e-01 +2.500e-01 +1.667e-01 +8.333e-02 +0.000e+00	LARCFTCRT Envelope (max) (Avg: 75%) +1.000e+00 +9.167e-01 +8.333e-01 +7.500e-01 +6.667e-01 +5.833e-01 +5.000e-01 +4.167e-01 +3.333e-01 +2.500e-01 +1.667e-01 +8.333e-02 +0.000e+00

Table 3.2: Specimen status just before or at the first damage appearance for each of the initial damage criterion

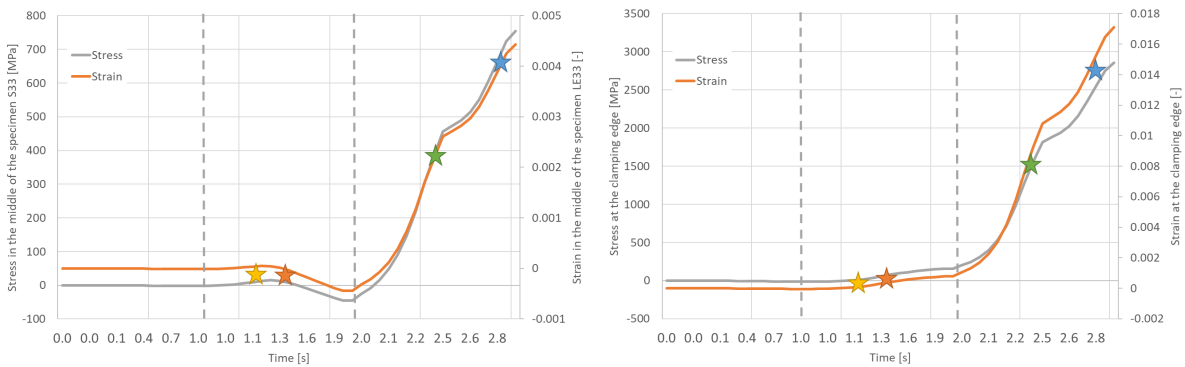
### 3.2.1. Damage results for the different reinforcement thickness

Similarly, the damage analysis results for the considered reinforcement are also provided. Firstly, the influence of the reinforcement thickness on the damage is shown. For each of the analysed thicknesses, the values of stress and strain are plotted for the element in the specimen's centre and near the clamping region. In the Figure 3.33, the results for the 1 [mm] reinforcement thickness are visualised, and in the Figure 3.34 for the 2 [mm] and finally, in the Figure 3.35 for the 4 [mm]. The first damage appearance for each criterion is indicated using stars as introduced in the Figure 3.31.



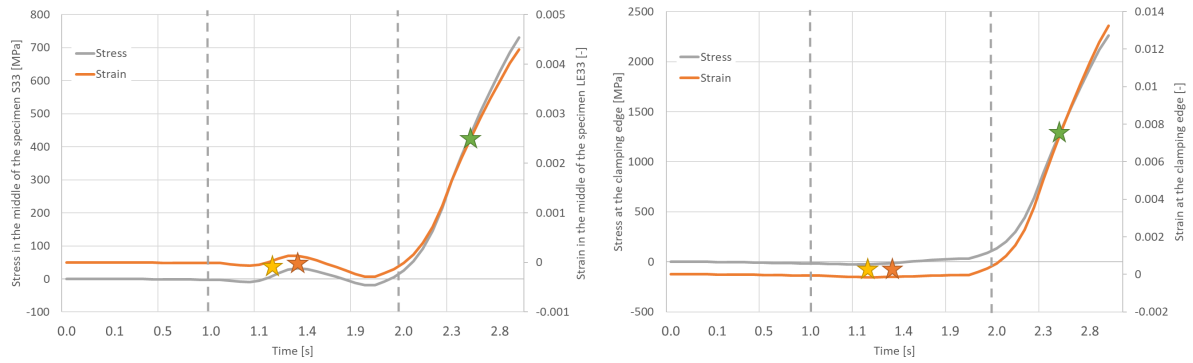
(a) Stress S33 and strain LE33 values in the specimen's centre, with the indication of the specific damage appearance (b) Stress S33 and strain LE33 values near the clamping edge, with the indication of the specific damage appearance

**Figure 3.33:** Stress and strain values for the specimen with the 1 mm thick reinforcement with the indication of the first damage appearance



(a) Stress S33 and strain LE33 values in the specimen's centre, with the indication of the specific damage appearance (b) Stress S33 and strain LE33 values near the clamping edge, with the indication of the specific damage appearance

**Figure 3.34:** Stress and strain values for the specimen with the 2 mm thick reinforcement with the indication of the first damage appearance



(a) Stress S33 and strain LE33 values in the specimen's centre, with the indication of the specific damage appearance (b) Stress S33 and strain LE33 values near the clamping edge, with the indication of the specific damage appearance

**Figure 3.35:** Stress and strain values for the specimen with the 4 mm thick reinforcement with the indication of the first damage appearance

Also, in the case of the different reinforcement thicknesses, the specimen's status just before the first damage appearance for different damage criteria can be seen in the Table 3.3 for all reinforcement options tested in this simulation set. The provided visualisation is the ABAQUS representation of the damage for all the elements present in the model. The damage is present when the value reaches 1. The legend is also provided in the table for ease of reading. The matrix cracking and fibre splitting are presented from the top side of the specimen, while the fibre kinking and fibre tensile failure are provided from the bottom. The specimen status after the first damage initiation is not provided as the LARC05 damage criterion can't provide damage evolution. Hence, the results at later stages are not relevant.

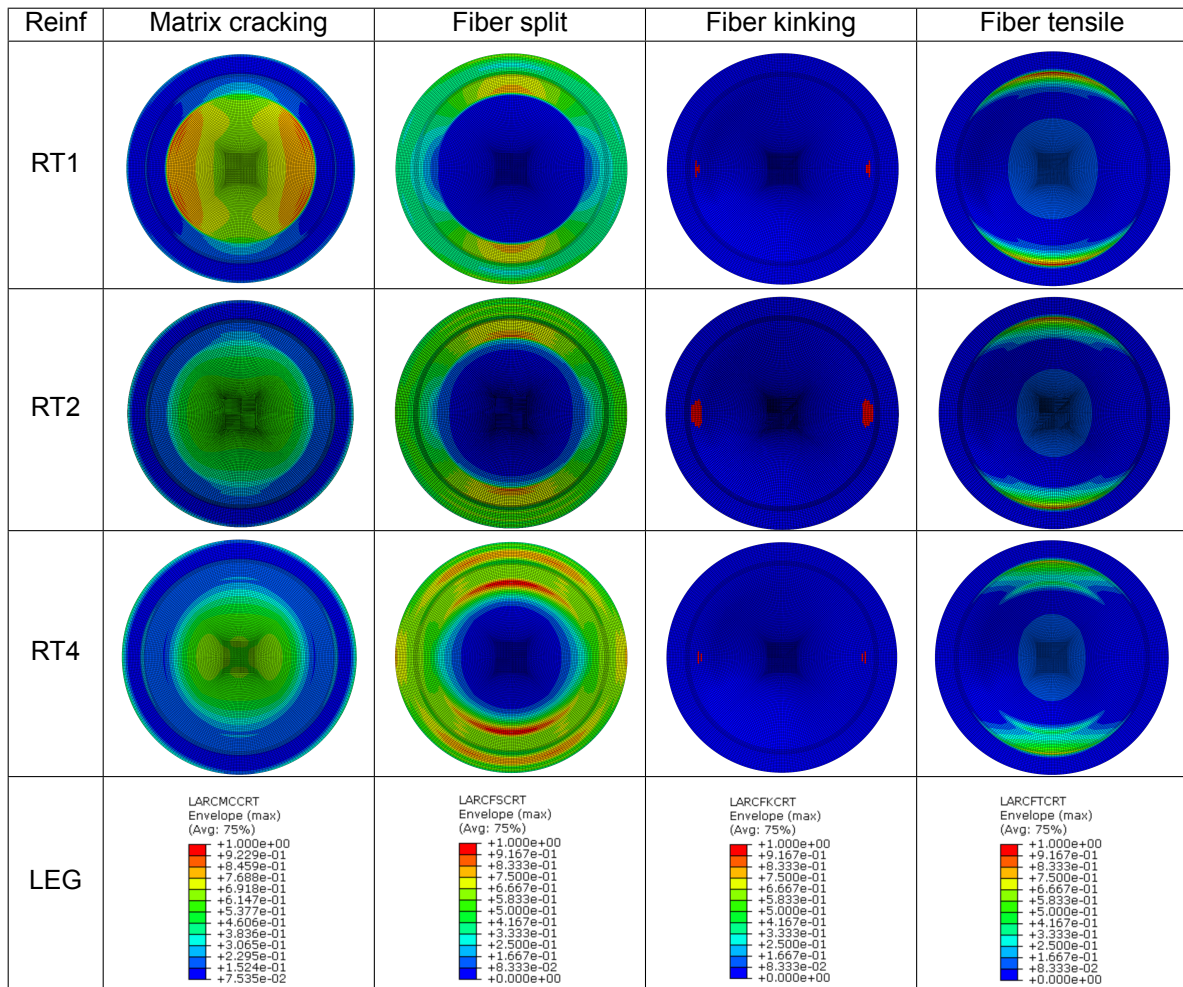
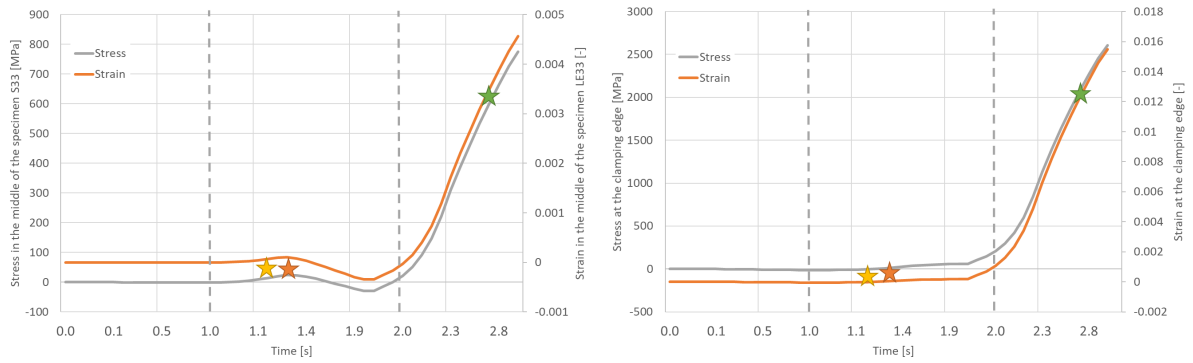


**Table 3.3:** Specimen status just before or at the first damage appearance for each of the initial damage criterion and for all tested reinforcement's thicknesses

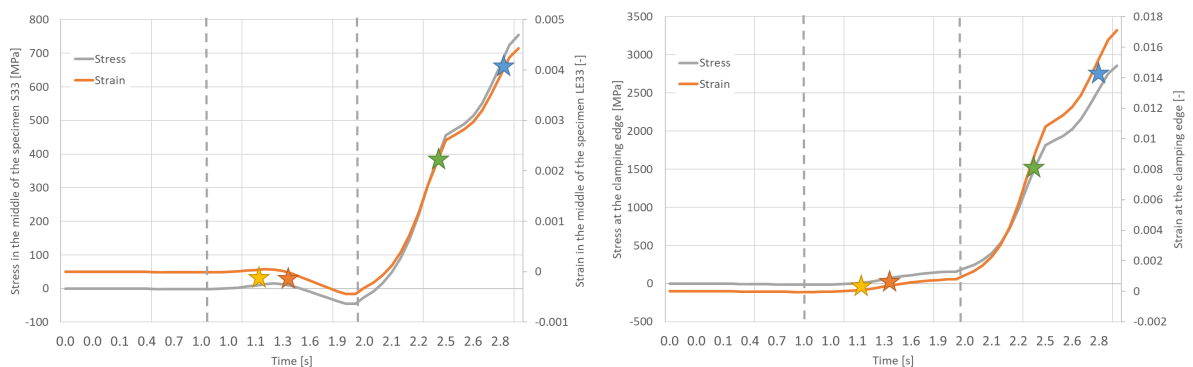
### 3.2.2. Damage results for the different reinforcement material

Different reinforcement materials have also been tested, and the results of their damage analyses are also provided. For each different reinforcement material analysed, the values of stress and strain are plotted for the element in the specimen's centre and near the clamping region. In the Figure 3.36, the results for the steel reinforcement are visualised, and in the Figure 3.37 for the aluminium reinforcement and finally, in the Figure 3.38 for the composite reinforcement. The first damage appearance for each criterion is indicated using stars as introduced in the Figure 3.31.



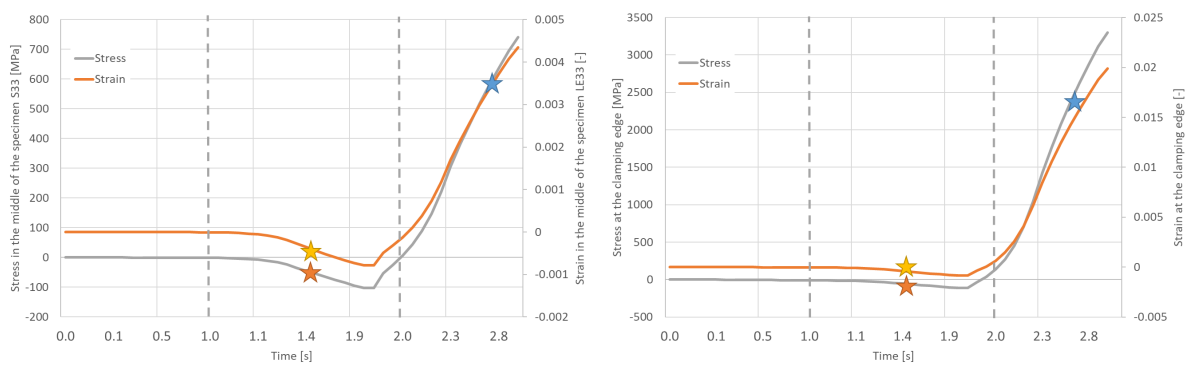
(a) Stress S33 and strain LE33 values in the specimen's centre, with the indication of the specific damage appearance (b) Stress S33 and strain LE33 values near the clamping edge, with the indication of the specific damage appearance

**Figure 3.36:** Stress and strain values for the specimen with the steel reinforcement with the indication of the first damage appearance



(a) Stress S33 and strain LE33 values in the specimen's centre, with the indication of the specific damage appearance (b) Stress S33 and strain LE33 values near the clamping edge, with the indication of the specific damage appearance

**Figure 3.37:** Stress and strain values for the specimen with the aluminium reinforcement with the indication of the first damage appearance

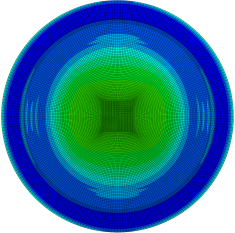
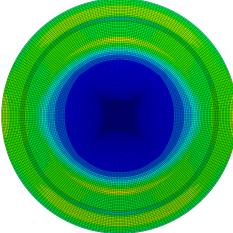
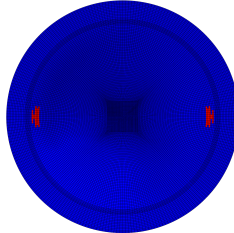
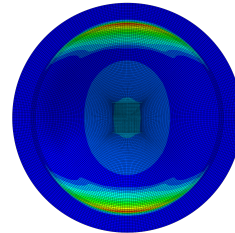
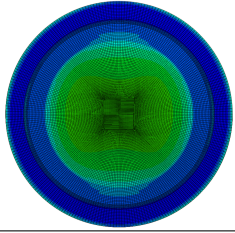
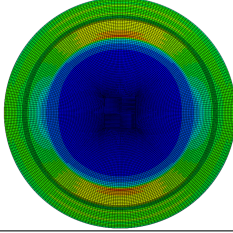
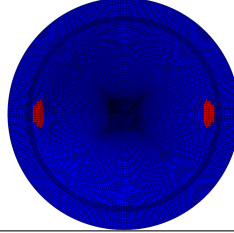
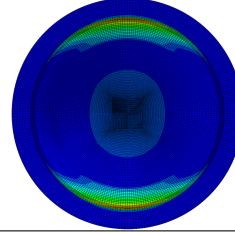
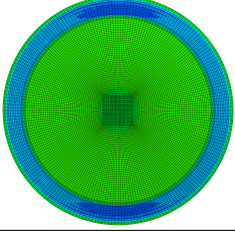
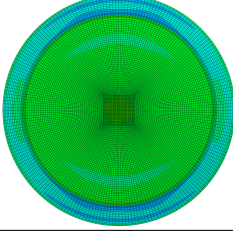
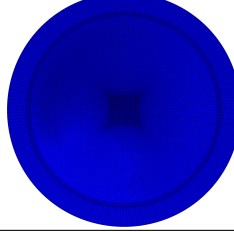
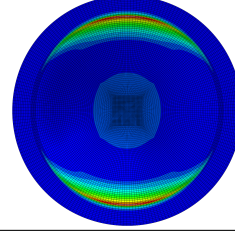


(a) Stress S33 and strain LE33 values in the specimen's centre, with the indication of the specific damage appearance (b) Stress S33 and strain LE33 values near the clamping edge, with the indication of the specific damage appearance

**Figure 3.38:** Stress and strain values for the specimen with the CFRP reinforcement with the indication of the first damage appearance

Also, in the case of the different reinforcement materials, the specimen's status just before the first damage appearance for different damage criteria can be seen in the Table 3.4 for all reinforcement options tested in this simulation set. The provided visualisation is the ABAQUS representation of the damage for all the elements present in the model. The damage is present when the value reaches 1. The legend is also provided in the table for ease of reading. The matrix cracking and fibre splitting are

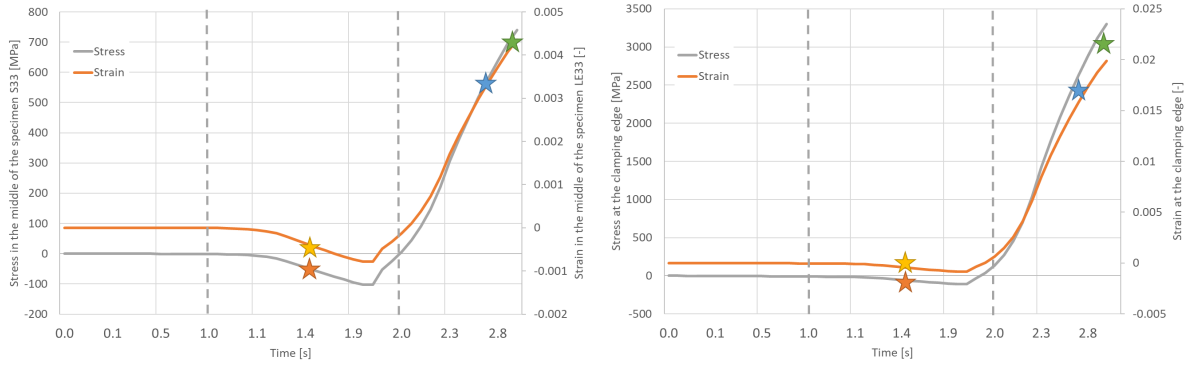
presented from the top side of the specimen, while the fibre kinking and fibre tensile failure are provided from the bottom. The specimen status after the first damage initiation is not provided as the LARC05 damage criterion can't provide damage evolution. Hence, the results at later stages are not relevant.

Reinf	Matrix cracking	Fiber split	Fiber kinking	Fiber tensile
Steel				
Alu				
CFRP				
LEG	<p>LARCMCRTC Envelope (max) (Avg: 75%)</p> <ul style="list-style-type: none"> <li>+1.000e+00</li> <li>+9.229e-01</li> <li>+8.459e-01</li> <li>+7.688e-01</li> <li>+6.918e-01</li> <li>+6.147e-01</li> <li>+5.377e-01</li> <li>+4.606e-01</li> <li>+3.836e-01</li> <li>+3.065e-01</li> <li>+2.295e-01</li> <li>+1.524e-01</li> <li>+7.535e-02</li> </ul>	<p>LARCFSCRT Envelope (max) (Avg: 75%)</p> <ul style="list-style-type: none"> <li>+1.000e+00</li> <li>+9.167e-01</li> <li>+8.333e-01</li> <li>+7.500e-01</li> <li>+6.667e-01</li> <li>+5.833e-01</li> <li>+5.000e-01</li> <li>+4.167e-01</li> <li>+3.333e-01</li> <li>+2.500e-01</li> <li>+1.667e-01</li> <li>+8.333e-02</li> <li>+0.000e+00</li> </ul>	<p>LARCFKRTC Envelope (max) (Avg: 75%)</p> <ul style="list-style-type: none"> <li>+1.000e+00</li> <li>+9.167e-01</li> <li>+8.333e-01</li> <li>+7.500e-01</li> <li>+6.667e-01</li> <li>+5.833e-01</li> <li>+5.000e-01</li> <li>+4.167e-01</li> <li>+3.333e-01</li> <li>+2.500e-01</li> <li>+1.667e-01</li> <li>+8.333e-02</li> <li>+0.000e+00</li> </ul>	<p>LARCFTRTC Envelope (max) (Avg: 75%)</p> <ul style="list-style-type: none"> <li>+1.000e+00</li> <li>+9.167e-01</li> <li>+8.333e-01</li> <li>+7.500e-01</li> <li>+6.667e-01</li> <li>+5.833e-01</li> <li>+5.000e-01</li> <li>+4.167e-01</li> <li>+3.333e-01</li> <li>+2.500e-01</li> <li>+1.667e-01</li> <li>+8.333e-02</li> <li>+0.000e+00</li> </ul>

**Table 3.4:** Specimen status just before or at the first damage appearance for each of the initial damage criterion and for all tested reinforcement's materials

**Composite reinforcement orientation**

One extra analysis was performed to provide additional detail for the composite reinforcement, where the plies were positioned at a 45-degree angle compared to the previous study. The values of stress and strain for this specific case are plotted for the element in the specimen's centre and near the clamping region as shown in the Figure 3.39. The specimen status just before the damage ignition for all considered criteria is also presented in the Table 3.5.



(a) Stress S33 and strain LE33 values in the specimen's centre, with the indication of the specific damage appearance (b) Stress S33 and strain LE33 values near the clamping edge, with the indication of the specific damage appearance

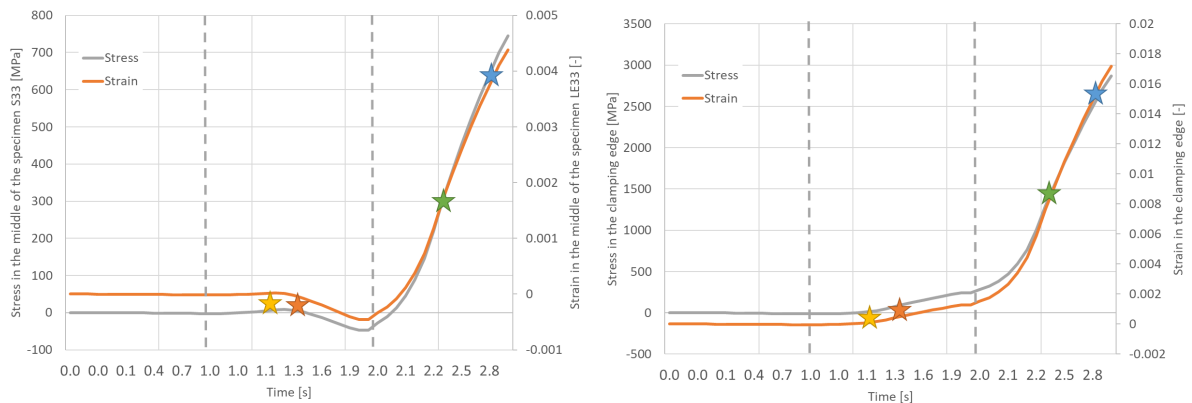
**Figure 3.39:** Stress and strain values for the specimen with the CFRP reinforcement at the 45-degree angle with the indication of the first damage appearance

Reinf	Matrix cracking	Fiber split	Fiber kinking	Fiber tensile
CFRP 45				

**Table 3.5:** Specimen status just before or at the first damage appearance for each of the initial damage criterion for the composite reinforcement with the 45-degree position angle

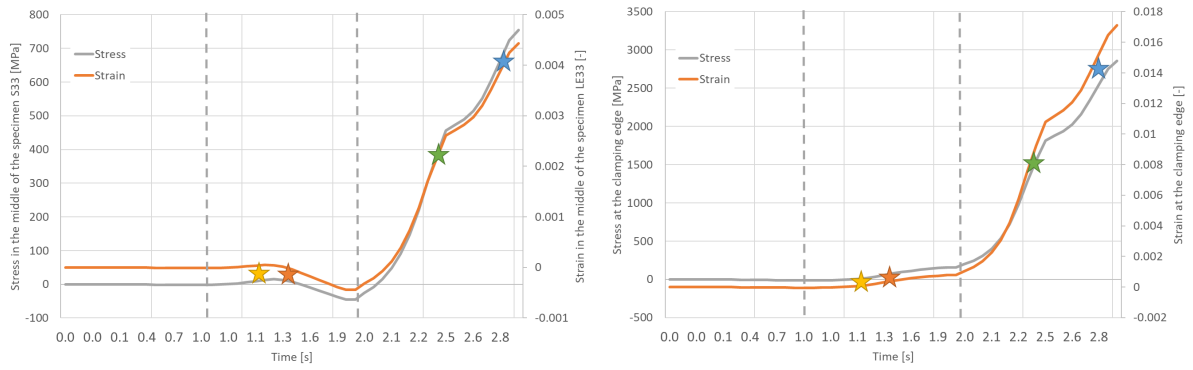
### 3.2.3. Damage results for the different reinforcement width

Different reinforcement widths have also been tested, and the results of their damage analyses are also provided. For each different reinforcement width analysed, the values of stress and strain are plotted for the element in the specimen's centre and near the clamping region. In the Figure 3.40, the results for the reinforcement width of 60 [mm] are visualised, and in the Figure 3.41 for the reinforcement width of 80 [mm] and finally, in the Figure 3.42 for the reinforcement width of 100 [mm]. The first damage appearance for each criterion is indicated using stars as introduced in the Figure 3.31.



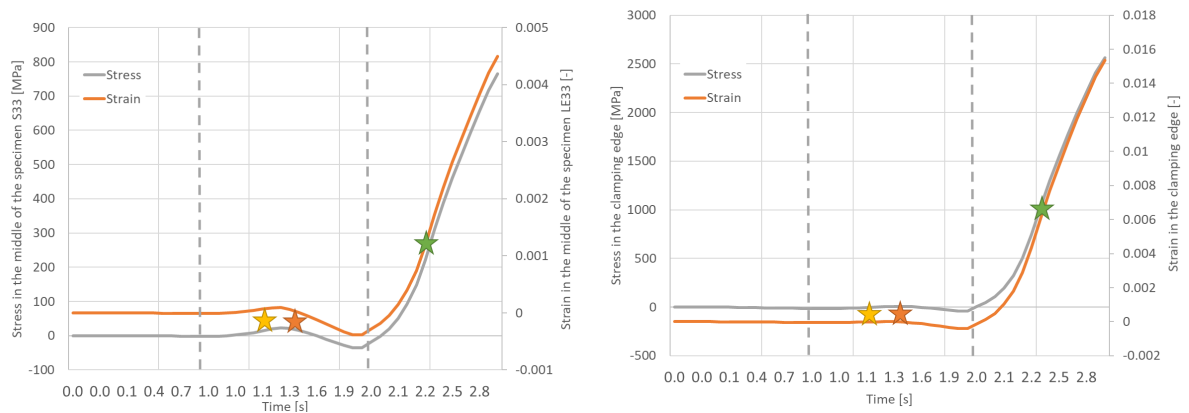
(a) Stress S33 and strain LE33 values in the specimen's centre, with the indication of the specific damage appearance (b) Stress S33 and strain LE33 values near the clamping edge, with the indication of the specific damage appearance

**Figure 3.40:** Stress and strain values for the specimen with the reinforcement width of 60 [mm] with the indication of the first damage appearance



(a) Stress S33 and strain LE33 values in the specimen's centre, with the indication of the specific damage appearance (b) Stress S33 and strain LE33 values near the clamping edge, with the indication of the specific damage appearance

**Figure 3.41:** Stress and strain values for the specimen with the reinforcement width of 80 [mm] with the indication of the first damage appearance



(a) Stress S33 and strain LE33 values in the specimen's centre, with the indication of the specific damage appearance (b) Stress S33 and strain LE33 values near the clamping edge, with the indication of the specific damage appearance

**Figure 3.42:** Stress and strain values for the specimen with the reinforcement width of 100 [mm] with the indication of the first damage appearance

Furthermore, in the case of the different reinforcement widths, the specimen's status just before the first damage appearance for different damage criteria can be seen in the Table 3.6 for all reinforcement options tested in this simulation set. The provided visualisation is the ABAQUS representation of the damage for all the elements present in the model. The damage is present when the value reaches 1. The legend is also provided in the table for ease of reading. The matrix cracking and fibre splitting are presented from the top side of the specimen, while the fibre kinking and fibre tensile failure are provided from the bottom. The specimen status after the first damage initiation is not provided as the LARC05 damage criterion can't provide damage evolution. Hence, the results at later stages are not relevant.

Reinf	Matrix cracking	Fiber split	Fiber kinking	Fiber tensile
RW60				
RW80				
RW100				
LEG	<p>LARCMCRTC Envelope (max) (Avg: 75%)</p> <ul style="list-style-type: none"> <li>+1.000e+00</li> <li>+9.229e-01</li> <li>+8.459e-01</li> <li>+7.688e-01</li> <li>+6.918e-01</li> <li>+6.147e-01</li> <li>+5.377e-01</li> <li>+4.606e-01</li> <li>+3.836e-01</li> <li>+3.065e-01</li> <li>+2.295e-01</li> <li>+1.524e-01</li> <li>+7.535e-02</li> </ul>	<p>LARCFSCRT Envelope (max) (Avg: 75%)</p> <ul style="list-style-type: none"> <li>+1.000e+00</li> <li>+9.157e-01</li> <li>+8.333e-01</li> <li>+7.500e-01</li> <li>+6.667e-01</li> <li>+5.833e-01</li> <li>+5.000e-01</li> <li>+4.167e-01</li> <li>+3.333e-01</li> <li>+2.500e-01</li> <li>+1.667e-01</li> <li>+8.333e-02</li> <li>+0.000e+00</li> </ul>	<p>LARCFKRTC Envelope (max) (Avg: 75%)</p> <ul style="list-style-type: none"> <li>+1.000e+00</li> <li>+9.157e-01</li> <li>+8.333e-01</li> <li>+7.500e-01</li> <li>+6.667e-01</li> <li>+5.833e-01</li> <li>+5.000e-01</li> <li>+4.167e-01</li> <li>+3.333e-01</li> <li>+2.500e-01</li> <li>+1.667e-01</li> <li>+8.333e-02</li> <li>+0.000e+00</li> </ul>	<p>LARCFTRC Envelope (max) (Avg: 75%)</p> <ul style="list-style-type: none"> <li>+1.000e+00</li> <li>+9.157e-01</li> <li>+8.333e-01</li> <li>+7.500e-01</li> <li>+6.667e-01</li> <li>+5.833e-01</li> <li>+5.000e-01</li> <li>+4.167e-01</li> <li>+3.333e-01</li> <li>+2.500e-01</li> <li>+1.667e-01</li> <li>+8.333e-02</li> <li>+0.000e+00</li> </ul>

**Table 3.6:** Specimen status just before or at the first damage appearance for each of the initial damage criterion and for all tested reinforcement's widths

### 3.2.4. Damage results for the single-sided and double-sided reinforcement

Finally, the effect of single vs double reinforcement has also been tested, and the damage analysis results are also provided. For both instances, the single and the double reinforcement, the values of stress and strain are plotted for the element in the specimen's centre. In the Figure 3.43a, the results for the single reinforcement are visualised, and in the Figure 3.43b for the double reinforcement. The first damage appearance for each criterion is indicated using stars as introduced in the Figure 3.31. The values for strain and stress near the clamping edge are not provided as, due to the double reinforcement, the high-stress position moved near the centre of the specimen. Hence, the comparison with the single reinforcement wouldn't be adequate.

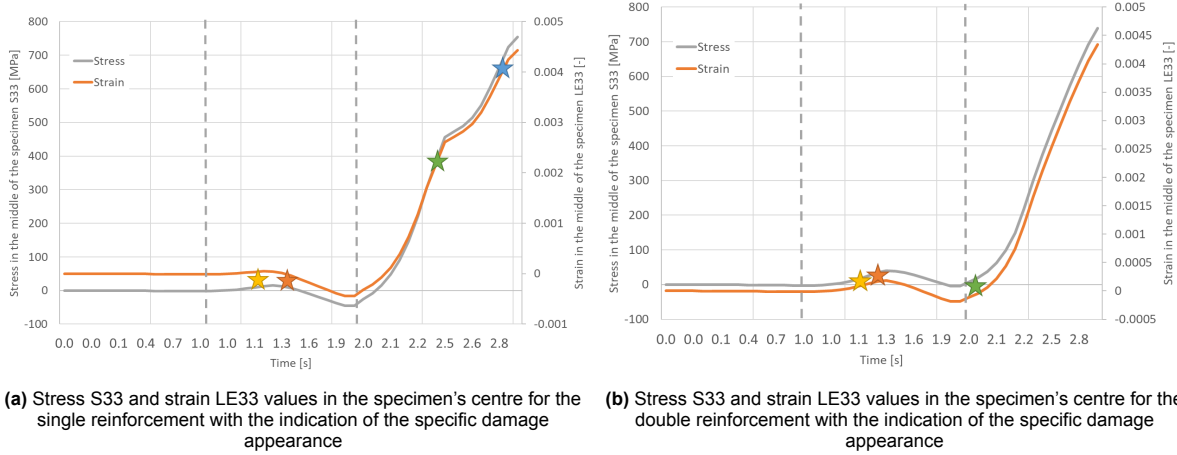


**Figure 3.43:** Stress and strain values for the specimen with single and double reinforcement with the indication of the first damage appearance

Moreover, both for the single and double reinforcement, the specimen's status just before the first damage appearance for different damage criteria can be seen in the Table 3.7 for all reinforcement options tested in this simulation set. The provided visualisation is the ABAQUS representation of the damage for all the elements present in the model. The damage is present when the value reaches 1. The legend is also provided in the table for ease of reading. The matrix cracking and fibre splitting are presented from the top side of the specimen, while the fibre kinking and fibre tensile failure are provided from the bottom. The specimen status after the first damage initiation is not provided as the LARC05 damage criterion can't provide damage evolution. Hence, the results at later stages are not relevant.

Reinf	Matrix cracking	Fiber split	Fiber kinking	Fiber tensile
single				
double				
LEG	LARCMCRT Envelope (max) (Avg: 75%) +1.000e+00 +9.229e-01 +8.459e-01 +7.689e-01 +6.919e-01 +6.147e-01 +5.377e-01 +4.606e-01 +3.835e-01 +3.065e-01 +2.295e-01 +1.524e-01 +7.535e-02	LARCFSCRT Envelope (max) (Avg: 75%) +1.000e+00 +9.167e-01 +8.339e-01 +7.500e-01 +6.667e-01 +5.833e-01 +5.000e-01 +4.167e-01 +3.333e-01 +2.500e-01 +1.667e-01 +8.333e-02 +0.000e+00	LARCFKCRT Envelope (max) (Avg: 75%) +1.000e+00 +9.167e-01 +8.333e-01 +7.500e-01 +6.667e-01 +5.833e-01 +5.000e-01 +4.167e-01 +3.333e-01 +2.500e-01 +1.667e-01 +8.333e-02 +0.000e+00	LARCFTRT Envelope (max) (Avg: 75%) +1.000e+00 +9.167e-01 +8.333e-01 +7.500e-01 +6.667e-01 +5.833e-01 +5.000e-01 +4.167e-01 +3.333e-01 +2.500e-01 +1.667e-01 +8.333e-02 +0.000e+00

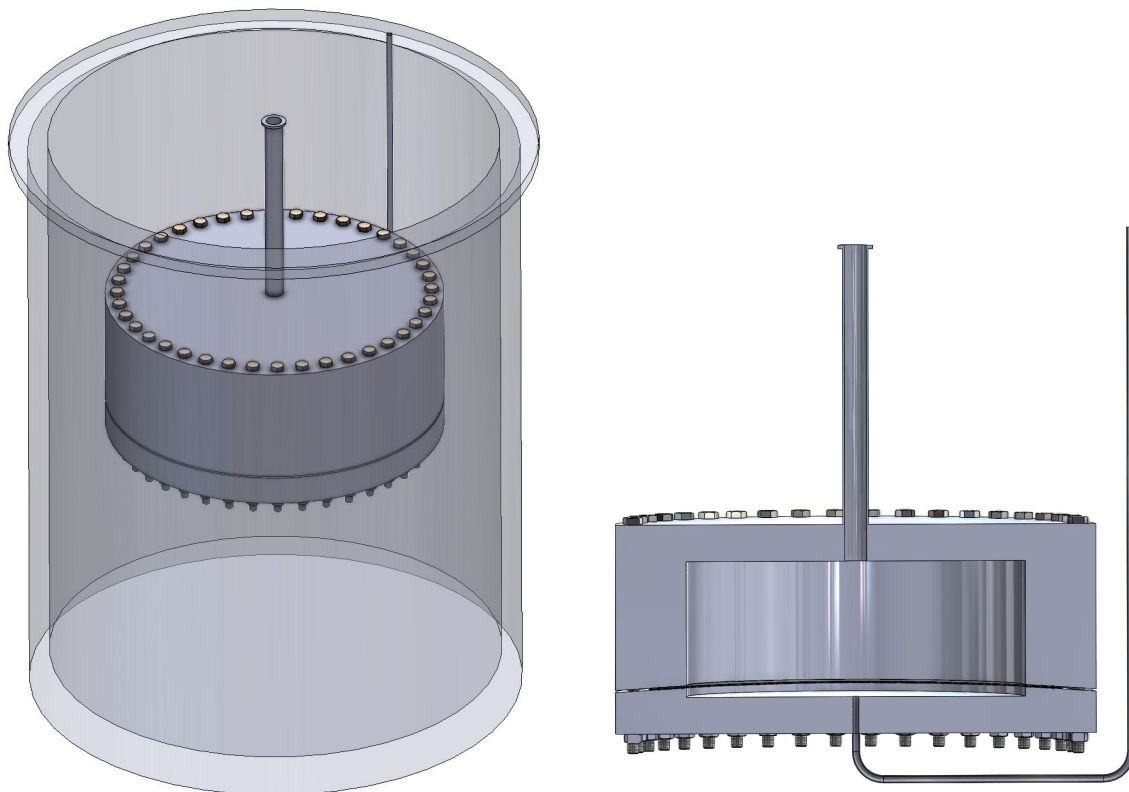
**Table 3.7:** Specimen status just before or at the first damage appearance for each of the initial damage criteria for both single and double reinforcement

### 3.3. Thermal modelling results

As a final analysis, the results of the thermal modelling are provided. Firstly, based on the more detailed design, the heat capacity of the testing rig is calculated, and the necessary amount of liquid nitrogen is also estimated. Then, the results of the thermal analysis for the estimation of the heat flux are shown. Finally, the specimen cooling characteristics present during thermal simulation are shown.

#### Heat capacity

To estimate the heat capacity, the updated model of the testing rig has been modelled in the CAD software as present in the Figure 3.44. From that model, the volume of each part could have been derived. The design volumes and the materials' specific properties are presented in the Table 3.8. For this analysis, the two most probable material candidates for the testing rig, namely stainless steel and Invar, have been used. Based on those estimates, the calculations are provided below to estimate the required cooling energy and the amount of liquid nitrogen.



(a) Visualisation of the testing rig used for the heat capacity calculations inside the dewar

(b) Cross-section view of the testing rig used for the heat capacity calculations

**Figure 3.44:** Models of the testing rig used for the heat capacity calculations and thermal analysis

Material Properties		Estimates from the CAD	
Specific heat (Steel) [ $J/kgK$ ]	<b>500</b>	Volume of upper enclosure [ $m^3$ ]	<b>0.02259</b>
Specific heat (Invar) [ $J/kgK$ ]	<b>505</b>	Volume of lower enclosure [ $m^3$ ]	<b>0.00920</b>
Specific heat (CFRP) [ $J/kgK$ ]	<b>1040</b>	Volume of the specimen [ $m^3$ ]	<b>0.00032</b>
Specific heat (helium) [ $J/kgK$ ]	<b>5188</b>	Volume of the bolts [ $m^3$ ]	<b>0.00128</b>
Density (Steel) [ $kg/m^3$ ]	<b>8000</b>	Volume of the enclosed helium [ $m^3$ ]	<b>0.00161</b>
Density (Invar) [ $kg/m^3$ ]	<b>8100</b>	Enclosed volume of upper enclosure [ $m^3$ ]	<b>0.01452</b>
Density (CFRP) [ $kg/m^3$ ]	<b>1540</b>	Volume of the nuts [ $m^3$ ]	<b>0.00009</b>
Density (helium @20 bar) [ $kg/m^3$ ]	<b>10</b>	Volume of the steel pipes [ $m^3$ ]	<b>0.00006</b>

**Table 3.8:** Inputs for the estimation of the liquid nitrogen volume necessary for the cooling of the setup

To estimate the necessary energy to cool down the entire testing rig to the liquid nitrogen temperature, the following equation has been used:

$$Q = m * C_p * \Delta T \tag{3.1}$$

Where  $\Delta T$  can be obtained by taking the difference between the room temperature and liquid nitrogen temperature in the following way:

$$\Delta T = 293 - 77 = 216[K] \tag{3.2}$$

The mass  $m$  and specific heat  $C_p$  can be obtained from the Table 3.8. Then, by following the Equation 3.1, the total energy required to cool down the rig to the liquid nitrogen temperature can be calculated. Firstly, for the steel option:

$$Q_{total}(Steel) = 28830824[J] \tag{3.3}$$

Then, for the Invar option:

$$Q_{total}(Invar) = 29480209[J] \tag{3.4}$$

Based on those obtained values and the vaporisation energy of liquid nitrogen equal to 199 [kJ/kg], the amount of coolant can be estimated for both options. For steel option **144.88 [kg]** of liquid nitrogen is needed, while for the Invar option around **148.14 [kg]**.

The cooling process

In this section, the results of the thermal simulation are presented. The heat flux of the testing rig is presented in the Figure 3.45 and the heat flux of the specimen itself in the Figure 3.46. The temperature distribution of the setup at the point of the highest heat flux of the specimen is also shown in the Figure 3.47. The results are presented for both cooling methods with and without the pre-cooling step with the cold nitrogen gas.

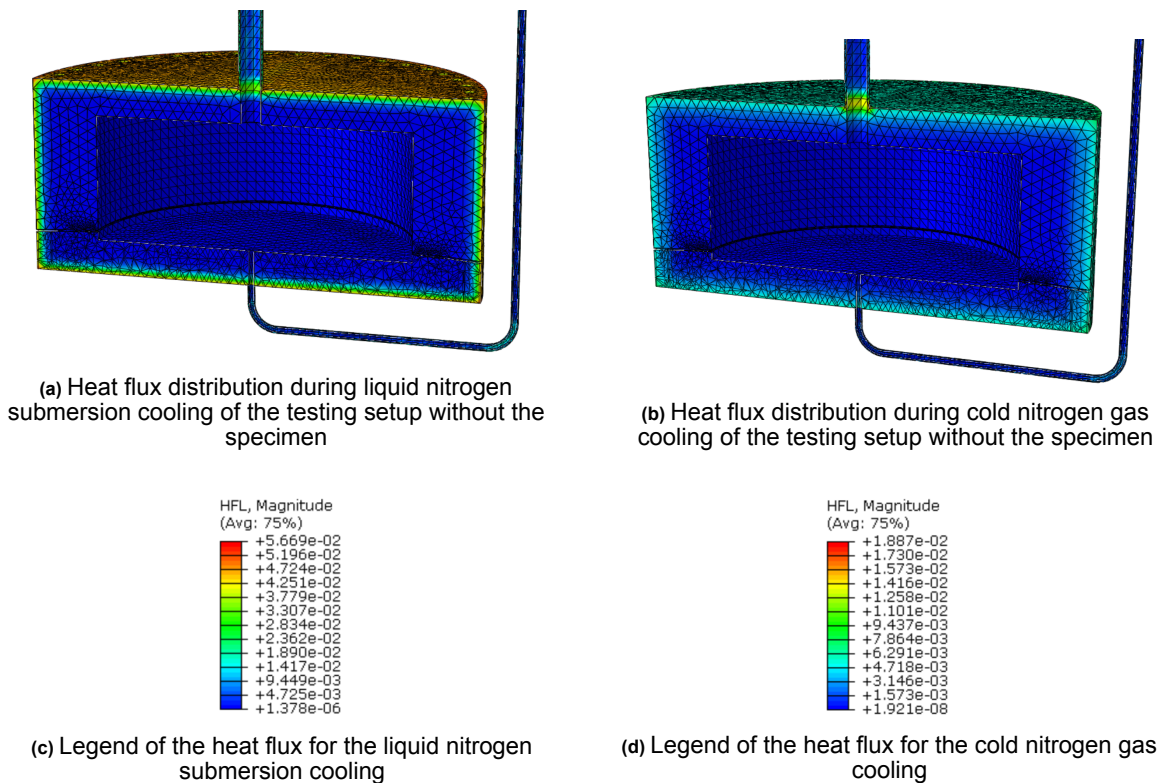
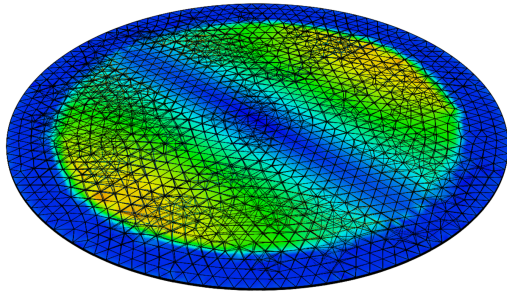
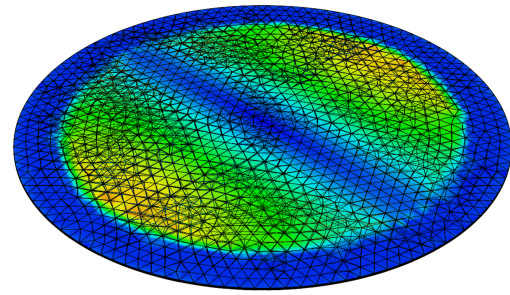


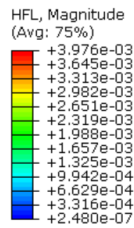
Figure 3.45: Heat flux results for the testing rig without the specimen for the liquid nitrogen cooling and cold nitrogen gas cooling



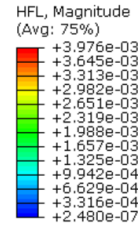
(a) Heat flux distribution on the specimen at the point of maximum registered heat flux from the specimen's centre without the pre-cooling step



(b) Heat flux distribution on the specimen at the point of maximum registered heat flux from the specimen's centre with the pre-cooling step

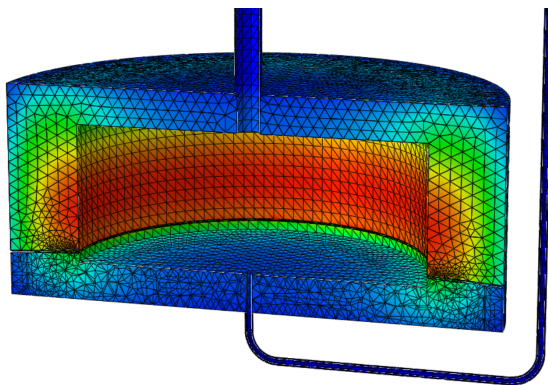


(c) Legend for the heat flux distribution for the method without the pre-cooling step

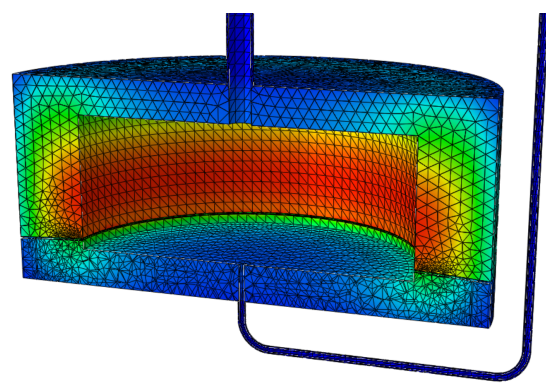


(d) Legend for the heat flux distribution for the method with the pre-cooling step

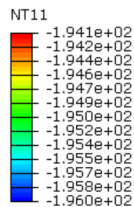
**Figure 3.46:** Heat flux results for the specimen at the point of maximum registered heat flux at the specimen's centre for method with and without pre-cooling step



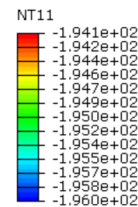
(a) Temperature distribution at the testing rig excluding the specimen at the point of maximum heat flux registered at the specimen's centre for the method without the pre-cooling step



(b) Temperature distribution at the testing rig excluding the specimen at the point of maximum heat flux registered at the specimen's centre for the method with the pre-cooling step



(c) Legend for the temperature distribution for the method without the pre-cooling step

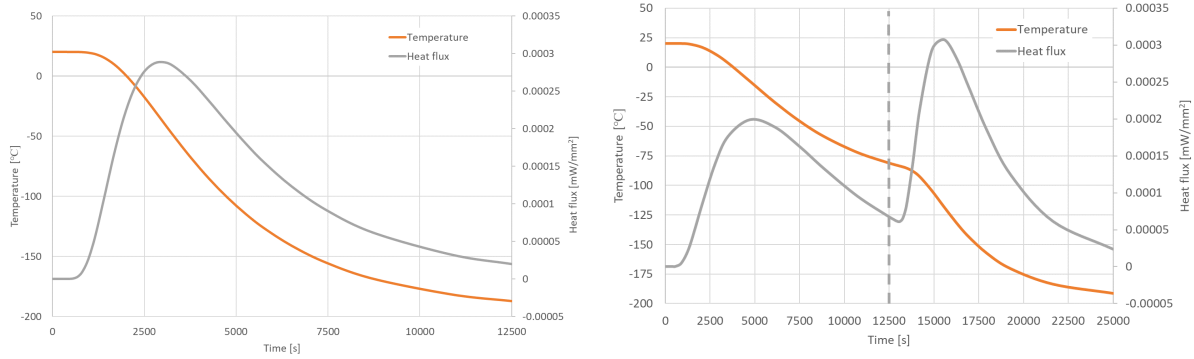


(d) Legend for the temperature distribution for the method with the pre-cooling step

**Figure 3.47:** Temperature distribution results for the testing rig at the point of maximum heat flux present at the specimen's centre for the method with and without the pre-cooling step

Specimen cooling

Finally, the specimen cooling results are also presented. Firstly, the heat flux and the temperature of the specimen over time for both cooling methods with and without the pre-cooling step are presented in the Figure 3.48. Then, the graphical representation of the specimen at various points during the process is shown. The steps at the maximum heat flux point and the end of the analysis are showcased.



(a) Temperature change for the specimen's centre during liquid nitrogen submersion cooling (b) Temperature change for the specimen's centre during cold gas pre-cooling and liquid nitrogen cooling

Figure 3.48: Temperature change for the specimen's centre with a and without pre-cooling step

Step	w/o pre-cooling	with pre-cooling
Max heat flux point		
End of the pre-cooling	N/A	
End of the cooling		
Legend	<p>NT11</p> <ul style="list-style-type: none"> <li>-3.656e+01</li> <li>-4.985e+01</li> <li>-6.314e+01</li> <li>-7.642e+01</li> <li>-8.971e+01</li> <li>-1.030e+02</li> <li>-1.163e+02</li> <li>-1.296e+02</li> <li>-1.429e+02</li> <li>-1.561e+02</li> <li>-1.694e+02</li> <li>-1.827e+02</li> <li>-1.960e+02</li> </ul>	<p>NT11</p> <ul style="list-style-type: none"> <li>-8.115e+01</li> <li>-9.072e+01</li> <li>-1.003e+02</li> <li>-1.099e+02</li> <li>-1.194e+02</li> <li>-1.290e+02</li> <li>-1.386e+02</li> <li>-1.481e+02</li> <li>-1.577e+02</li> <li>-1.673e+02</li> <li>-1.769e+02</li> <li>-1.864e+02</li> <li>-1.960e+02</li> </ul>

Table 3.9: Specimen status at different points during the cooling procedure for the method with the pre-cooling step and the method with the pure liquid nitrogen submersion cooling.

Due to the narrow range of the temperature at the end of the cooling, it seems that the specimen

had a uniform distribution. But at the end of the analysis, the specimen with the pre-cooling step had the following temperature distribution [-192, -196], and without the pre-cooling step, the distribution was [-187, -196]

**Helium consideration**

To see the influence of helium on cooling results for the testing rig, the simulation following the methodology from the subsection 2.2.8 has been performed. The results for both the specimen and the bottom enclosure that will be in contact with the gas are presented below. The temperature and the heat flux over time in the specimen's centre are shown in the Figure 3.49, together with the temperature and heat flux for the bottom enclosure over the same time period. The temperature distribution present in the testing rig during helium heating can be seen in the Figure 3.50.

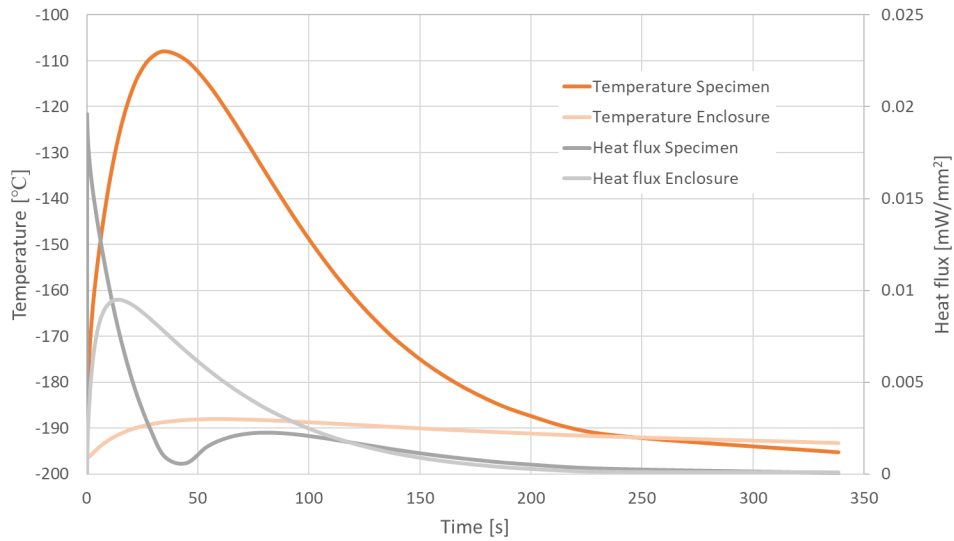


**Figure 3.49:** Temperature and heat flux change for the specimen's centre and the bottom enclosure of the permeation setup during the application of warmer helium gas to the system.

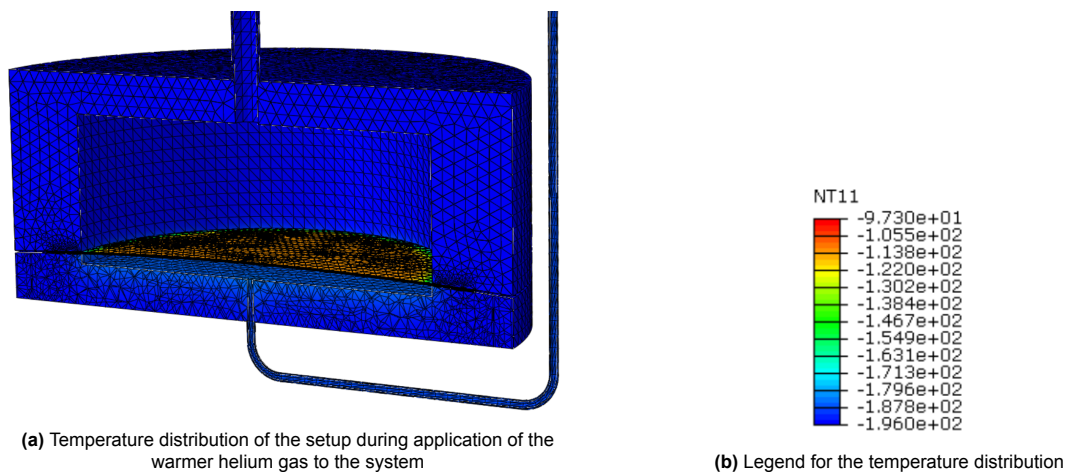


**Figure 3.50:** Effect of the warmer helium gas on the temperature distribution of the testing setup

**3.3.1. Other cooling methods**

The results of other cooling methods that are considered are presented as a final analysis. Firstly, the cooling outcome of the method with the pre-cooled nitrogen gas is shown. Then, the results of the

thermostat method are presented. Finally, the improved testing rig with the additional fins is considered. The results are mostly shown for the specimen cooling and not the enclosure.

**Cold gas cooling**

The temperature distribution of the testing setup during the cold gas cooling method is provided in the Figure 3.51. The temperature change and heat flux registered in the specimen's centre for this type of cooling is shown in the Figure 3.52. In the Figure 3.52a, the entire duration of the analysis is plotted, but in the Figure 3.52b, the detailed view at the beginning of the cooling process is presented. Finally, in the Figure 3.53, the heat flux distribution across the specimen is shown at the point of the maximum heat flux registered in the specimen's centre.

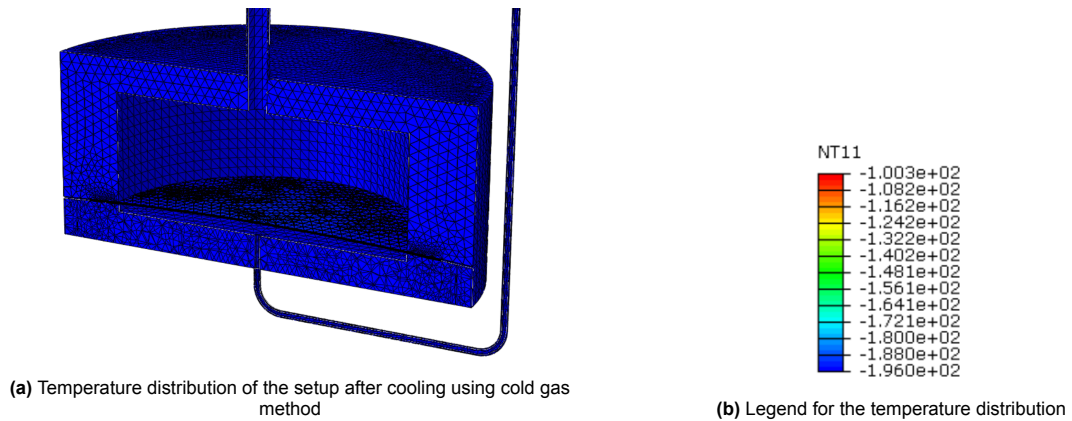


**Figure 3.51:** Effect of the Cold gas cooling method on the temperature distribution of the testing setup

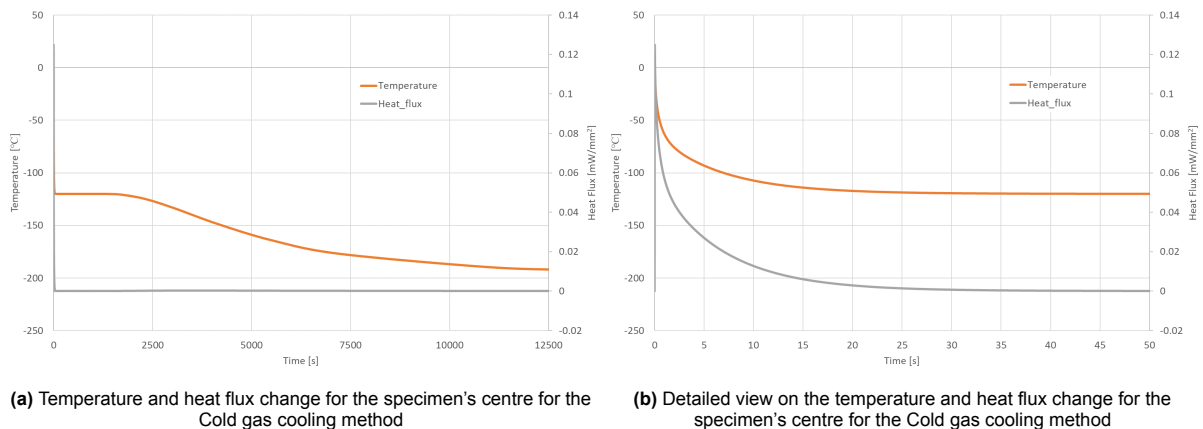


**Figure 3.52:** Effect of the cold gas cooling on the temperature and heat flux of the specimen

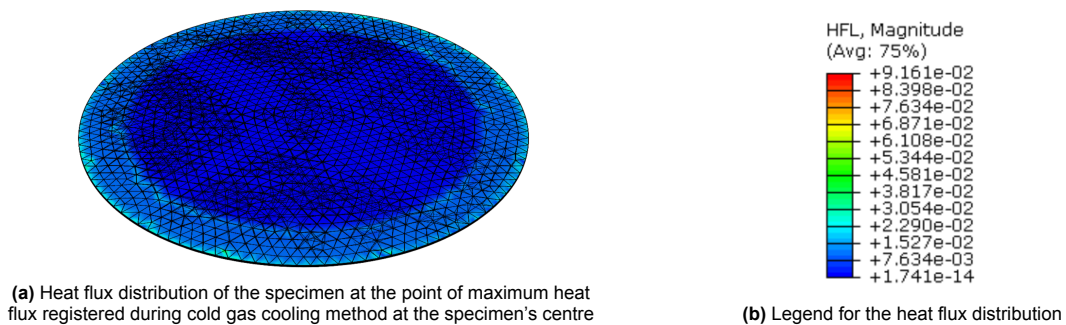


**Figure 3.53:** Effect of the cold gas cooling on the heat flux distribution of the specimen

**Cryostat cooling**

The temperature distribution of the testing setup during the cryostat cooling method is provided in the Figure 3.54. The temperature change and heat flux registered in the specimen's centre for this type of cooling is shown in the Figure 3.55. Finally, in the Figure 3.56, the heat flux distribution across the specimen is shown at the point of the maximum heat flux registered in the specimen's centre.

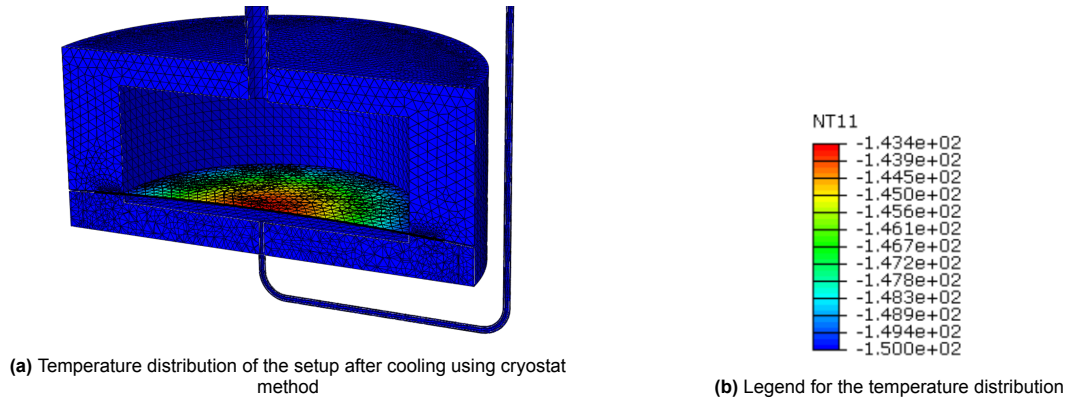


**Figure 3.54:** Effect of the Cryostat cooling method on the temperature distribution of the testing setup

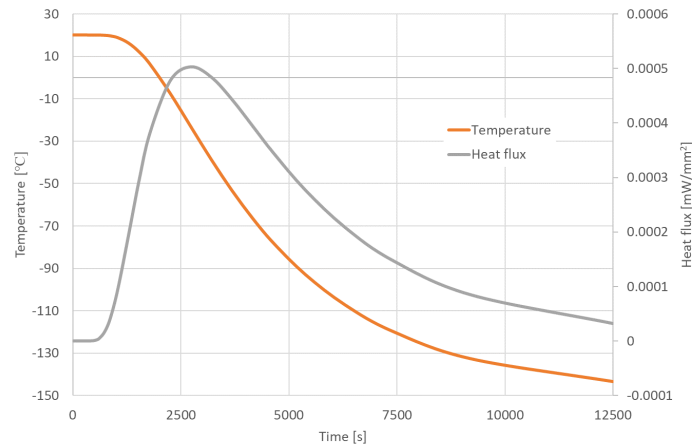


**Figure 3.55:** Effect of the cryostat cooling method on the temperature and heat flux of the specimen at the point of the maximum heat flux registered in the specimen's centre

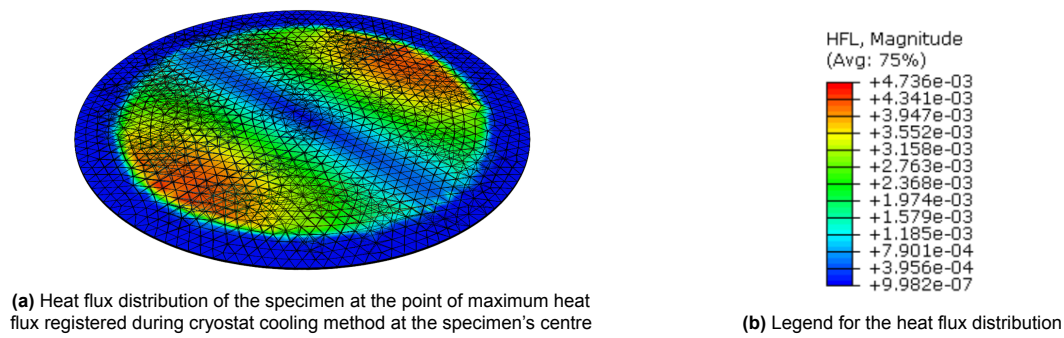


**Figure 3.56:** Effect of the cryostat cooling method on the heat flux distribution of the specimen

**Addition of cooling fins**

The temperature distribution of the testing setup during the cooling with the additional cooling fins is

provided in the Figure 3.57. The temperature change and heat flux registered in the specimen's centre for this type of cooling is shown in the Figure 3.58. Finally, in the Figure 3.59, the heat flux distribution across the specimen is shown at the point of the maximum heat flux registered in the specimen's centre.

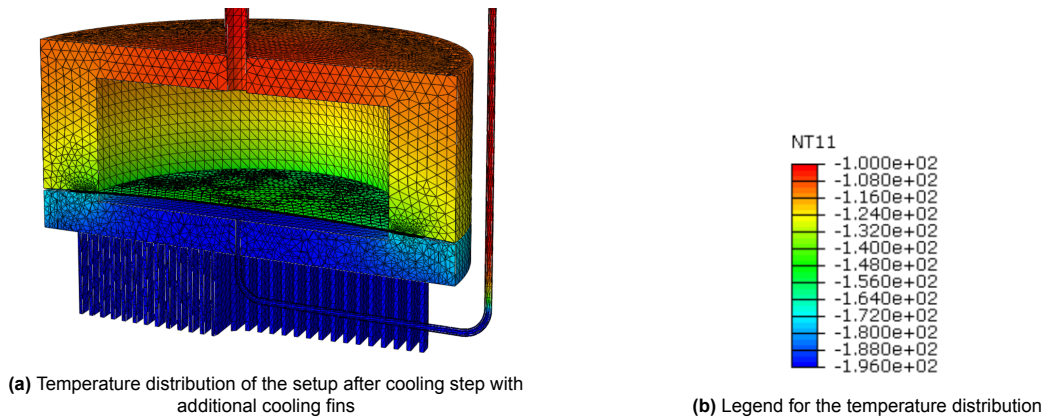


Figure 3.57: Effect of the cooling fins on the temperature distribution of the testing setup

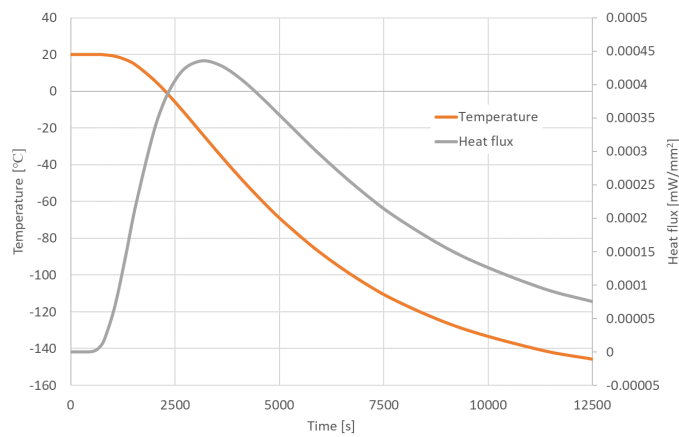


Figure 3.58: Effect of the cooling fins on the temperature and heat flux of the specimen at the point of the maximum heat flux registered in the specimen's centre

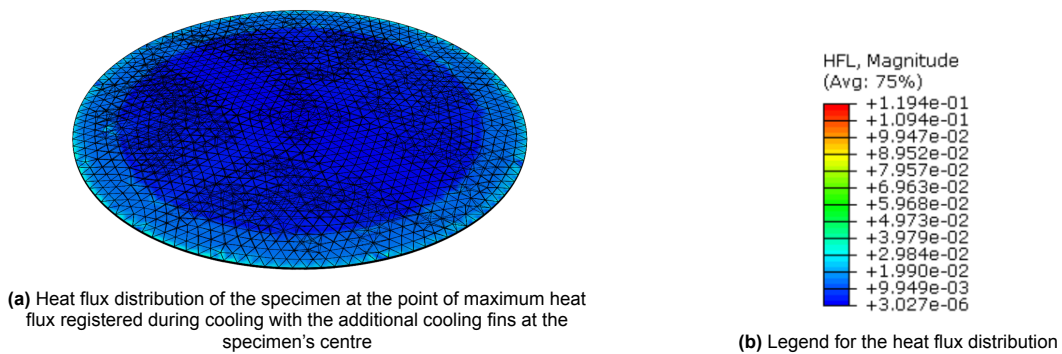


Figure 3.59: Effect of the cooling fins on the heat flux distribution of the specimen

# 4

## Discussions

In this chapter, the obtained results are discussed. Firstly, the findings of the parametric study are presented. The dependencies and specific influences of the parameters on the results are outlined. Furthermore, each parameter effect on the equal bi-axial zone is detailed and discussed. The damage analysis outcomes are also provided, and their effect on the bulge bi-axial testing is argued. The recommendation for suitable reinforcement is given, taking into account fibre damage and the practicality of each option. Finally, the thermal aspect of the setup is discussed, where different options for cooling are compared. Based on those findings, advice on the right approach for cooling is presented, considering aspects like the cooling rate, the minimum achievable temperature, and the economics of the option.

## 4.1. Effect of different parameters

Firstly, the outcome of the parametric study is described and discussed. Each of the outlined parameters is presented separately, and the results of the corresponding studies are deeply analysed. The essential factor of the parametric study was finding the specimen characteristics with the realistic stress state. Hence, the focus is on the maximum strain reached in the middle of the specimen and the equal bi-axial zone. However, any unexpected findings or dependencies are also discussed to provide a more complete view.

### 4.1.1. Influence of the diameter

Regardless of the path used, considering both in-plane strains, the maximum strain reached at the specimen's centre for the different diameters is between 0.003 and 0.005. As presented in the Figure 2.1.4, the relevant strain for the hydrogen tank is between 0.004 and 0.005 microstrain. Taking this into account, only specimens with a diameter larger than 350 [mm] reached that strain bracket at least at the top layer of the laminate, as seen in the Figure 3.3c or Figure 3.3d. The bottom layer of the specimen shows a decrease in the strain, as shown in the Figure 3.4c and Figure 3.4d. In this case, the value of the 0.004 microstrains is not even reached for the largest specimen with a diameter of 650 [mm]. Furthermore, as expected, the stresses present in the laminate increase with the diameter and the testing surface, and they reach a reasonable value in the specimen's centre between 175 and 250 [MPa] for the S11 stress factor and maximum value of 800 [MPa] for the S33 stress.

Unfortunately, the stress concentration near the clamping regions increases with the increase in diameter. For the largest specimen, the LE11 strain reaches even 0.034 microstrains as seen in the Figure 3.3c, which is most likely beyond the material's capabilities, which raises the question of material damage. That's why the damage analysis was also performed, and it is presented later in the section 4.2. Furthermore, by comparing the peaks in stress and strain near the clamping region, especially from the Figure 3.3a and Figure 3.4a, it is clear that the specimen is in compression at the top and in tension at the bottom of the laminate, straight after the clamping zone and only after certain distance both sides of the specimen are in tension. This behaviour is expected as the circular specimen experiences inward bending around the clamping zone.

Moreover, by looking at the slope of the strain, from the clamping zone to the specimen's centre, it can be noticed that the slope increases slightly with the increasing diameter as visible in the Figure 3.3d for example. This indicates that the more significant portion of the specimen diameter should have a steady strain value, essential for the equal bi-axial strain zone. The study of the bi-axial zone confirms this. When both the top and bottom layers of the specimen are considered, the equal bi-axial zone is only reached for the specimen with a diameter of 450 [mm], as seen in the Figure 3.5d. This theory is also confirmed by looking at the graph for the largest specimen in the Figure 3.5f, where the curves for the top and bottom layer of the specimen almost perfectly align with each other. However, when only the top layer of the specimen is considered, the equal bi-axial strain zone increases with the diameter magnitude. But this statement is only valid in absolute terms; from the relative point of view, all tested specimens have an equal bi-axial zone of around 25% of the total diameter.

### 4.1.2. Influence of the curvature

Looking at the results for the top path in the Figure 3.8 and the bottom path in the Figure 3.9, the difference in the maximum strain reached in the specimen's centre for all tested curvatures is minimal, equal to around 0.002 microstrains. However, for the top layer of the specimen, the highest strain is reached for the flat specimen as seen in the Figure 3.8c and Figure 3.8d, which can be translated to the specimen with infinite curvature. On the other hand, the opposite is true for the bottom layer of the specimen, where the highest strain is achieved for the specimen with the smallest curvature. Unfortunately, regardless of the curvature, the strain achievable for the tested conditions only surpasses the 0.004 microstrain at the top, while it barely reaches 0.002 microstrain at the bottom.

In the case of the clamping zone, it is clear that as the curvature approaches infinity, as in the case of the flat specimen, the stress concentration increases with it, reaching 0.032 microstrains in the Figure 3.9c. However, this also means the stress concentration is reduced for the smaller curvature specimens around 1000 or 2000 [mm]. Hence, to avoid specimen damage near the clamping zone, it would be advised to use specimens with a smaller curvature. But then the question of the representative condition arises. As discussed in the subsection 2.1.6, the value of around 3000 [mm] seems the most

reasonable for the hydrogen tank for aviation applications.

When looking at the equal bi-axial strain for the different specimen's curvatures, there is a minimal deviation, at least for the top layer of the specimen as presented in the Figure 3.10. There is an increase in the zone for the specimen with the smallest curvature of around 10 [mm] across the entire diameter. The difference between the specimens is much more profound at the bottom layer, where the smallest zone is present for the flat specimen, followed by the specimen with a diameter of 5000 [mm], seen in the Figure 3.11. Conversely, the largest zone is for the specimen with a curvature of 1000 [mm], and the increase seems substantial at around 100 [mm] across the entire diameter. This shows that smaller curvatures for the specimens positively affect the size of the equal bi-axial zone. This might also be explained by the lower stress concentration at the clamping zone, which translates to the more stable strain and stress values in the laminate's centre.

#### 4.1.3. Influence of the thickness

A significant influence on stress and strain can be seen between the specimens with different material thicknesses as seen in the Figure 3.14 or Figure 3.15. The difference in strain between the thinnest and thickest specimen is even 0.009 microstrains for the LE11 at the bottom path as presented in the Figure 3.15c. The thinnest specimen reaches 0.007 microstrains at the top in the Figure 3.14c and just below 0.006 microstrains at the bottom in the Figure 3.15c for the LE11 strain. Meanwhile, the thickest laminate barely stays at around 0.002 microstrains for the top layer and goes into negative values at the bottom. This confirms that the setup with a 450 [mm] diameter specimen can reach the desired strain levels for thin laminates, but thicker laminates need further adjustments of the testing conditions.

Unfortunately, with the increase of the strain levels at the specimen's centre for the thinner laminates, the stress concentration near the clamping zone also increases. For the 1 [mm] specimen, the peak strain is measured at -0.038 microstrains for the LE11 at the top layer as seen in the Figure 3.14c. On the other hand, the maximum strain for the thickest plate of 10 [mm] is around -0.007 microstrain. This indicates that thicker laminates have significantly lower stresses inside the laminate. Furthermore, the bending is not as severe as for the thinner specimens, as seen in the vertical displacement graph in the Figure 3.13. The difference in the maximum deflection between the tested specimens is almost 26 [mm].

In the case of the equal bi-axial zone, it seems that thinner laminates are better for achieving the right stress state, as seen in the Figure 3.16, at least for the top layer of the specimen. However, in the case of the bottom layer, the situation is not as clear. The best laminate out of the ones tested has a thickness of 5 [mm], but the thinnest laminates with 1 and 2 [mm] thickness are not that much worse. However, the laminates with 3 [mm] and 10 [mm] thickness perform very poorly; in the case of the smaller one, the equal bi-axial zone is not even reached. Hence, specimens with a reasonably small thickness are advisable to achieve membrane testing conditions.

#### 4.1.4. Influence of the pressure

The increase in pressure increases the loading acting on the specimen. That's why, at higher pressures, higher strains are present in the specimen's centre. For the highest pressure of 25 [bar], the specimen can achieve almost 0.005 microstrains at the top layer, as seen in the Figure 3.20c and almost 0.003 microstrains at the bottom layer, as shown in the Figure 3.21c. In the case of the loading with the lowest tested pressure of 5 [bar], the achievable strain decreases to 0.001 microstrains for the top and 0 microstrains for the bottom layer. This indicates that the pressure increase corresponds to the increase in stress and strain. Furthermore, pressure adjustment can be regarded as the easiest method to implement if different stress and strain values are needed during testing. For most of the setups from the literature [81] and industry, simple pressure valve is needed to modify the desired pressure. Also, after a closer look at the graphs, especially the ones for the LE33 strain seen in the Figure 3.20d or Figure 3.21d, the increase in pressure correspond to the linear increase in strain, when comparing the values for the 10 [bar] and 20 [bar] or 5 [bar] and 10 [bar].

However, this linear increase is absent for the stress concentration near the clamping zone. As expected, the stress and strain increase at the clamping location with a higher loading, but the response is weaker and not linear. Unfortunately, in any case, the stress concentration is still significant and reaches a maximum of almost 0.032 microstrains for the LE11, as seen in the Figure 3.21c. Based on those findings, pressure is an excellent way of increasing strain in the specimen's centre, as the penalty due to the stress concentration is not as severe when comparing it to the gain in the reachable stress

and strain values. However, solutions to decrease the stress concentration should still be applied to avoid specimen damage for the actual testing conditions.

When looking at the equal bi-axial strain analysis results, it is clear that a higher force creates better conditions. Regardless of the specimen side, the zone is consistently higher for the specimens with higher pressure, as seen in the Figure 3.22 and Figure 3.23. And the zone is the largest for the highest tested pressure of 25 [bar]. Furthermore, while all tested pressures achieved equal bi-axial zones at the top of the specimen, this wasn't the case for the bottom layer. Looking at the results presented in the Figure 3.23, the minimum pressure to achieve an equal bi-axial zone in the specimen's centre is larger than 10 [bar] for the specimen with diameter of 450 [mm] and thickness of 2 [mm].

#### 4.1.5. Influence of the layup

In the case of the final tested parameter, the chosen layup of the specimen, the difference is the most significant, as the in-plane stiffness distribution between the analyses is hugely different. The maximum LE11 strain in the specimen's centre is achieved for the CP and QI laminate, with the latter being slightly higher above 0.004 microstrains, as seen in the Figure 3.27c. In the case of the LE33 strain, the most considerable value is reached for the uni-directional laminate, going beyond 0.012 microstrains, as shown in the Figure 3.27d. The asymmetric behaviour of the UD laminate is also visible in the vertical displacement as presented in the Figure 3.25. In general, the difference in the strain response, especially for the centre of the laminate, is very similar for the CP and QI laminate. But this statement doesn't hold for the stress response as the difference is significant. This is most likely caused by the fact that the top and bottom layers between those two layups are not the same. For the QI, the outer layers have a 0-degree angle, while the CP laminate has a 90-degree outer layer.

The significant difference between the tested layups stays for the stress concentration near the clamping zone. The most considerable LE11 strain for the top layer is achieved for the QI laminate, while the CP achieves a higher strain value for the bottom layer. In the case of the LE33 strain, regardless of the path used, the UD laminate reaches the highest strain value. The value of -0.071 microstrain is even reached at the top layer of the specimen for this layup, as shown in the Figure 3.28d.

Finally, looking at the outcome of the equal bi-axial zone study, it can be concluded that a CP laminate performs slightly better than a QI laminate. For the top layer of the specimen, the zone is more than 10 [mm] larger for the cross-ply, while for the bottom layer, the zone is visually almost the same. However, the strain ratio stays flatter and closer to the agreed value for longer in the case of the CP layup.

## 4.2. Damage and element testing

The parametric study showed that the specimen experiences large strains and stresses near the clamping regions. A damage analysis has been performed to see if this can impair the laminate. As the analysis used LARC05, the matrix cracking, fibre splitting, fibre kinking and fibre tensile failure were considered.

Firstly, the specimen from the parametric study was analysed, having the same parameters as the main configuration. The plots show that every kind of damage initiation appeared during the simulation, as shown in the Figure 3.32. The matrix failure and fibre splitting had already appeared during the cooling step, which proves the study done by French et al. [35], where matrix cracking was predominantly present when the specimen was cooled while clamped. During the loading step, fibre kinking and fibre tensile failure were present, which indicates that the specimen most likely wouldn't survive the test. From the results presented in the Figure 3.32b, it can be deduced that the tensile failure of the specimen appears around 0.016 microstrains. The values for this graph were plotted for the element with the most significant stress concentration, where the tensile failure was present at the end of the analysis. The value of 0.016 microstrains is significantly lower than some values reported during the parametric study, which highlights the issue of the stress concentration due to the clamping and creates a necessity for reinforcement in that region, as also reported by the Estrada et al. [30]. When taking a closer look at the different states of the laminate at the point of the damage as presented in the Table 3.2, it can be noticed that matrix cracking appears almost simultaneously across the entire surface between the clamping zone. Fibre splitting, on the other hand, seems to start in the specimen's centre. In the case of the fibre kinking and fibre tensile, the damage appears at the point of stress concentration near the clamping zone. These findings suggest that possible reinforcement can help

mainly with fibre kinking or tensile failure, as they are primarily present due to the excessive bending near the clamping. At the same time, other damage is limited mainly by the material characteristics. But this helps the testing procedure during permeation and leakage testing, as the material is meant to be pushed to its limits. The condition should induce crack formation, which appears primarily inside the matrix. However, fibre tensile failure can't happen as that could cause significant damage to the sensitive measurement equipment.

#### 4.2.1. Influence of the reinforcement

As it was suggested above, the specimen in its normal conditions, when subjected to the 20 [bar] of pressure loading, will most likely experience catastrophic failure during the testing. Such an outcome of the test is undesirable as it would most likely damage sensitive equipment used for the measurements. Hence, a way to reduce the chance of tensile failure damage has to be considered. That's why different kinds of reinforcement were tested to see if they can prohibit excessive damage to the laminate.

Starting with the reinforcement of the different thicknesses as seen in the Figure 3.33, Figure 3.34 and Figure 3.35, it can be noticed that the tensile damage criteria improved by adding the reinforcement to the specimen, regardless of the option used. When increasing the thickness, the point at which the ultimate fibre failure appears is delayed, as the maximum strain at the edge is also reduced. Furthermore, the tensile failure is not even present in the specimen with the thickest reinforcement, as seen in the Figure 3.35. On the other hand, the fibre splitting and kinking seem to be not influenced by the presence of the reinforcement. Matrix cracking appears slightly later in the analysis at higher strain values than in the case of the simple specimen, but it is still present during the cooling step. Also, when looking at the maximum strain present in the specimen's centre, the value is not affected by the reinforcement as even for the thickest option, the strain is above 0.004 microstrains, as seen in the Figure 3.35a. Unfortunately, when specimen status is concerned, the reinforcement has a significant influence. Matrix cracking seems to originate from the region with the reinforcement as seen in the Table 3.3. Fibre splitting, instead of the specimen centre, appears underneath the reinforcement. The change is less severe in the case of fibre tensile failure and fibre kinking. The stress concentration region seems more spread out and pushed towards the centre due to the reinforcement in case of those damage criteria.

When considering different material options for the reinforcement, an increase in stiffness positively influences the specimen. Looking at the analysis results for the steel, as presented in the Figure 3.36, the fibre tensile failure is not present, and fibre kinking is significantly delayed. However, the strain at the end of the analysis with the steel reinforcement is just above the 0.016 microstrains, indicating that even a slight increase in loading could cause a failure. In the case of composite reinforcement, tensile failure is still present, but fibre kinking is absent. However, if the laminate is rotated by 45 degrees, the fibre kinking would be again present as seen in the Figure 3.39. In the case of matrix cracking and fibre splitting, the influence of the different materials is similar to the difference in thickness. This suggests that those damage criteria see a slight improvement by simply placing any reinforcement. The specimen status presented in the Table 3.4 is influenced similarly by uniform materials such as steel and aluminium. Composite reinforcement, on the other hand, doesn't show the same connection. The matrix cracking and the fibre splitting show no significant alteration after adding the composite reinforcement.

In the case of the different reinforcement widths, the tensile failures are only absent for the widest reinforcement of 100 [mm]. Still, once again, the strain value at the end of this simulation suggests that the material is very close to failure. In the case of the other widths, the presented results in the Figure 3.40 and the Figure 3.41 show that there is a minimal difference between the reinforcement with the width of 60 and 80 [mm]. However, the maximum strain is reduced for the wider ring, but not enough to prohibit tensile failure. The other criteria, like matrix cracking and fibre splitting, show almost no change between the different reinforcements. When looking at the specimen status presented in the Table 3.6, the zone of the influence for the matrix cracking and fibre splitting increases with the reinforcement widths, as expected. Fibre tensile and kinking show similar behaviour to other reinforcement options.

All tested reinforcements were placed at the top of the specimen only. However, one could expect that if the reinforcement had been placed from both sides of the laminate, even better results could have been achieved. Looking at the results presented in the Figure 3.43, this is indeed the case. The fibre tensile is absent, and the maximum strain in the middle of the specimen stays almost exactly the

same as for the single reinforcement. On the other hand, the leftover damage criteria seem to be even worse than in the case of other tested reinforcements. Fibre kinking, for example, appears directly after the start of the loading conditions. This may be explained by looking at the specimen status for this condition. The damage location is moved more towards the centre of the specimen due to the presence of the reinforcement at the bottom side of the laminate. Similarly, the affected zone by the fibre tensile failure is more at the centre and not as severe as in the case of the single reinforcement. Matrix cracking and fibre splitting also seem to be affected by the placement of the reinforcement on both sides of the laminate. The damage-influenced zone is more extensive, and the damage appears from the area where the reinforcement is placed.

Looking at all the considered reinforcements, it is clear that they are necessary for the permeation and leakage testing. Otherwise, the specimen would experience fibre failure damage near the clamping zone, as seen for all the laminates with the desired strain levels above 0.004 microstrains in the specimen's centre. By implementing a representative curvature of around 3000 [mm], the fibre failure is present in all laminates from the parametric study as the strain at the bottom side of the laminate crosses the value of 0.016 microstrain, which appears to be the material limit. Different reinforcement options can be used to prohibit the damage. A steel ring of around 3 [mm] in thickness or a wide and thick aluminium ring is recommended for the final permeation and leakage testing. Based on the results, they should be sufficient for fibre failure prevention. On the other hand, the double reinforcement seems too invasive, and the loading condition on the bottom side of the laminate could damage the adhesive layer between the ring and the specimen. The molecules of the medium gas would be in direct contact with the adhesive layer. Furthermore, the composite reinforcement also showed good behaviour, but its improvement doesn't justify the additional cost of such an option. Previously proposed options made out of steel or aluminium required much simpler manufacturing processes. The composite ring would require a separate curing cycle and precise tooling to match the existing curvature of the specimen, which could potentially drive the cost too much.

The aspect of the reinforcement that wasn't touched upon during the study is the influence of the additional rings on the measurement area. Extra material present on the surface could obstruct the permeation and leakage pathways. However, when the equal bi-axial zone is considered, the measurement should take place only in the region of interest anyway, which is only limited to the specimen's centre. That's why the outside surface should be sealed off using foil or other methods to minimise the risk of result corruption by external leakages. Finally, another consideration that should be performed is the strength evaluation of the bonding used for the glueing reinforcement onto the specimen. If the bond line fails during testing, the reinforcement will lose its ability to take the laminate's stresses. For that aspect, the cohesive zone modelling should be performed, for example. However, due to the time constraints, this aspect of this research is left as a recommendation for future studies.

## 4.3. Thermal aspect

Even though the specimen was cooled down during the parametric study and the damage analysis to the testing operational temperature of 77 [K], the thermal aspect of the entire setup and the heat transfer to the specimen weren't considered. That thermal analysis was performed on the preliminary testing design, considering different cooling approaches. Firstly, the results of the submersion cooling method are evaluated, and helium heating is touched upon. Then, the other possible cooling options and their influence on the thermal aspect are outlined.

### 4.3.1. Liquid nitrogen submersion method

Two separate analyses were performed to evaluate the thermal aspect of the bulge bi-axial testing rig. One includes the pre-cooling step using cold nitrogen gas, and the second one goes directly to the liquid nitrogen submersion. Looking at the results of the latter one, it is clear that due to the large size of the enclosures, the cooling process takes a long time. Even after the 12500 [sec], the specimen centre didn't reach the desired temperature of the liquid nitrogen. Also, considering the temperature plot from the Figure 3.48a, the specimen stays at room temperature at the beginning of cooling for more than 1000 [sec]. The heat capacity demand of the enclosures and the poor cooling capabilities of the liquid nitrogen causes this. Once the temperature starts going down, the rate is mainly limited by the local heat transfer from the sealing to the specimen and the heat conductivity of the laminate itself, as the rest of the structure is already at the minimum temperature, as seen in the Figure 3.47a.

The situation looks very similar in the case of the method with the pre-cooling step, as the maximum heat flux achieved for the specimen's centre is the same as for the pure submersion method, as seen in the Figure 3.48. However, cooling seems more gradual at the point of exposure to the cold gas as the heat flux reaches only 60% of the value for the pure submersion cooling and doesn't decrease as rapidly, either. But as the system hasn't changed between those two methods, the same limitations still exist, as the temperature of the specimen is limited by the heat transfer and heat conduction of the material system, as the setup temperature at the point of maximum heat flux is almost precisely the same as for the pure submersion method, as seen in the Figure 3.47b. Furthermore, the heat flux present inside the laminate seems to be not affected by the different approaches, as shown in the Figure 3.46. Still, it is different for the enclosures as depicted in the Figure 3.45. Finally, the temperature distribution using a slower method with the pre-cooling step provides a more uniform temperature distribution across the specimen, as seen in the Table 3.9. Considering everything, there seems to be no significant difference between those two approaches. Still, when the amount of liquid nitrogen necessary to cool down the system is considered, as presented in the section 3.3, the method with the pre-cooling step could be more economical. For cold gas cooling, a smaller amount of nitrogen is expected to be used than in the case of rapid submersion. Also, the amount of liquid nitrogen needed to cool down from 177 [K] to 77 [K] would be reduced when looking at the Equation 3.1, as the  $\Delta T$  would be smaller.

Lastly, the testing rig's final thermal aspect is the application of helium at the loading step. At this point, the entire setup should be at the steady state temperature of around 77 [K], but the helium is expected to have a much higher temperature than that. To see the influence of that, the temperature distribution of the specimen after being heated by the helium is presented in the ???. From the graph, it can be noticed that the specimen centre heats up significantly, reaching around  $-110\text{ }^{\circ}\text{C}$ . At the same time, the enclosure heated up by less than 10 degrees. This is mainly caused by the fact that the enclosure is much bigger than the specimen, and the ratio of the affected surface to the volume is much worse for the laminate than for the steel enclosure. This can be only seen in the Figure 3.50, as the specimen seems to be only affected by the warmer helium. Even though the higher temperature of the laminate stays only for 200 [sec], these conditions are unrealistic for the hydrogen tank. That's why it is recommended to pre-cool the helium before applying it to the system, especially as the helium gas has a favourable heat transfer coefficient at higher pressures.

#### 4.3.2. Other cooling methods

Three approaches were tested to see if other cooling methods can improve the setup's thermal performance. Firstly, the influence of the cold gas application was considered. As the heat transfer from the seals limits the cooling rate, the additional cold gas exposure of the entire specimen surface should decrease the laminate temperature faster. Looking at the results presented in the Figure 3.52, this improvement is indeed visible. Due to the higher heat transfer coefficient of the cold gas, the specimen can reach the steady state temperature within 30 [sec], but that temperature is limited by the gas used. If the liquid nitrogen temperature is desirable for the testing, the submersion method should be used, and the time to reach 77 [K] is similar to the one achieved by the method without the gas cooling. Furthermore, the heat flux present in the laminate is different, as seen in the Figure 3.53; the cooling by the cold gas application happens mainly in the trough thickness direction and not in the plane. This might even be beneficial for this type of method as the cooling of the hydrogen tank would also most likely be driven by the through-thickness cooling of the walls. However, such an approach requires a cold gas feed-through system that might be challenging to implement.

Secondly, the cryostat method was tested to see if a completely different cooling approach could deliver better results than the submersion method. From the plots presented in the Figure 3.55, it is clear that the heat flux inside the laminate improved compared to other tested methods by around 67% at the peak point. However, the cooling rate wasn't influenced significantly as the steady state temperature wasn't even reached after 12500 [sec]. Furthermore, it seems that this cooling method only improved the enclosure's cooling, but the decrease in specimen temperature was once again limited to the heat transfer through the sealing and the heat conduction of the composite material. As it can be seen from the Figure 3.56a, the heat flux inside the specimen looks similar to the one presented before for the submersion method.

The final method that was tested mainly was designed to reduce the cooling requirements of the setup on the liquid nitrogen supply by adding cooling fins. Looking at the result presented in the Figure 3.58 and in the Figure 3.57a, it can be noticed that after 12500 [sec], the steady-state temperature

of the specimen was almost reached, similar to the submersion method, and only a fraction of the testing rig was in direct contact with the liquid nitrogen. Furthermore, the temperature of the specimen reached around  $-140$  [ $^{\circ}C$ ], which could be satisfactory, taking into account the economic benefits of using this method. Also, submerging the testing rig even deeper could lower the temperature achievable for the specimen. When heat flux is considered, as seen in the Figure 3.59a, it is visible that the results are significantly different to the ones presented before. This is due mainly to the fact that the cooling in this method happens primarily on one side of the laminate.

All things considered, as the specimen is locked inside the vacuum enclosure, the change in the cooling method mainly affects the metallic enclosure rather than the laminate itself. The cold gas application should be considered to accelerate the cooling process, as then the heat transfer coefficient to the specimen can be significantly improved. From the perspective of the testing cost, adding the cooling fins improves the thermal aspect and the pre-cooling step. Both approaches can significantly lower the value of the required liquid nitrogen to cool down the specimen.

#### 4.4. Research question reflections

As many design decisions about the hydrogen tank are yet to be made, creating a perfectly representative testing rig is challenging. However, this research tried to find guidelines for developing the bulge bi-axial permeation testing rig, making the tank connection to the experiments easier.

Based on the findings that were obtained using the ABAQUS standard FEM analyses and the literature, design options for the setup were narrowed down. Specimen characteristics like thickness, material system, layup, curvature, and diameter, and testing conditions such as temperature, pressure, measurement area and their influence on the testing were discussed. From the literature, it was determined that material systems play a crucial role in the inhibition of crack creation and propagation. That's why toughened epoxy with intermediate modulus fibres like IM7/8552 should be used if the leakage concerns the composite structure. Crack propagation is also heavily affected by the ply sequence of the laminate, where the more orthotropic the layup, the lesser the risk of crack network creation, but at the same time, the greater the risk for delamination caused by the out-of-plane loading. Temperature prohibits permeation in some instances but has minimal influence on the leakage, but material thermal cycling creates cracking. From the analysis, it was also found that the thickness has a significant influence on the reachable strain levels for the specimen in the bulge bi-axial testing rig. Similarly, pressure magnitude was found to be the most straightforward parameter for the stress and strain adjustment during the testing. On the other hand, curvature plays an essential role in the minimisation of the stress concentration due to the clamping, while larger diameters improve the area of measurement and provide a more stable equal-bi-axial zone.

Hence, the bulge bi-axial permeation and leakage testing specimen should have a diameter of around 450 [mm] and a thickness of no more than 5 [mm] to create the membrane conditions. The curvature should be minimised as much as possible to decrease the stress concentrations near the clamping. However, to test larger curvatures, representative of the actual hydrogen tank and at the desirable strains, which were determined to be between 0.004 and 0.005 microstrains, the usage of the reinforcement placed at the top of the laminate is advisable. Pressure should be tuned with the diameter and thickness to achieve the desirable stress state. The boundary conditions of the testing rig should be designed to reduce the specimen's bending after clamping, either by minimising the distance between the bolts and the laminate edge or by using the spacers in the enclosure gap. Another solution could be extending the laminate over the bolt line and bolting the enclosure through the laminate as it was done by the S. Oliver [78]. Furthermore, as the clamping significantly influences the specimen conditions, the permeation and leakage measurement should only be limited to the zone of equal bi-axial strain present in the specimen's centre. The other parts of the laminate should then be sealed to minimise the risk of errors in the measurements. Using such an approach also increases test representativeness as the measurement focuses on the area with the right conditions. Finally, the temperature during the testing conditions should be as low as possible, but in most cases, this depends on practical and economic aspects. Low temperature creates conditions similar to those inside the hydrogen, but using other cooling methods proved to be enough to create damage in the composite laminate. Finally, the cooling of the specimen and its representativeness depend on the operational conditions of the actual tank. It is unclear what the process of hydrogen filling will look like. If the slow process with the pre-cooling step is chosen, then the submersion method should be enough. But if more rapid cooling is

preferred, cold gas or liquid flow through the system should be considered to bring the specimen's temperature down as quickly as possible. Also, pre-conditioning can be used to prepare the specimen for testing, but thermo-mechanical cycles should be used. The laminates without the application of loading or imposed movement constraint are not as susceptible to cracking as otherwise, as shown by the French et al. [35].

Following these findings, it is believed that the right approach for the design of the specimen for the bulge bi-axial permeation and leakage testing has been developed. Furthermore, the way to perform the testing with the right conditions, within the current limitations, has been found to achieve the most representative permeation and leakage testing. That's why the main question of how the element-level testing of CFRP can accurately represent the behaviour of a full-scale hydrogen tank on the topic of permeation and leakage has been answered.

# 5

## Conclusions

This research aimed to find and analyse the most representative approach to perform the bulge bi-axial testing for permeation and leakage. To complete this task, an extensive literature analysis was performed, and multiple FEM simulations were run.

Bulge bi-axial testing was found to depend on the following parameters: specimen thickness, diameter, curvature, layup, material and specific conditions such as pressure loading, temperature or measurement area. From the literature, it was determined that layup plays a role in crack propagation, and large angles between the adjacent plies tend to limit cracking. However, high orthotropy of the laminate causes significant delamination if the out-of-plane loading is considered. Furthermore, the different studies determined that toughened epoxies with intermediate modulus fibre systems are the most promising candidates for the hydrogen tank material. Hence, materials such as IM7/8552 or similar others should be used during testing. In the case of the temperature, the effect is primarily visible in the response of the permeation, but higher  $\Delta T$  is believed to create higher thermal stresses and encourage cracking.

From the performed numerical analyses, it was observed that specimen diameter plays a role in both achievable strain levels and the stable bi-axial zone. Specimens with a greater diameter than 450 [mm], from which only 380 [mm] is under loading conditions, proved to develop a stable equal bi-axial zone, as discussed in subsection 4.1.1. This is the desirable condition for this type of testing, as it simulates the tank states in the end-cap. In the case of the specimen thickness, it was noticed that the thicker laminates are too stiff to reach the desirable strain levels, and the equal bi-axial zone is not as stable as for the thinner laminates. Hence, to keep the stress state of the specimen at a representative condition above 0.004 microstrains, it is advisable to use laminates with 1 or 2 [mm] thickness, as shown in subsection 4.1.3. The other parameter that helped reach the desirable strain levels is pressure. The value of strain at the specimen's centre, reported during the analysis, showed an almost perfect linear relation to the pressure change. Furthermore, values of 15 [bar] and higher proved to be enough to reach tank strain values for the specimen with 450 [mm] diameter and 2 [mm] thickness, as described in subsection 4.1.4. During studies, it was also discovered that specimens experience large stress concentrations near the constraint zone due to the immense force acting on them and stiff clamping. This proved to be a problem, as during the damage analysis, it was found that the laminate couldn't survive the duration of the testing as fibre tensile failure occurred at around 0.016 microstrains, where at the stress concentration point, the strain could reach even 0.040 microstrains for specific specimens. However, it was also noticed that the peak of the stress concentrations depends on the curvature of the specimen. The smaller the curvature, the lower the strain present in that region, as shown in subsection 4.1.2. Furthermore, smaller curvature increased the equal bi-axial zone for the laminate's top and bottom layers. Most of the analyses were performed using cross-ply laminate, but the quasi-isotropic and uni-directional laminate behaviour was also checked. As expected, the uni-directional specimen experienced high stresses at the clamping zone, while the quasi-isotropic specimen performed similarly to the cross-ply, as discussed in subsection 4.1.5.

During damage analysis, it was also determined that to prohibit the specimen from failing, it is recommended to use ring reinforcement at the clamping zone. From the different tested reinforcements, a steel ring with a width of 80 [mm] and a thickness of around 3 [mm] should be enough to reduce the

---

strain below the breaking point of 0.016 microstrains. A broader and thicker aluminium ring should also be enough, as discussed in subsection 4.2.1, but then the measurement area is limited, which is undesirable. It was also shown that the stress state of the laminate in the centre is not hugely affected by the reinforcement, and other damage criteria like matrix cracking or fibre splitting depend mainly on the material system and cooling process.

A set of thermal analyses were also performed to understand the cooling behaviour of the setup better. It was discovered that the heat transfer through the sealing and heat conductivity of the laminate would limit any method that doesn't cool the specimen directly. That's why it is recommended to use a flow-through system with cold gas or cryogenic liquid if a rapid temperature decline of the specimen is desirable. Furthermore, to save liquid nitrogen or other cryogenic liquids, it is advisable to use pre-cooling steps or extend the setup with the cooling fins that can act as a heat sink, as proposed in subsection 4.3.2. Finally, the application of helium into the system after the cooling process is completed can cause a spike in the temperature of the specimen. Hence, it is advisable to pre-cool helium gas before its application.

# 6

## Recommendations

Even though the study's goal was reached during this research, certain things could have been done differently or better to improve the final outcome.

Most importantly, the model that was created for this study should be validated against the real-world example. The experimental data from the physical bulge bi-axial permeation and testing setup should be used to compare the results of the performed simulations. This way, it can be confirmed that the findings of this research are correct, and the model can be used to predict the laminate behaviour at different conditions prior to testing.

It would also be beneficial to create low-cost simulations and run them automatically to obtain a very extensive parametric study and focus only on the areas of interest with the more advanced analysis. This way, the broader range of the possible parameters could be covered, and potentially, other dependencies could be found. Furthermore, if the later study could access the more robust computing unit, all the simulations should be done using a complete enclosure system. As the discussion on boundary conditions shows, it is challenging to simplify the clamping conditions using built-in functions completely. Also, aspects such as slippage are not correctly represented if the influence of other elements is lacking.

In the case of the damage analysis, only damage initiation was looked into. Hence, it is highly recommended to run the simulation using XFEM software and evaluate the damage propagation and the influence of matrix cracking and fibre splitting on specimen durability. Following such an approach, it would be possible to understand better how the damage is created and how it propagates through the structure. Moreover, by extending the damage simulation by the permeability and leakage analysis, the model could predict expected leakage through the given laminate. Also, aspects like void fraction and the effect of moisture should be studied and implemented into the specimen model for a better representation of real-world conditions.

Furthermore, the thermal analysis should also be performed by implementing the CFD simulations. Especially the application of the helium to the system and its interaction with the rest of the setup should be analysed using flow simulations. This way, the exact temperature and the change in the conditions within the testing rig could be created. Also, the liquid nitrogen interaction with the system could be evaluated using this approach. The effect of the evaporation and the mixing of cold gas with warmer air on the setup could be estimated.

Lastly, this research was limited only to the bulge bi-axial testing setup. However, as it was discussed in the chapter 2, other systems, like, for instance, cross-specimen testing, can bring important results for the composite hydrogen tank development. It was indicated that there is still a gap in research in all element-level methods for permeation and leakage testing. Hence, other approaches should also be studied, and the understanding should be built to create the most representative conditions for testing and help the development of hydrogen storage for aviation.

# References

- [1] 2021. URL: <https://www.airbus.com/en/newsroom/news/2021-12-how-to-store-liquid-hydrogen-for-zero-emission-flight>.
- [2] 2022. URL: <https://www.airbus.com/en/innovation/low-carbon-aviation/hydrogen/zeroe>.
- [3] European Commission. (n.d.) *Development of specific aviation cryogenic storage system with a gauging, fuel metering, heat management and monitoring system. Funding amp; tenders*. URL: <https://ec.europa.eu/info/funding-tenders/opportunities/portal/screen/opportunities/topic-details/horizon-jti-cleanh2>. (accessed: 30.06.2023).
- [4] João Alves. “Successful first test for the Ariane 6 vulcain engine”. In: *Links 2960.2015* (2016), p. 660.
- [5] David Anderson, Arthur Edelstein, and Mark Pilgram. *Permeation of Gaseous Hydrogen through Tank Walls at Extremely Low Temperature*. AIAA, 1998.
- [6] International Air Transport Association et al. “Fact Sheet 7: Liquid Hydrogen as A Potential Low-Carbon Fuel for Aviation”. In: *International Air Transport Association: Montreal, QC, Canada* (2019).
- [7] Richard O Ballard. “Next-generation RS-25 engines for the NASA Space Launch System”. In: *European Conference for Aeronautics and Space Sciences (EUCASS 2017)*. M17-6076. 2017.
- [8] Erwin W Baumann et al. “DC-XA structural health-monitoring system”. In: *Smart Structures and Materials 1997: Industrial and Commercial Applications of Smart Structures Technologies*. Vol. 3044. SPIE. 1997, pp. 195–206.
- [9] Vernon Bechel. “Permeability and damage in unloaded cryogenically cycled PMCs”. In: *46th AIAA/ASME/ASCE/AHS/ASC Structures, Structural Dynamics and Materials Conference*. 2005, p. 2156.
- [10] Vernon Bechel, Ran Kim, and Steven Donaldson. “Composites containing barrier layers for reduced permeability at cryogenic temperature”. In: *47th AIAA/ASME/ASCE/AHS/ASC Structures, Structural Dynamics, and Materials Conference 14th AIAA/ASME/AHS Adaptive Structures Conference 7th*. 2006, p. 2092.
- [11] Vernon T Bechel, Mathew Negilski, and Joshua James. “Limiting the permeability of composites for cryogenic applications”. In: *Composites science and Technology* 66.13 (2006), pp. 2284–2295.
- [12] Fabien Benedic, Jean-Philippe Leard, and Christian Lefloch. “Helium high pressure tanks at EADS space transportation new technology with thermoplastic liner”. In: *EADS Report: ADA445482* (2005).
- [13] Jan Christian Both. “Tragfähigkeit von CFK-Metall-Laminaten unter mechanischer und thermischer Belastung”. de. PhD thesis. Technische Universität München, 2014, p. 176.
- [14] Pedro P Camanho et al. “Prediction of in situ strengths and matrix cracking in composites under transverse tension and in-plane shear”. In: *Composites Part A: Applied Science and Manufacturing* 37.2 (2006), pp. 165–176.
- [15] Amelia Ann Case. “Permeability of hybrid composites subjected to extreme thermal cycling and low-velocity impacts”. PhD thesis. Georgia Institute of Technology, 2004.
- [16] R Ortiz Cebolla, B Acosta Iborra, and Frederik Harskamp. “Permeation tests in type-approval regulations for hydrogen fuelled vehicles: Analysis and testing experiences at the JRC–GASTEF facility”. In: *International Journal of Hydrogen Energy* 48.47 (2023), pp. 17923–17939.
- [17] NASA Marshall Spaceflight Center. “The Space Launch Initiative: Technology to Pioneer the Space Frontier”. In: *NASA Fact Sheets* (2003).

- [18] Duo Chen et al. "A review of the polymer for cryogenic application: methods, mechanisms and perspectives". In: *Polymers* 13.3 (2021), p. 320.
- [19] Sukjoo Choi. *Micromechanics, fracture mechanics and gas permeability of composite laminates for cryogenic storage systems*. University of Florida, 2005.
- [20] Barbara Cohen. "Artemis Program Overview". In: *Endurance Science Workshop*. 2023.
- [21] D Coulon. "Vulcain-2 cryogenic engine passes first test with new nozzle extension". In: *ESA Bulletin* 102 (2000), pp. 123–124.
- [22] Howard D Curtis. *Orbital mechanics for engineering students*. Butterworth-Heinemann, 2013.
- [23] S Disdier et al. "Helium permeation in composite materials for cryogenic application". In: *Cryogenics* 38.1 (1998), pp. 135–142.
- [24] Ben B Donahue. "Space Launch System Exploration Upper Stage Development & Missions". In: *2018 AIAA SPACE and Astronautics Forum and Exposition*. 2018, p. 5236.
- [25] K Doyle et al. "Feasibility of carbon fiber/PEEK composites for cryogenic fuel tank applications". In: *12th European Conference on Spacecraft Structures, Materials and Environmental Testing*. Vol. 691. 2012, p. 95.
- [26] D. Dumbacher. "Results of the DC-XA program". In: *Space Programs and Technologies Conference* (1996). DOI: 10.2514/6.1996-4317.
- [27] Dan Dumbacher and Paul Klevatt. "DC-xa - first step top a reusable launch vehicle". In: *Space Programs and Technologies Conference and Exhibit* (1994). DOI: 10.2514/6.1994-4682.
- [28] Dan L Dumbacher and Dennis E Smith. "NASA 2nd generation RLV program introduction, status and future plans". In: *38th Joint Propulsion Conference*. AIAA Paper 2002-4570. 2002.
- [29] LLC. (n.d.) Engineers Edge. *Thermal properties of metals, conductivity, thermal expansion, specific heat*. Engineers Edge - Engineering and Manufacturing Solutions. URL: [https://www.engineersedge.com/properties\\_of\\_metals.htm](https://www.engineersedge.com/properties_of_metals.htm). (accessed: 28.12.2023).
- [30] Hector Estrada and Stanley S Smeltzer III. "Design and Development of a Composite Dome for Experimental Characterization of Material Permeability". In: (1999).
- [31] John Fikes. "nasa composite cryotank technology project game changing program". In: *Defense Manufacturing Conference (DMC) 2015*. M16-4989. 2015.
- [32] John Fikes and John Vickers. "Composite cryotank technologies and demonstration project". In: *JANNAF 6th Liquid Propulsion Subcommittee Meeting*. M11-1318. 2011.
- [33] John C Fikes. *Composite Cryotank Technologies and Demonstration*. Tech. rep. 2014.
- [34] Delma C Freeman Jr, Theodore A Talay, and R Eugene Austin. "Reusable launch vehicle technology program". In: *Acta Astronautica* 41.11 (1997), pp. 777–790.
- [35] Jordan French, Chris Dahlkamp, and Michael Czabaj. "Formation of cryobiasial-induced damage in tape-laminate composites". In: *Composite Structures* 235 (2020), p. 111816.
- [36] Peter Friese. "Experimentelle Untersuchungen zur Permeation kryogenen Heliums und Wasserstoffs durch Kohlenstoffaserverbundwerkstoffe". PhD thesis. DLR Bremen, 2014.
- [37] Thomas Gates, Ray Grenoble, and Karen Whitley. "Permeability and life-time durability of polymer matrix composites for cryogenic fuel tanks". In: *45th AIAA/ASME/ASCE/AHS/ASC structures, structural dynamics & materials conference*. 2004, p. 1859.
- [38] Robert Goetz, RS Ryan, and Ann F Whitaker. "Final report of the X-33 liquid hydrogen tank test investigation team". In: *Marshall Space Flight Center, Huntsville, AL* (2000).
- [39] Arturo Gomez and Howard Smith. "Liquid hydrogen fuel tanks for commercial aviation: Structural sizing and stress analysis". In: *Aerospace Science and Technology* 95 (2019), p. 105438.
- [40] Nathan Gray et al. "Decarbonising ships, planes and trucks: An analysis of suitable low-carbon fuels for the maritime, aviation and haulage sectors". In: *Advances in Applied Energy* 1 (2021), p. 100008.

- [41] Ray Grenoble and Thomas Gates. "Hydrogen gas leak rate testing and post-testing assessment of microcrack damaged composite laminates". In: *47th AIAA/ASME/ASCE/AHS/ASC Structures, Structural Dynamics, and Materials Conference 14th AIAA/ASME/AHS Adaptive Structures Conference 7th*. 2006, p. 2017.
- [42] Ray Grenoble and Thomas Gates. "Hydrogen permeability of polymer matrix composites at cryogenic temperatures". In: *46th AIAA/ASME/ASCE/AHS/ASC structures, structural dynamics and materials conference*. 2005, p. 2086.
- [43] Brian W Grimsley et al. "Hybrid composites for LH2 fuel tank structure". In: (2001).
- [44] David M Grogan. "Damage and permeability in linerless composite cryogenic tanks". PhD thesis. 2015.
- [45] Iwona Grombik et al. "New method of measuring hydrogen concentration in air". In: *Environment Protection Engineering* 32.3 (2006), pp. 75–79.
- [46] Hitoshi Hamori et al. "Gas permeability of CFRP cross-ply laminates with thin-ply barrier layers under cryogenic and biaxial loading conditions". In: *Composite Structures* 245 (2020), p. 112326.
- [47] Hitoshi Hamori et al. "Numerical and experimental evaluation of the formation of leakage paths through CFRP cross-ply laminates with leak barrier layers". In: *Composite Structures* 230 (2019), p. 111530.
- [48] Ken Higuchi et al. "Development and flight test of metal-lined CFRP cryogenic tank for reusable rocket". In: *Acta Astronautica* 57.2-8 (2005), pp. 432–437.
- [49] Jörg Hohe et al. "Performance of fiber reinforced materials under cryogenic conditions—A review". In: *Composites Part A: Applied Science and Manufacturing* 141 (2021), p. 106226.
- [50] Jon Huete and Pericles Pilidis. "Parametric study on tank integration for hydrogen civil aviation propulsion". In: *International Journal of Hydrogen Energy* 46.74 (2021), pp. 37049–37062.
- [51] Jens Humpenöder. *Gaspermeation von Faserverbunden mit Polymermatrices*. Forschungszentrum Karlsruhe, 1997.
- [52] Ahmed Ibrahim, Yeong Ryu, and Mir Saidpour. "Stress analysis of thin-walled pressure vessels". In: *Modern Mechanical Engineering* 5.01 (2015), pp. 1–9.
- [53] Yoshifumi Inatani, Yoshihiro Naruo, and Koich Yonemoto. "Concept and preliminary flight testing of a fully reusable rocket vehicle". In: *Journal of Spacecraft and Rockets* 38.1 (2001), pp. 36–42.
- [54] Justin Jackson. "CCTD Testing Overview". In: *Composites Materials and Manufacturing Technologies for Space Applications Technical Interchange Meeting*. M15-4547. 2015.
- [55] Justin R Jackson, John Vickers, and John Fikes. *Composite cryotank technologies and development 2.4 and 5.5 m out of autoclave tank test results*. Tech. rep. 2015.
- [56] Yves Jannot and Didier Lasseux. "A new quasi-steady method to measure gas permeability of weakly permeable porous media". In: *Review of Scientific Instruments* 83.1 (2012), p. 015113.
- [57] Theodore F Johnson, David W Sleight, and Robert A Martin. "Structures and design phase I summary for the NASA composite cryotank technology demonstration project". In: *54th AIAA/ASME/ASCE/AHS/ASC Structures, Structural Dynamics, and Materials Conference*. 2013, p. 1825.
- [58] Zhu Kang et al. "Experimental study on cool down characteristics and thermal stress of cryogenic tank during LN2 filling process". In: *Applied Thermal Engineering* 130 (2018), pp. 951–961.
- [59] Seth Stovack Kessler. "Cryocycling and Mechanical Testing of CFRP for X-33 Liquid H2 Fuel Tank Structure". PhD thesis. Technology Laboratory for Advanced Composites, Department of Aeronautics and ..., 1998.
- [60] Jung-Myung Kim et al. "Evaluation of Permeability Performance by Cryogenic Thermal Shock in Composite Propellant Tank for Space Launch Vehicles". In: *Composites Research* 33.5 (2020), pp. 309–314.
- [61] Hisashi Kumazawa, Takahira Aoki, and Ippei Susuki. "Analysis and experiment of gas leakage through composite laminates for propellant tanks". In: *AIAA journal* 41.10 (2003), pp. 2037–2044.

- [62] Hisashi Kumazawa, Ippei Susuki, and Takahira Aoki. "Gas leakage evaluation of CFRP cross-ply laminates under biaxial loadings". In: *Journal of composite materials* 40.10 (2006), pp. 853–871.
- [63] Hortense Laeuffer et al. "A new device to measure permeability evolution under pressure loading: Application to CFRP pipes". In: *Measurement* 98 (2017), pp. 68–76.
- [64] Gary Letchworth. "X-33 reusable launch vehicle demonstrator, spaceport and range". In: *AIAA Space 2011 Conference & Exposition*. 2011, p. 7314.
- [65] Ni Liu et al. "Progress in research on composite cryogenic propellant tank for large aerospace vehicles". In: *Composites Part A: Applied Science and Manufacturing* 143 (2021), p. 106297. ISSN: 1359-835X. DOI: <https://doi.org/10.1016/j.compositesa.2021.106297>. URL: <https://www.sciencedirect.com/science/article/pii/S1359835X21000270>.
- [66] JC Malenfant et al. "Thermo mechanical damage influence on the composite material permeability: Application to the design of a linerless cryogenic tank. Theme: Composite Structure". In: (2009).
- [67] Douglas A McCarville et al. "Design, manufacture and test of cryotank components". In: *Comprehensive Composite Materials II* 3.M17-6280 (2017).
- [68] Jinxin Meng et al. "Leakage performance of CFRP laminate under cryogenic temperature: Experimental and simulation study". In: *Composites Science and Technology* 226 (2022), p. 109550.
- [69] Subodh K Mital et al. "Review of current state of the art and key design issues with potential solutions for liquid hydrogen cryogenic storage tank structures for aircraft applications". In: (2006).
- [70] Shraeya Mithal and Dan Rutherford. "ICAO's 2050 net-zero CO". In: *POLICY* (2023).
- [71] Grace Nehls. *Boeing all-composite cryogenic fuel tank proves technology readiness*. Feb. 2022. URL: <https://www.compositesworld.com/news/boeing-all-composite-cryogenic-fuel-tank-proves-technology-readiness>.
- [72] Hoi Dick Ng and John HS Lee. "Comments on explosion problems for hydrogen safety". In: *Journal of Loss Prevention in the Process Industries* 21.2 (2008), pp. 136–146.
- [73] Mindy Niedermeyer and RG Clinton Jr. "X-33 LH2 tank failure investigation findings". In: *Aerospace Materials, Processes and Environmental Technology*. 2000.
- [74] Jae Noh et al. "Numerical modeling, thermomechanical testing, and NDE procedures for prediction of microcracking induced permeability of cryogenic composites". In: *5th Conference on Aerospace Materials, Processes, and Environmental Technology*. 2003.
- [75] E OCONNOR. "Saturn V launch vehicle report". In: *3rd Annual Meeting*. 1966, p. 840.
- [76] Tomoya OHE et al. "Development of Large Liquid Hydrogen Tank". In: *Journal of High Pressure Institute of Japan* 58.3 (2020), pp. 138–151. DOI: 10.11181/hpi.58.138.
- [77] BM Oliver, James G Bradley, and Harry Farrar IV. "Helium concentration in the Earth's lower atmosphere". In: *Geochimica et Cosmochimica Acta* 48.9 (1984), pp. 1759–1767.
- [78] Stanley T Oliver. *Analysis of a circular composite disk subjected to edge rotations and hydrostatic pressure*. The University of Alabama in Huntsville, 2004.
- [79] ST Pinho et al. "Material and structural response of polymer-matrix fibre-reinforced composites". In: *Journal of Composite Materials* 46.19-20 (2012), pp. 2313–2341.
- [80] Richard W Powell, Stephen A Cook, and Mary Kae Lockwood. "The road from the NASA access to space study to a reusable launch vehicle". In: *International Astronautical Congress*. 1998.
- [81] Leonardo Raffaelli. "Thermomechanics of Fibre Reinforced Epoxies for Cryogenic Pressurized Containment". PhD thesis. Technische Universität München, 2006.
- [82] Jonathan Ransom et al. "Lessons learned from recent failure and incident investigations of composite structures". In: *49th AIAA/ASME/ASCE/AHS/ASC Structures, Structural Dynamics, and Materials Conference, 16th AIAA/ASME/AHS Adaptive Structures Conference, 10th AIAA Non-Deterministic Approaches Conference, 9th AIAA Gossamer Spacecraft Forum, 4th AIAA Multidisciplinary Design Optimization Specialists Conference*. 2009, p. 2317.

- [83] Carolin Rauh, Thomas Reimer, and Jascha Wilken. "Leakage Investigation of Epoxy-Based Composite Laminates for Reusable Cryogenic Propellant Tanks". In: (2022).
- [84] H Kevin Rivers, Joseph G Sikora, and Sankara N Sankaran. "Detection of hydrogen leakage in a composite sandwich structure at cryogenic temperature". In: *Journal of spacecraft and rockets* 39.3 (2002), pp. 452–459.
- [85] M Robinson. "Composite cryogenic propellant tank development". In: *35th Structures, Structural Dynamics, and Materials Conference*. 1994, p. 1375.
- [86] Michael Robinson, Jeffrey Eichinger, and Scott Johnson. "Hydrogen permeability requirements and testing for reusable launch vehicle tanks". In: *43rd AIAA/ASME/ASCE/AHS/ASC Structures, Structural Dynamics, and Materials Conference*. 2002, p. 1418.
- [87] Michael Robinson et al. "Trade study results for a second-generation reusable launch vehicle composite hydrogen tank". In: *45th AIAA/ASME/ASCE/AHS/ASC structures, structural dynamics & materials conference*. 2004, p. 1932.
- [88] Michael J Robinson. "Determination of allowable hydrogen permeation rates for launch vehicle propellant tanks". In: *Journal of Spacecraft and Rockets* 45.1 (2008), pp. 82–89.
- [89] Hans Rottländer, Walter Umrath, and Gerhard Voss. "Fundamentals of leak detection". In: *Leybold GMBH (ed) Cat 199* (2016), p. 37.
- [90] Samit Roy and Michael Benjamin. "Modeling of permeation and damage in graphite/epoxy laminates for cryogenic fuel storage". In: *Composites Science and Technology* 64.13-14 (2004), pp. 2051–2065.
- [91] Michael Scheerer et al. "Analyses and Testing of the Thermo-Mechanical Behaviour of Cryogenic Composite Propellant Feed Lines". In: *13th European Conference on Spacecraft Structures, Materials & Environmental Testing*. Vol. 727. 2014, p. 124.
- [92] Daniel Schultheiß. "Permeation barrier for lightweight liquid hydrogen tanks". In: (2007).
- [93] Martin Sippel et al. "Final Results of Advanced Cryo-Tanks Research Project CHATT". In: *6TH EUROPEAN CONFERENCE FOR AERONAUTICS AND SPACE SCIENCES (EUCASS) 2015*. The project CHATT is part of the European Commission's Seventh Framework Programme (FP7) and run on behalf of the Commission by DLR-SART in a multinational collaboration. One of the core objectives is to investigate Carbon Fiber Reinforced Plastic (CFRP) cryogenic pressure tanks. Four different subscale CFRP-tanks are designed, manufactured, and tested. The total budget is exceeding 4.2 M€ with an EU contribution of almost 3.3 M€ [1]. The project started in January 2012, run for 42 months and now ends on 30th June 2015 as planned. EUCASS, June 2015. URL: <https://elib.dlr.de/101483/>.
- [94] Ingo Staack, Alejandro Sobron, and Petter Krus. "The potential of full-electric aircraft for civil transportation: from the Breguet range equation to operational aspects". In: *CEAS Aeronautical Journal* 12.4 (2021), pp. 803–819.
- [95] National Institute of standards and technology. *Index of Material Properties*. URL: <https://trc.nist.gov/cryogenics/materials/materialproperties.htm>. (accessed: 28.12.2023).
- [96] Stephen Timoshenko, Sergius Woinowsky-Krieger, et al. *Theory of plates and shells*. Vol. 2. McGraw-hill New York, 1959.
- [97] Furkan Ismail Ulu. "Measurement of multidirectional thermal conductivity of IM7-G/8552 unidirectional composite laminate". PhD thesis. North Carolina Agricultural and Technical State University, 2015.
- [98] Kate Underhill, Andreas Flock, and ESA Space Transportation. "Focus on Low-Cost Light-Weight Upper Stage within ESA's Future Launchers Preparatory Programme (FLPP)". In: (2022).
- [99] Pfeiffer Vacuum. *Vacuum technology know how*. 2009.
- [100] John H Vickers. "Composite australia conference composite cryotank project structures for launch vehicles". In: *Composites Australia Conference and Trade Show*. M13-2455. 2013.
- [101] Marina Wolff and Markus Quadt. "Maturation of selected and promising CFRP-technologies for bare tanks and structures of a representative future launcher upper stage demonstrator". In: *European Conference on Spacecraft Structures Materials and Environmental Testing*. 103. 2023.

- [102] Inc. Wolfram Research. *Technical data for the element Indium in the Periodic Table*. (n.d.). URL: <https://periodictable.com/Elements/049/data.html>. (accessed: 28.12.2023).
- [103] Xue Feng Yao et al. "Experimental study of helium leakage parameters in flexible composite". In: *Journal of applied polymer science* 116.6 (2010), pp. 3562–3568.
- [104] T Yokozeki et al. "Experimental evaluation of gas permeability through damaged composite laminates for cryogenic tank". In: *Composites science and technology* 69.9 (2009), pp. 1334–1340.
- [105] Tomohiro Yokozeki, Takahira Aoki, and Takashi Ishikawa. "Experimental cryogenic gas leakage through damaged composite laminates for propellant tank application". In: *Journal of Spacecraft and rockets* 42.2 (2005), pp. 363–366.
- [106] Tomohiro Yokozeki, Takahira Aoki, and Takashi Ishikawa. "Gas permeability of microcracked laminates under cryogenic conditions". In: *44th AIAA/ASME/ASCE/AHS/ASC Structures, Structural Dynamics, and Materials Conference*. 2003, p. 1604.
- [107] Tomohiro Yokozeki et al. "Evaluation of gas permeability of cfrp laminates under cyclic loadings". In: *TRANSACTIONS OF THE JAPAN SOCIETY FOR AERONAUTICAL AND SPACE SCIENCES, AEROSPACE TECHNOLOGY JAPAN* 8.ists27 (2010), Pc\_5–Pc\_9.
- [108] Koichi Yonemoto et al. "Application of CFRP with high hydrogen gas barrier characteristics to fuel tanks of space transportation system". In: *TRANSACTIONS OF THE JAPAN SOCIETY FOR AERONAUTICAL AND SPACE SCIENCES, SPACE TECHNOLOGY JAPAN* 7.ists26 (2009), Pc\_13–Pc\_18.
- [109] Hongfei Zheng et al. "The application of carbon fiber composites in cryotank". In: *Solidification*. IntechOpen, 2018.

# 7

## Model verification

In this chapter, the results of the model verification are provided. Firstly, the mesh convergence study is outlined with the strain and stress results in graphs corresponding to different paths across the specimen. Then, the meshing strategy outcome is presented, where different choices of specimen meshing are compared. Finally, the results of the verification are provided.

### 7.1. Mesh convergence

To present the results of the mesh convergence, the values of stress and strain in both in-plane directions are provided along the different paths across the specimen. The chosen paths are presented in the Table 7.1. The paths along the X and Z- coordinate systems are provided to see the dependence of the directions. The large and small circles are also used for the view around the specimen. This way, the convergence can be compared across the entire specimen rather than a single point.

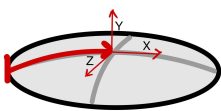
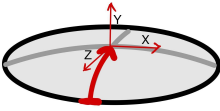
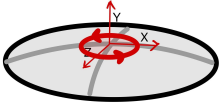
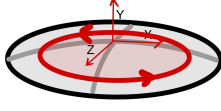
X-path	Z-path	Small circle	Large circle
			

Table 7.1: Chosen paths across the specimen for the results presentation

#### 7.1.1. Results for the X-path

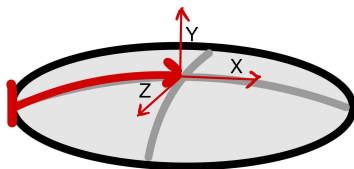
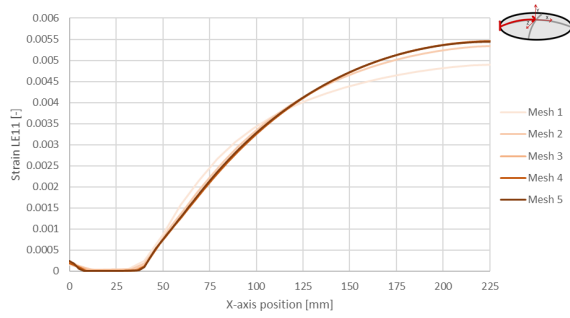
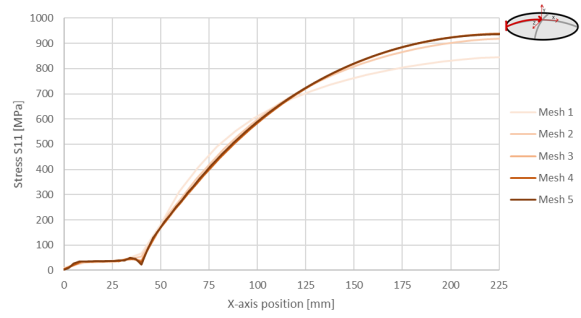


Figure 7.1: X-path used for the results presentation.

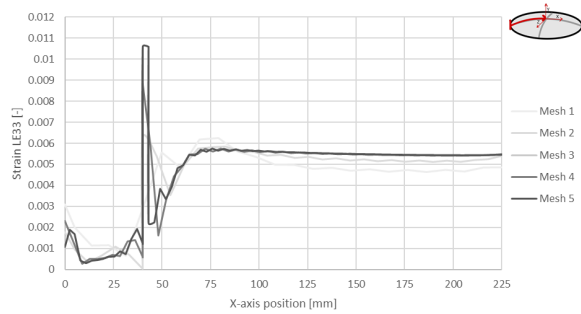
Firstly, the results of the different mesh element sizes are provided along the X-path, starting from the edge and continuing until the specimen's middle. For the results, the values of stress  $S_{11}$ ,  $S_{33}$  and strain  $LE_{11}$ ,  $LE_{33}$  are shown. In the Figure 7.2a, the results of Strain ( $LE_{11}$ ), in the Figure 7.2c, the results of Strain ( $LE_{33}$ ), in the Figure 7.2b, the results of the stress ( $S_{11}$ ), in the Figure 7.2d, the results of the stress ( $S_{33}$ ) are provided.



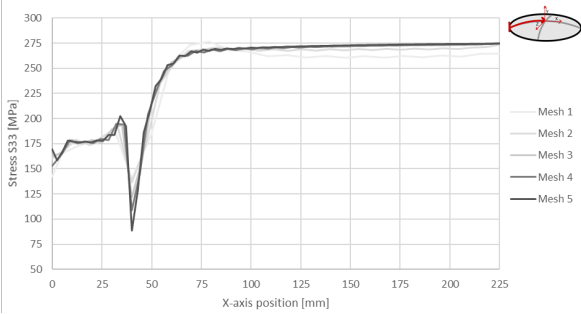
(a) Mesh convergence study results for the strain LE11 along the x-path



(b) Mesh convergence study results for the stress S11 along the x-path



(c) Mesh convergence study results for the strain LE33 along the x-path



(d) Mesh convergence study results for the stress S33 along the x-path

Figure 7.2: The results of the mesh convergence study along the x-path

## 7.1.2. Results for the Z-path

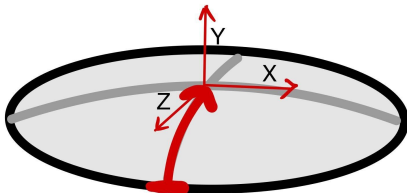
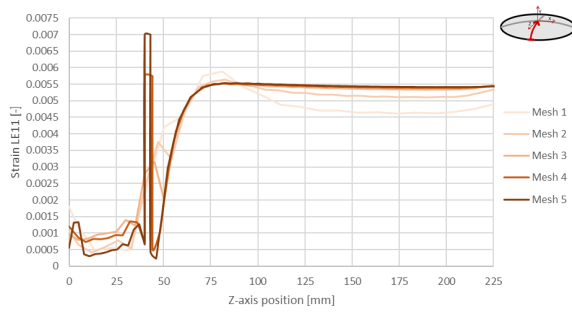
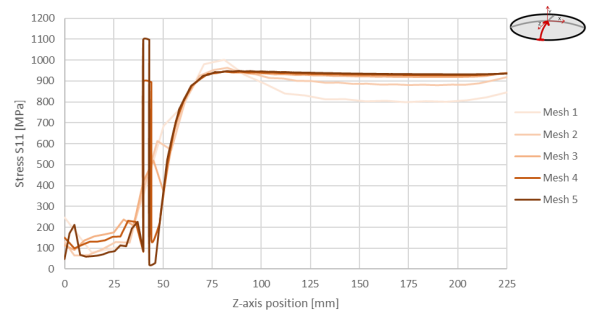


Figure 7.3: Z-path used for the results presentation

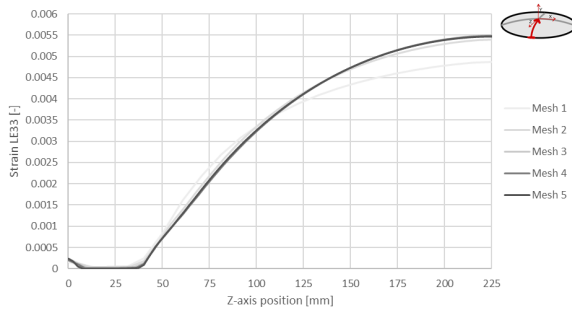
Then, the results of the different mesh element sizes are provided along the Z-path, as shown in the Figure 7.3, starting from the edge and continuing until the specimen's middle. For the results, the values of stress S11, S33 and strain LE11, LE33 are shown. In the Figure 7.4a, the results of Strain (LE11), in the Figure 7.4c, the results of Strain (LE33), in the Figure 7.4b, the results of the stress (S11), in the Figure 7.4d, the results of the stress (S33) are provided.



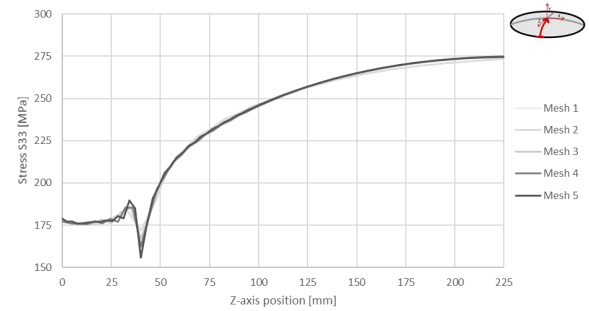
(a) Mesh convergence study results for the strain LE11 along the z-path



(b) Mesh convergence study results for the stress S11 along the z-path



(c) Mesh convergence study results for the strain LE33 along the z-path



(d) Mesh convergence study results for the stress S33 along the z-path

Figure 7.4: The results of the mesh convergence study along the Z-path

### 7.1.3. Results for the Small circular path

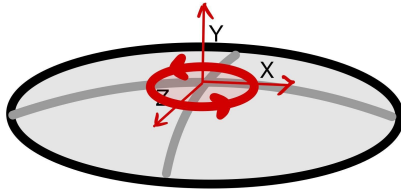
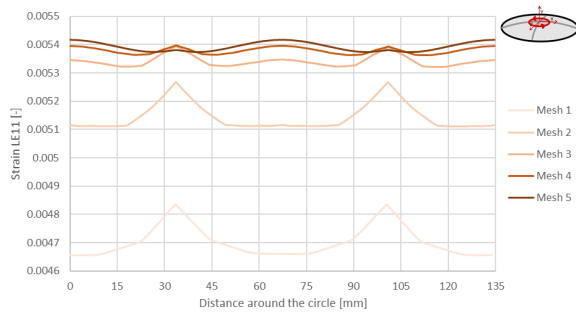
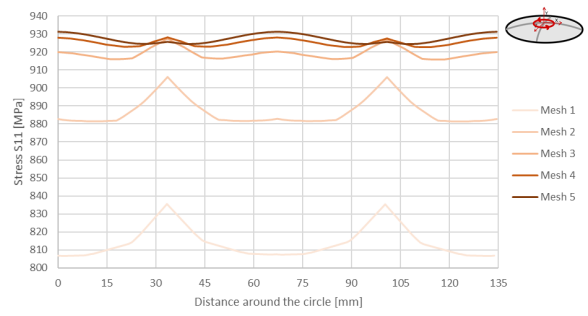


Figure 7.5: Small circle path used for the results presentation

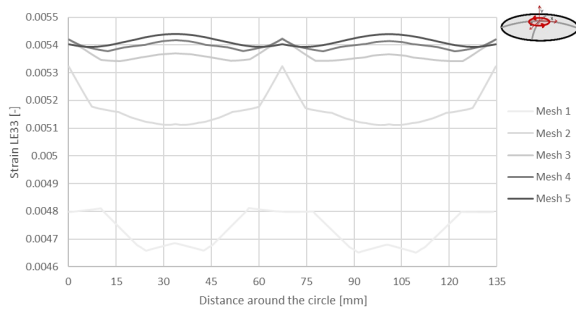
After that, the results of the different mesh element sizes are provided along the small circle path, as shown in the Figure 7.5, going around the small circumference around 50 elements long in radius. For the results, the values of stress S11, S33 and strain LE11, LE33 are shown. In the Figure 7.6a, the results of Strain (LE11), in the Figure 7.6c, the results of Strain (LE33), in the Figure 7.6b, the results of the stress (S11), in the Figure 7.6d, the results of the stress (S33) are provided.



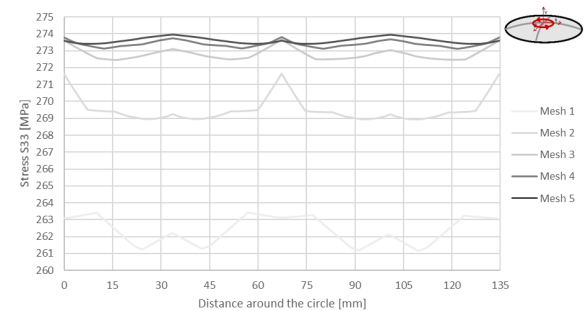
(a) Mesh convergence study results for the strain LE11 along the small circle path



(b) Mesh convergence study results for the stress S11 along the small circle path



(c) Mesh convergence study results for the strain LE33 along the small circle path



(d) Mesh convergence study results for the stress S33 along the small circle path

Figure 7.6: The results of the mesh convergence study along the small circle path

### 7.1.4. Results for the Large circular path

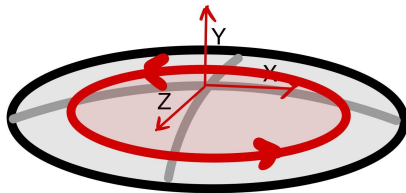
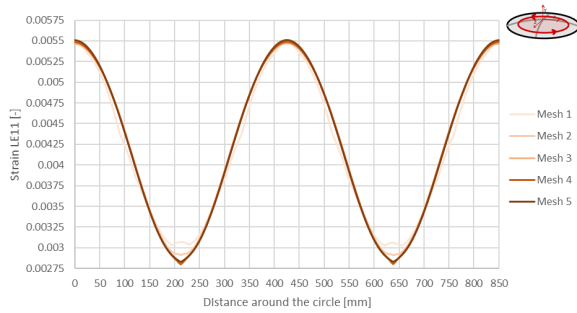
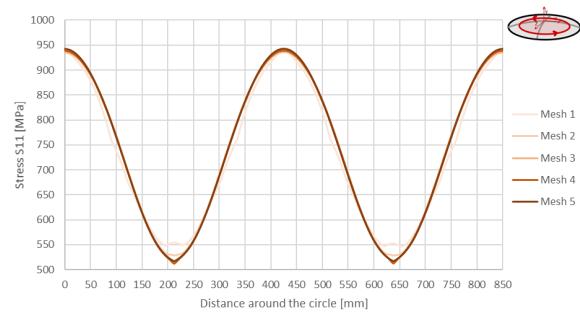


Figure 7.7: Large circle path used for the results presentation

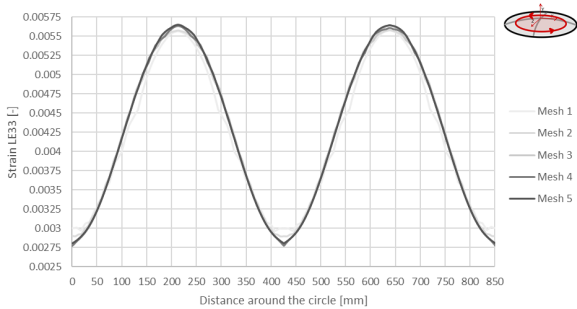
Lastly, the results of the different mesh element sizes are provided along the large circle path, as shown in the Figure 7.7, going around the large circumference around 150 elements long in radius. For the results, the values of stress S11, S33 and strain LE11, LE33 are shown. In the Figure 7.8a, the results of Strain (LE11), in the Figure 7.8b, the results of Strain (LE33), in the Figure 7.8c, the results of the stress (S11), in the Figure 7.8d, the results of the stress (S33) are provided.



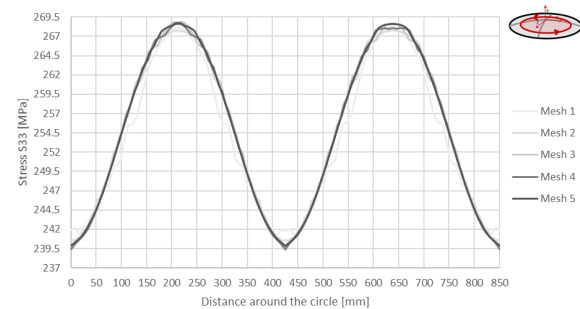
(a) Mesh convergence study results for the strain LE11 along the large circle path



(b) Mesh convergence study results for the stress S11 along the large circle path



(c) Mesh convergence study results for the strain LE33 along the large circle path



(d) Mesh convergence study results for the stress S33 along the large circle path

Figure 7.8: The results of the mesh convergence study along the large circle path

### 7.1.5. Meshing strategy

The results of the meshing strategy are provided below. Firstly, the total CPU time of the analysis for each of the models is shown in the Table 7.2. Then, the stress and strain results are presented for both paths along the x-coordinate and z-coordinate.

Mesh Strategy	Element number	Total CPU time [s]
SQS	355616	63164
STS	371040	102980
TET-BIG	351072	27742
TET-SMALL	363248	79265

Table 7.2: Computing time of each meshing methods.

#### Results for the X-path

For the results of the meshing strategy along the x-path, the values of stress S11, S33 and strain LE11, LE33 are shown. In the Figure 7.10a, the results of Strain (LE11), in the Figure 7.10c, the results of Strain (LE33), in the Figure 7.10b, the results of the stress (S11), in the Figure 7.10d, the results of the stress (S33) are provided. Firstly, however, the vertical displacement for different meshing strategies is shown in the Figure 7.9

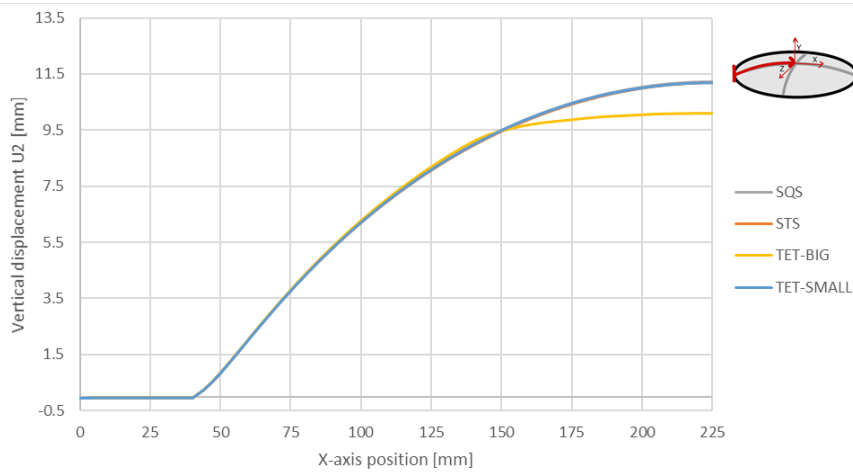
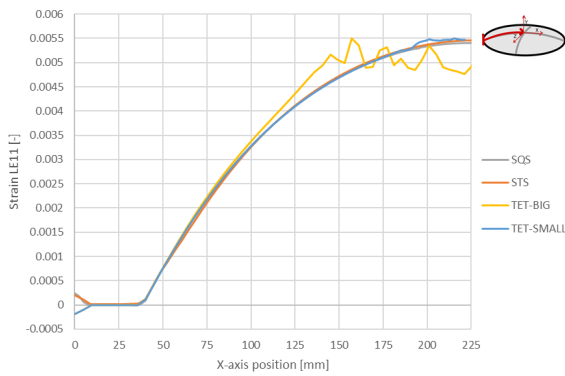
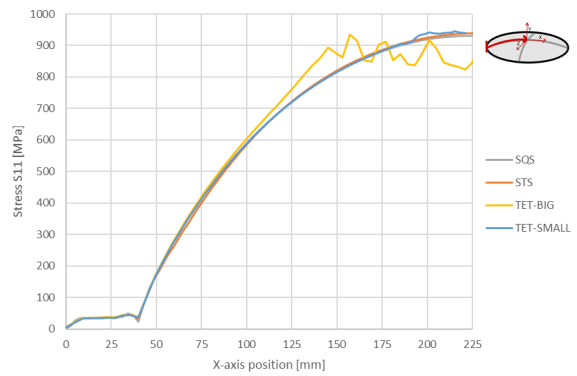


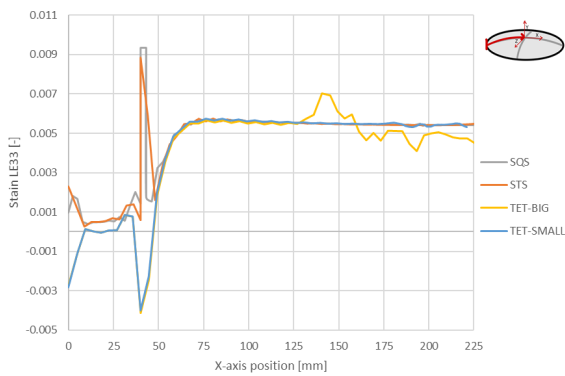
Figure 7.9: Vertical displacement along the x-path for different mesh strategies



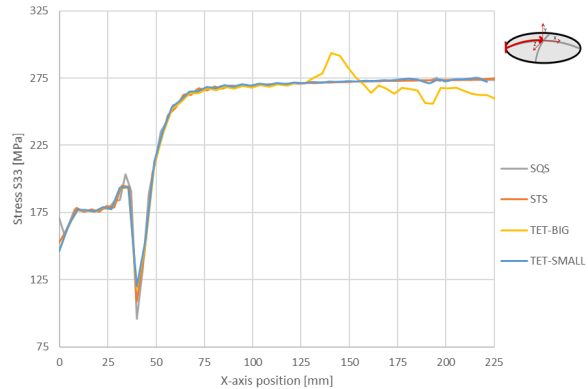
(a) Meshing strategy study results for the strain LE11 along the x-path



(b) Meshing strategy study results for the stress S11 along the x-path



(c) Meshing strategy study results for the strain LE33 along the x-path

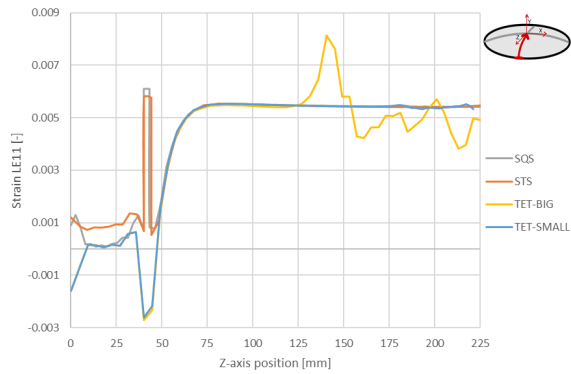


(d) Meshing strategy study results for the stress S33 along the x-path

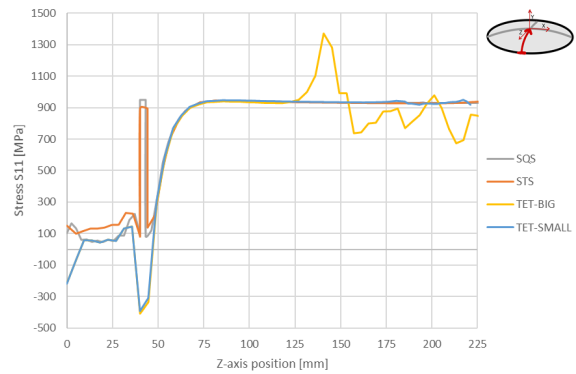
Figure 7.10: The results of the meshing strategy study along the x-path

### Results for the Z-path

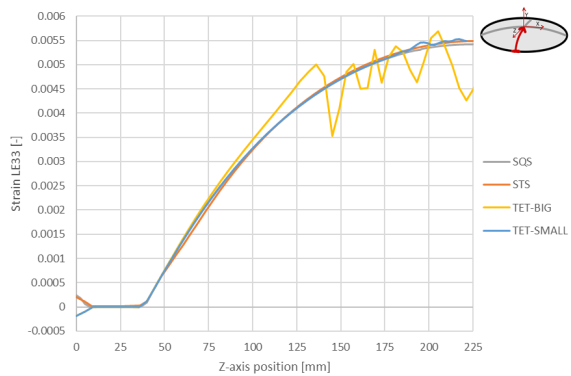
Then, the results of the meshing strategy along the z-path are provided. The values of stress S11, S33 and strain LE11, LE33 are shown. In the Figure 7.11a, the results of Strain (LE11), in the Figure 7.11c, the results of Strain (LE33), in the Figure 7.11b, the results of the stress (S11), in the Figure 7.11d, the results of the stress (S33) are provided.



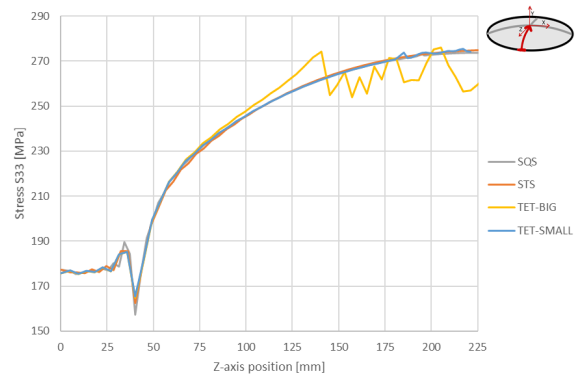
(a) Meshing strategy study results for the strain LE11 along the z-path



(b) Meshing strategy study results for the stress S11 along the z-path



(c) Meshing strategy study results for the strain LE33 along the z-path



(d) Meshing strategy study results for the stress S33 along the z-path

Figure 7.11: The results of the meshing strategy study along the z-path

### Conclusions of the initial Meshing strategy

The results clearly show that the SQS and STS meshing strategies provide the most accurate results. They don't show any instabilities behaviour, especially near the centre of the specimen, in comparison to the other method, as it can be seen in the Figure 7.10a for instance. Looking also at the computing times presented in the Table 7.2, the SQS seems like the most reliable choice for future studies. However, square partitioning can cause dependency on the results, especially close to the partitioning lines. To see if this dependency is significant and can bring issues at a later point, additional considerations have to be performed. They should evaluate the result at the partitioning line near the square part.

### Additional Considerations

To provide the results of the analysis regarding the dependency of the square partitioning line. The stress and strain graphs are provided along the circular path that crosses the square in the middle of the SQS mesh. In the Figure 7.12a, the strain (LE11), in the Figure 7.12b, the stress (S11), in the Figure 7.12c, the strain (LE33) and in the Figure 7.12d, the stress (S33).

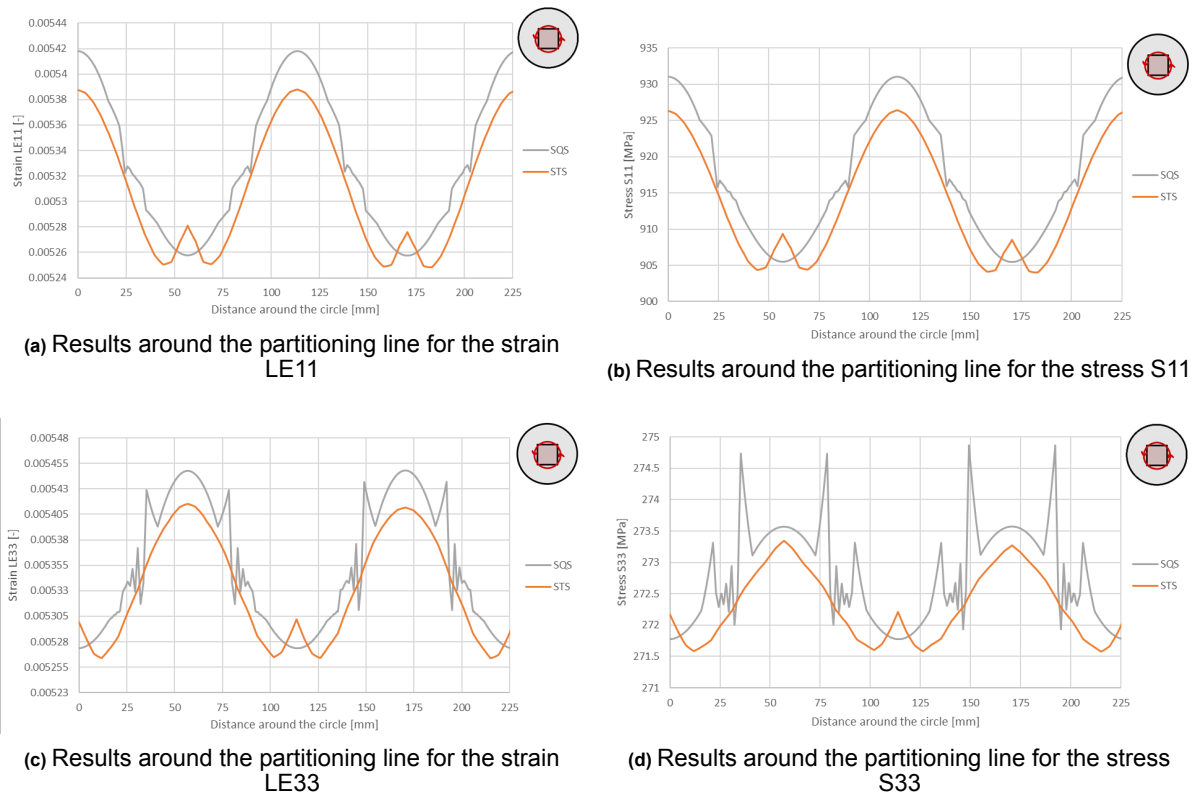


**Figure 7.12:** The outcome of the additional study for the determination of the dependency of the square partitioning line.

To see the difference between the two meshing strategies, the values at the peaks that correspond to the crossing point of the x and z-coordinate are provided below in the Table 7.3.

	S11 [MPa]	S33 [MPa]	LE11 [-]	LE33 [-]
<b>SQS</b>	931.0904	274.7386	0.005418	0.005429
<b>STS</b>	926.4529	272.4575	0.005388	0.005356
<b>Relative error at the peaks [%]</b>	0.5	0.84	0.56	1.36

**Table 7.3:** Specific values of the stress and strain, from the results regarding the determination of the dependency of the square partitioning line

### Final outcome of the Meshing strategy study

Based on the values provided in the Table 7.3, it is visible that the relative error for most of the values is below 1%, apart from the results for the strain LE33. However, even though the error is present for the SQS mesh, considering the performance gain from the Table 7.2, the mesh with square partitioning in the middle of the specimen will be used in the later studies. Such a mesh minimises the element distortion that translates to the 50% decrease in the computation time. The reduction of results quality by around 1% is justified in this case, as the study aims to gain an understanding rather than provide the most accurate results possible.

### 7.1.6. Verification

The results of the analytical equation and the FEM analysis, performed for the verification purposes for the aluminium simply supported disk are provided in the Table 7.4.

	w for the q=10 [bar]	w for the q=20 [bar]
<b>FEM [mm]</b>	17.1412	21.7211
<b>Analytical [mm]</b>	17.5310	22.0877
<b>Relative error [%]</b>	2.22	1.66

**Table 7.4:** Results of the performed verification

From the performed verification, the FEM model is in the range of 2% from the analytical method used. The analytical model is an approximate model. Hence, the presented results are deemed to be close enough. Also, with the higher pressures, the values are getting closer to each other, which indicates that at the relevant strains, the model should be even more accurate.